AD NUMBER

AD913688

LIMITATION CHANGES

TO:

Approved for public release; distribution is unlimited.

FROM:

Distribution authorized to U.S. Gov't. agencies only; Test and Evaluation; 21 JUN 1973. Other requests shall be referred to Air Force Avionics Laboratory, Attn: RSO-4, Wright-Patterson AFB, OH 45433.

AUTHORITY

AFAL ltr, 19 Mar 1976

AFAL-TR-73-188

ELECTRO-OPTICAL AEROSPACE SURVEILLANCE STUDIES

L. R. Baker
R. H. Cromwell
J. D. Gaskill

September 1973

Prepared for the
Air Force Avionics Laboratory
Air Force Systems Command
Wright-Patterson Air Force Base, Ohio

Optical Sciences Center
University of Arizona
Tucson, Arizona 85721

DISCLAIMER NOTICE

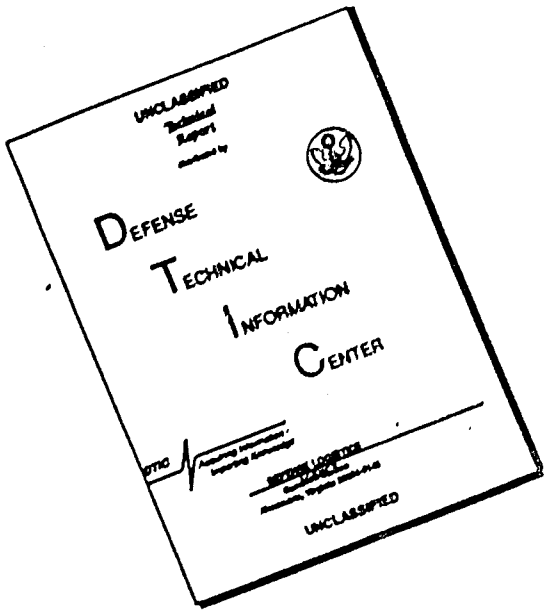

THIS DOCUMENT IS BEST QUALITY AVAILABLE. THE COPY FURNISHED TO DTIC CONTAINED A SIGNIFICANT NUMBER OF PAGES WHICH DO NOT REPRODUCE LEGIBLY.

NOTICE

When Government drawings, specifications, or other data are used for any purpose other than in connection with a definitely related Government procurement operation, the United States Government thereby incurs no responsibility nor any obligation whatsoever; and the fact that the government may have formulated. furnished, or in any way supplied the said drawings, specifications, or other data is not to be regarded by implication or otherwise as in any manner licensing the holder or any other person or corporation, or conveying any rights or permission to manufacture, use, or sell any patented invention that may in any way be related thereto.

Copies of this report should not be returned unless return is required by security considerations, contractual obligations, or notice on a specific document.

AFAL-TR-73-188

ELECTRO-OPTICAL AEROSPACE SURVEILLANCE STUDIES

L. R. Baker
R. H. Cromwell
J. D. Gaskill

September 1973

Prepared for the
Air Force Avionics Laboratory
Air Force Systems Command
Wright-Patterson Air Force Base, Ohio

Optical Sciences Center
University of Arizona
Tucson, Arizona 85721

FOREWORD

This final technical report on Electro-Optical Aerospace Surveillance Studies covers the period from December 1969 through December 1972. The work was accomplished under Contract F33615-70-C-1203 and performed by the Optical Sciences Center of The University of Arizona at Tuscon. The contractors principal investigator was Dr. J. D. Gaskill. The Air Force Project Officer was Mr. Luther H. Meuser of the Surveillance Branch, Air Force Avionics Laboratory, Air Force Project, Task and Work Unit Identification is 7660 03 03. The Program Element is 62204F.

This report has been reviewed and is approved for publication.

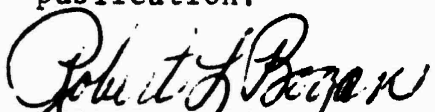

ROBERT L. BOGAN, MAJ, USAF
Acting Chief, Surveillance Branch
Reconnaissance and Surveillance Division

ABSTRACT

The purpose of this contract was to study methods for improving images of space objects obtained with earth-based telescopes. The results of the four contractual tasks are presented. With regard to Task I, recommendations are given for the best intensifier/SIT combinations and relay optics for the Cloudcroft satellite imaging program. As discussed in the section on Task II, it has been concluded that the wavefront-determination-correction method of image restoration is probably not feasible if only linear, postdetection inverse-filtering techniques are used. A discussion of the telescope calibration instrumentation is also included. With regard to Task III, information is listed that allows the optimum film/*f*-number combination to be determined for use with the *f*/3 focal reducer. The design and operation of the *f*/3 focal reducer are discussed in the section on Task IV.

CONTENTS

LIST OF ILLUSTRATIONS

INTRODUCTION

The objective of aerospace surveillance is the close and continuing observation of objects in a designated aerospace volume above the surface of the earth to accrue information for intelligence and early warning applications supporting both military defensive and offensive actions. The Air Force Avionics Laboratory is engaged in an extensive exploratory development program aimed at this general goal and has established an observatory at Cloudcroft, New Mexico, for accomplishing experimental field work under this program in the optical portion of the electromagnetic spectrum.

The specific problem is to improve optical and electro-optical techniques in order to optimize the capability of observing, identifying, and measuring space objects at distances up to 1000 miles and to develop techniques for reducing the degrading effects of the earth's atmosphere when making such observations.

The main purpose of the work reported herein was to investigate optical imaging and electro-optical sensing of observable phenomena and characteristics of space objects, and to identify experimental work needed to extend current capabilities and to exploit advanced technological possibilities beyond the present exploratory program. A further objective was to perform selected experiments at the AFAL Electro-Optical Experimental Station, Cloudcroft, New Mexico. This included formulation of the basic experimental conditions and parameters, special instrumentation design and implementation, experimental measurements or observations, analysis and evaluation of results, and report preparation.

Special areas of consideration were the highly transient effects of the earth's atmosphere in the performance of imaging and measurement of space objects, the limitations of practical optical telescopes, sensor behavior and their special characteristics, illumination phenomena, and the nature of observable data and how they are recorded, processed, and utilized. Other factors were also of concern, but were of lesser importance to this particular effort. These included such items as weather factors, logistics problems, and operational aspects. Related areas of consideration were missile and satellite detection, tracking, and identification programs involving aircraft and spacecraft based instrumentation. Additional areas of consideration broadly involved planetary and stellar astronomy techniques, optical communication, laser technology, image intensifier and television camera tube development, electronic data processing, and image data correlation.

TASK I. ELECTRO-OPTICAL IMAGING DEVICES

A. SIT CAMERA TUBE

Until a few years ago, the camera tube most often used for night viewing was the intensifier image orthicon (IIO or I^2O). More recently, the intensifier SEC camera tube (ISEC) has become popular because of its small size and less complicated and lighter electronics, but it is fragil and expensive to make.

The newest low-light camera tubes are the SIT (silicon intensifier target) by RCA, the EBS (electron-bombarded silicon) by Westinghouse, and the IDAC (intensified diode array camera) by the U. S. Army. Each tube uses a silicon diode array charge storage target in the electron imaging mode of operation (sometimes called impact ionization mode).

This new type of target shows vast improvement in target gain, which causes the SIT to be an extraordinarily sensitive device.

1. Silicon Target

Silicon planar technology was first developed for camera tube operation by Bell Laboratories when they were searching for a sensitive, inexpensive, long-life camera tube to be used in picture phones. Silicon has very attractive photodetection properties such as wide spectral response and high quantum efficiency.

Typically, the silicon target consists of a two-dimensional array of tiny silicon diodes (80 diodes per mm spacing) that are formed in an N-doped silicon wafer by means of integrated circuit planar technology. The diodes are situated with the P-region facing the scanning electron beam. A resistive sea covers the exposed N-regions between the P-regions to prevent contact of the electron beam with the wafer substrate. This prevents the substrate from charging negatively, which would cause the electron beam to be reflected away from the diodes and would result in a drastic decrease in signal output.

We shall first discuss the silicon target when it is used in the photon input mode. In photon operation, the diodes are reversed-biased to about 10 V, and the electron beam side of the target is held at near cathode potential (0 V) by the scanning electron beam. Each reversed-biased diode forms an elemental storage capacitor. Between scans, some of the charge on the array is locally neutralized by incident photon flux and forms a charge image proportional to the light image focused on the target. The next scan of the electron beam recharges the array, and the resulting charging current (the video signal) is capacitively coupled to the video amplifier.

The absorption of photons creates electron-hole pairs, and these holes are swept across the depletion region to the P-type region. Because all the holes reaching a diode during scan time contribute to the discharging of the diode, the signal current is proportional to the integrated local photon flux.

We shall next consider the case where the silicon target is used in the photoelectron input mode. The silicon target can also be used in an electron impact ionization mode in which high-energy photoelectrons emitted from a photocathode are accelerated to the target with energy on the order of 5 to 11 keV. Photoelectrons with this level of energy interact with the silicon target and create a large number of electron-hole pairs for each primary photoelectron. The holes diffuse to the diode depletion region and discharge the elemental capacitor. The gain of the target operating in this mode can reach a value of 2000 or more

electrons per photoelectron at −10 kV photocathode potential, thereby making the SIT an extremely sensitive camera tube operating near photon statistical noise levels. The silicon target is quite rugged, and can also withstand very high light overloads without target burn or damage.

The SIT resolution is ultimately limited by the diode spacing, the target size, and the resolution of the intensifier stage. Camera tubes with diode spacings of 12 to 15 μm and target diameters of 16 mm are currently being manufactured, but spacings of 8 μm are being investigated in order to improve the SIT imaging characteristics. Target diameters of 27 mm are now available that substantially improve the resolution. The SIT is currently manufactured in three photocathode sizes: 16 mm, 25 mm, and 40 mm. The photocathodes are deposited on fiber optics to allow coupling to additional stages of image intensification.

2. ISIT Testing

The intensified SIT (ISIT) camera we tested was an RCA SIT 21117A camera tube with a Varo 8605 No. 1 single-stage intensifier in dry contact. Both tubes had 40-mm-diam photocathodes. High voltage for both devices was provided by a simple resistive 2:1 voltage divider. Half the applied high voltage appeared across each tube; thus, the anode of the Varo intensifier was at the same potential as the photocathode of the SIT. The camera had sufficient gain to be photon noise limited.

A test was devised to measure the S/N (signal-to-noise ratio) of the ISIT camera tube at various gain settings. The gain is adjusted simply by changing the high voltage of the Varo intensifier and the SIT intensifier.

A calibrated Kodak step wedge was used to vary the irradiance. Only six steps of the 21 available steps were used because the SIT has a linear transfer characteristic and the S/N, even at minimum gain, is not high enough for detecting more than seven levels (including a "no filter" position). The transmission of the gray steps is listed below. Table 1 lists the S/N at various levels of irradiance and gain.

Step	Transmission	Irradiance ratio
no filter	1.0	1 1
1	0.78	1.3 1
2	0.42	2.4 1
3	0.25	4 1
4	0.15	6.7 1
5	0.089	11 1
6	0.049	20 1
7	0.029	34 1
8	0.018	56 1
9	0.011	91 1
10	0.0069	150 1

The video preamplifier noise was measured and found to be 19 mV root mean square (rms) at the measuring point. This level of noise was measured with the camera tube operating but with no high voltage applied. In all cases, the noise from the ISIT was higher

Table 1. Signal-to-Noise Ratio of ISIT at Various Intensity Levels, Lens Settings, and Photocathode Voltages

Measurement parameter	Step	Rms noise (mV)	Signal (V)	S/N_s	Integrated faceplate irradiance (W/m^2)
Intensity = 2.58 V, lens setting = f/8, photocathode voltage = −4.6 kV	Clear	52	2.7	52:1	4.4×10^{-6}
	1	45	1.9	42:1	3.4×10^{-6}
	2	38	1.2	32:1	1.9×10^{-7}
	3	31	1.7	23:1	1.1×10^{-7}
	4	28	0.5	18:1	6.6×10^{-8}
	5	25	0.4	16:1	4.0×10^{-8}
	6	23	0.3	13:1	2.2×10^{-8}
Intensity = 19.1 V, lens setting = f/8, photocathode voltage = −5.6 kV	Clear	60	2.4	40:1	1.6×10^{-6}
	1	50	1.8	36:1	1.3×10^{-6}
	2	40	1.2	30:1	6.7×10^{-7}
	3	36	0.8	22:1	4.0×10^{-7}
	4	30	0.5	17:1	2.4×10^{-7}
	5	26	0.4	15:1	1.4×10^{-7}
	6	24	0.3	13:1	8.0×10^{-8}
Intensity = 10.0 V, lens setting = f/8, photocathode voltage = −7 kV	Clear	80	2.6	33:1	2.2×10^{-7}
	1	74	2.1	28:1	1.7×10^{-7}
	2	57	1.3	23:1	9.2×10^{-8}
	3	46	0.9	20:1	5.5×10^{-8}
	4	37	0.6	16:1	3.3×10^{-8}
	5	30	0.45	15:1	2.0×10^{-8}
	6	27	0.3	11:1	1.1×10^{-8}
Intensity = 8.5 V, lens setting = f/8, photocathode voltage = −8 kV	Clear	94	2.6	28:1	9.6×10^{-8}
	1	87	1.9	22:1	7.5×10^{-8}
	2	70	1.2	17:1	4.0×10^{-8}
	3	55	0.8	15:1	2.4×10^{-8}
	4	46	0.6	13:1	1.4×10^{-8}
	5	36	0.5	14:1	8.6×10^{-9}
	6	29	0.3	10:1	4.8×10^{-9}
Intensity = 5.0 V, lens setting = f/8, photocathode voltage = −15.5 kV	Clear	235	2.3	10:1	4.5×10^{-9}
	1	200	1.7	9:1	3.5×10^{-9}
	2	170	1.0	6:1	1.9×10^{-9}
	3	145	0.7	5:1	1.1×10^{-9}
	4	105	0.5	5:1	6.7×10^{-10}
	5	76	0.35	4.5:1	4.0×10^{-10}
	6	65	0.25	4:1	2.2×10^{-10}
Intensity = 5.0 V, lens setting = f/16, photocathode voltage = −22 kV	Clear	270	1.6	6.0:1	1.1×10^{-9}
	1	260	1.2	4.5:1	8.6×10^{-10}
	2	200	0.8	4.0:1	4.6×10^{-10}
	3	105	0.6	3.5:1	2.8×10^{-10}
	4	125	0.4	3.0:1	2.8×10^{-10}
	5	100	0.3	3.0:1	9.9×10^{-11}
	6	. . .	. . .	. . .	. . .

than the preamplifier noise. Note that the S/N is the ratio of peak video signal to the true rms noise contained *in* the signal and not the noise in the black portion of the video signal as is sometimes measured. Because the ISIT is sensitive, photon noise dominates when the ISIT is operated at high gain.

We call this signal-to-noise ratio S/N_s, or the signal-to-noise-in-signal ratio, and plot it in Fig. 1. Notice that as the gain increases the *peak* S/N_s decreases until we reach an S/N_s of 20:1. At an S/N_s of 20:1 and −8 kV high voltage, the irradiance is 6×10^{-8} W/m^2. At a photocathode voltage of −4.6 kV, a 20:1 S/N_s is obtained at 8×10^{-7} W/m^2. Thus, we have realized a net gain in sensitivity (at S/N_s of 20:1) of 13:1. However, as the gain is increased further, the S/N_s decreases to a nearly constant value of 3.5:1.

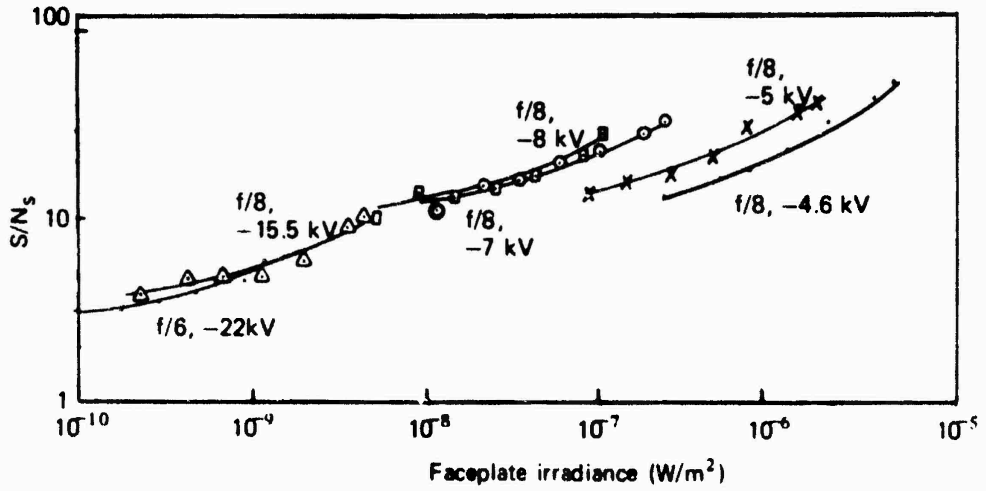

Fig. 1. S/N_s at various ISIT gains.

Such a value of S/N_s may seem so low as to be of little value in detecting and observing satellites, but in reality it is sufficient to determine all but very fine detail. Coltman and Anderson (1959) show that the threshold S/N for detecting the presence of vertical lines on a CRT (cathode ray tube) is much less than unity for even high frequencies on the order of 1000 TV lines per picture height. They also determine that the threshold S/N decreases linearly with frequency until the size of the CRT becomes a limiting factor. Rosell et al. (1968) determined that a S/N of 3.5:1 is necessary to detect squares of various image brightness with a probability of 0.5 or better. Of course, we must realize that periodic test objects (as used in the Rosell et al. study) are inappropriate for determining the threshold S/N because periodicity leads to subjective determinations based on memory, familiarity, or expectation. Nevertheless, the results of detectability research indicate the tremendous integrating and discriminability characteristics of the human eye.

We measured the resolution of the ISIT at various irradiance levels and S/N_s, and the results are shown in Table 2 and plotted in Fig. 2. An interesting aspect of this figure is that the resolution was higher at middle frequencies in the presence of noise (a poorer S/N). Not only did this effect show up in the data, but also was observable to the eye when viewing the TV monitor. Figure 3 shows the variation of relative gain with photocathode voltage for the ISIT.

Table 2. ISIT Resolution at Various Intensity Levels, Photocathode Voltages, and Irradiances

Frequency		Relative response *		
(lp/mm)	(TV lines/picture height)	Case 1	Case 2	Case 3
2.26	110	0.57	0.56	0.56
3.5	170	0.43	0.44	0.51
4.5	220	0.29	0.28	0.38
5.7	280	0.17	0.16	0.28
6.8	330	0.11	0.11	0.09

*Case 1: Intensity = 10 V, photocathode voltage = −8 kV, peak faceplate irradiance = 2×10^{-7} W/m^2
Case 2: Intensity = 8.5 V, photocathode voltage = −9.5 kV, peak faceplate irradiance = 8.6×10^{-8} W/m^2
Case 3: Intensity = 5.1 V, photocathode voltage = −20 kV, peak faceplate irradiance = 4×10^{-9} W/m^2

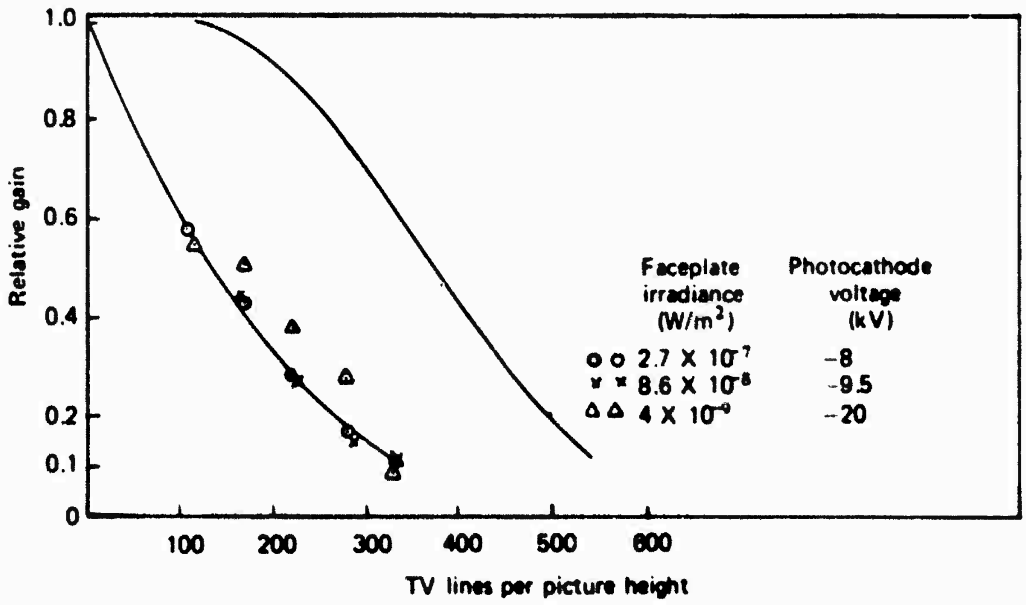

Fig. 2. ISIT resolution.

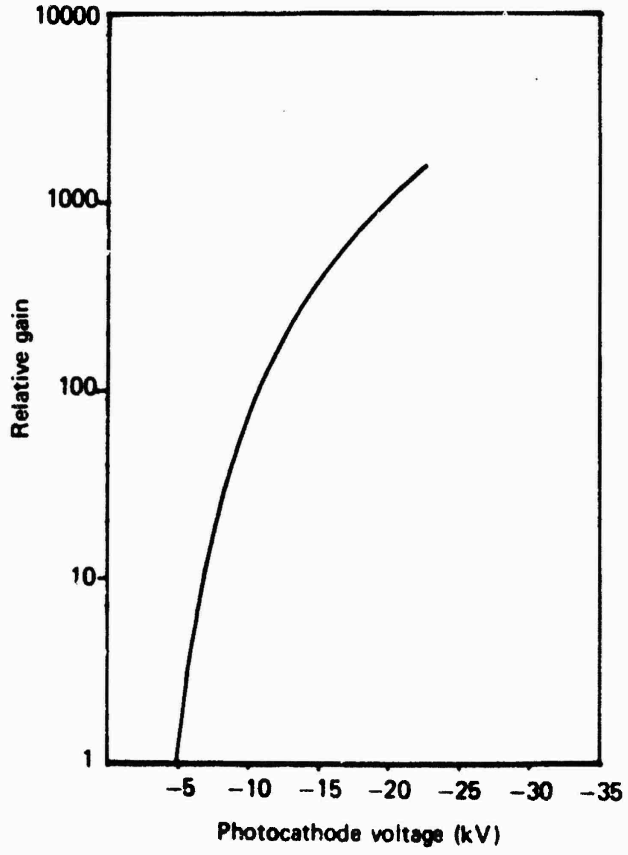

Fig. 3. ISIT relative gain versus high voltage.

Before the response of each frequency burst was plotted, it was corrected for the shading in the signal. The shading varies as a function of high voltage applied, and each single line trace and the responsivity of each frequency burst were individually corrected and normalized.

Photographs of various test objects were obtained, including the photograph of a simulated Apollo spacecraft shown in Fig. 4a. We imaged this photo with the ISIT camera tube, displayed the picture on a TV monitor, and photographed the CRT display for different S/N_s and different integration times.

Figure 4b shows the result for a S/N_s of 45:1, while Fig. 4c shows the same object but with a S/N_s of 5:1. Both photos were imaged at an integration time of 1/30th sec (1 TV frame). Figure 4d shows the result of integrating 10 TV frames with an input S/N_s of 5:1. The improvement of Fig. 4c over Fig. 4d is not surprising because we would expect an increase in S/N with increased integration time. Figure 5a shows a special resolution chart, photographed with a S/N_s of 45:1, and Fig. 5b shows the same object photographed with a S/N_s of 5:1, using an integration time of 1/30th sec.

The noise in all the above photographs is predominantly photon noise. Referring again to Fig. 1, we can draw a smooth line along the data points from 10^{-10} W/m^2 to 2×10^{-7} W/m^2. The resulting line has a slope of 0.5, which indicates photon noise.

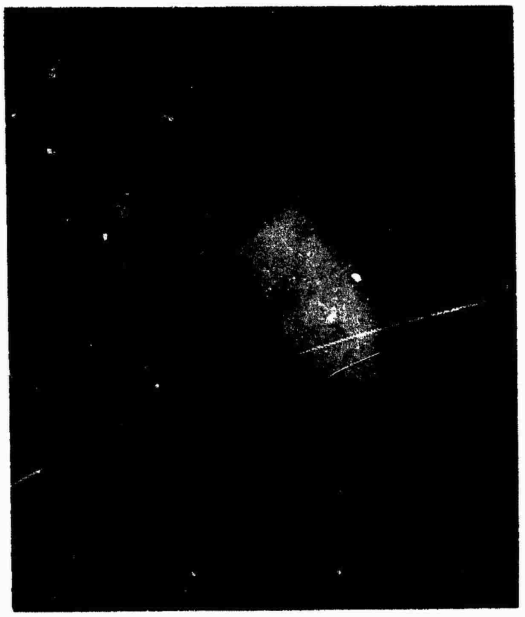

(a) Original photograph

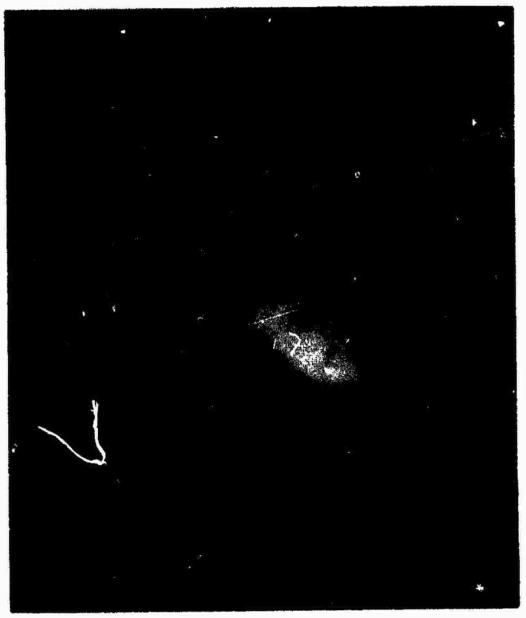

(b) Imaged at S/N_s of 45:1 and 1/30-sec integration time.

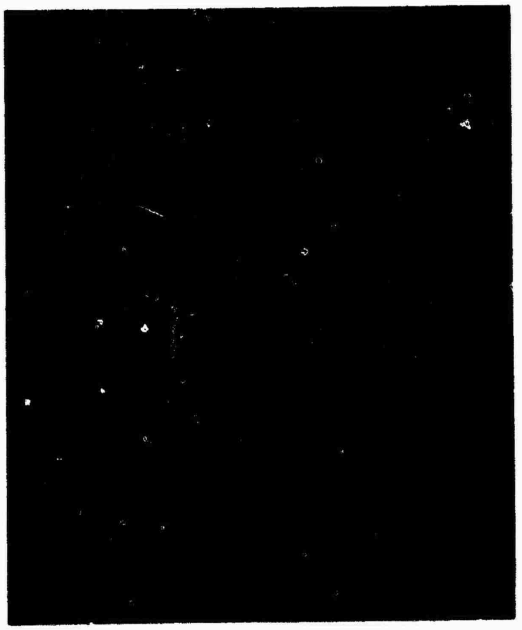

(c) Imaged at S/N_s of 5:1 and 1/30-sec integration time.

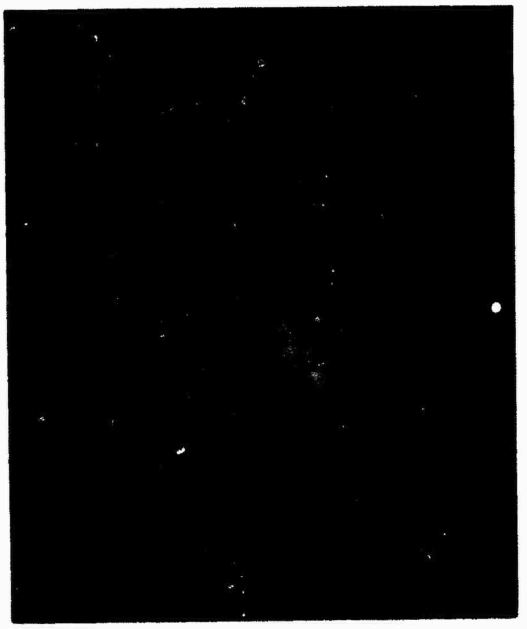

(d) Imaged at S/N_s of 5:1 and 1/3-sec integration time.

Fig. 4. Simulated Apollo spacecraft imaged with ISIT camera tube, displayed on a TV monitor, and photographed.

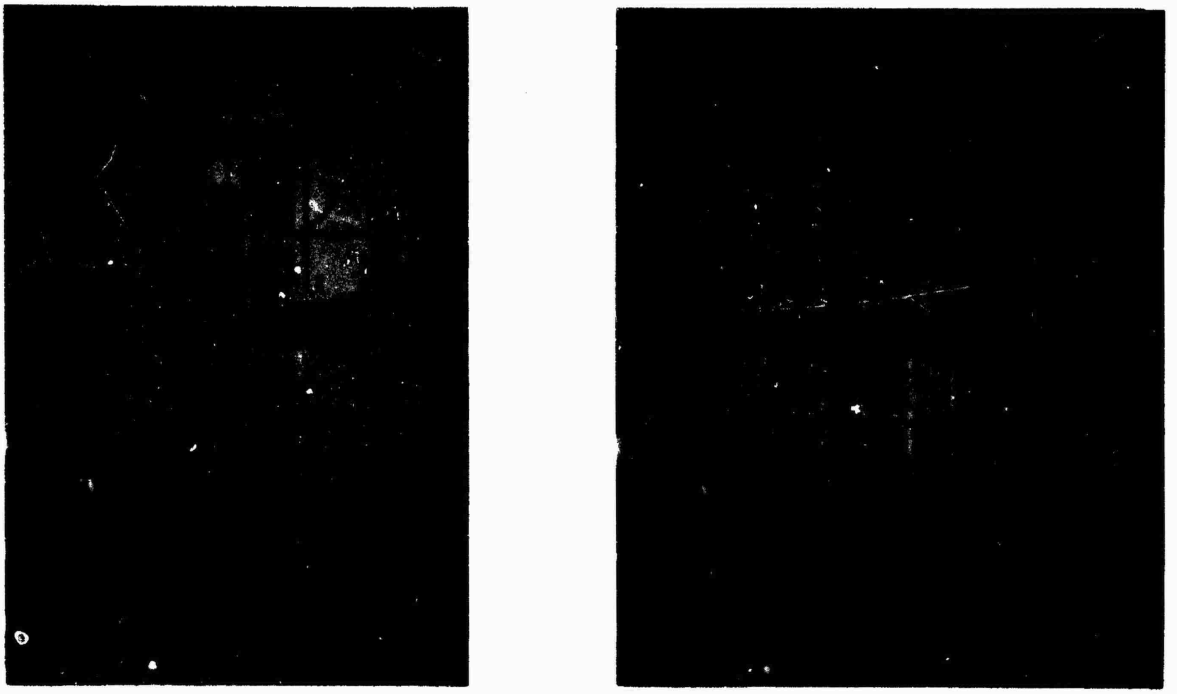

(a) $S/N_S = 45:1$.

(b) $S/N_S = 5:1$.

Fig. 5. Resolution chart imaged at 1/30-sec integration time.

3. Resolution

The SIT without an intensifier will typically have resolution as indicated in Table 3.

Table 3. SIT Resolution

Camera tube type	Mfg.	Photo-cathode diam (mm)	Target diam (mm)	Input image format (mm)	10 % response (lp/mm)	10 % response (TV l/p.h.)	Maximum No. pixels
C21145	RCA	40	27	32 X 24	17	820	975,000
21117C	RCA	40	16	32 X 24	12.5	600	480,000
21130	RCA	25	16	20 X 15	21	630	530,000
4804	RCA	16	16	127 X 9.5	32	600	480,000
WX31841	WEST.	40	?	32 X 24	15	720	690,000
WX31793	WEST.	25	16	20.3 X 15.2	25	600	610,000
WX31960	WEST.	16	16	12.7 X 9.5	31	590	464,000

The highest resolution SIT, in terms of line pairs per mm, is the RCA 4804 or Westinghouse WX31960, which are 16-mm-diam photocathode devices. The device with the highest resolution in terms of TV lines per picture height is the RCA C21145 40-mm-diam photocathode with a 27-mm-diam target. The larger format size of the C21145 provides far more

pixels as can be seen in the table. Figures 6a and b show the resolution data plotted in terms of line pairs per millimeter and TV lines per picture height for comparison. Any deficiency in resolution from small images, as we expect at Cloudcroft, can be compensated by enlarging the image on the photocathode.

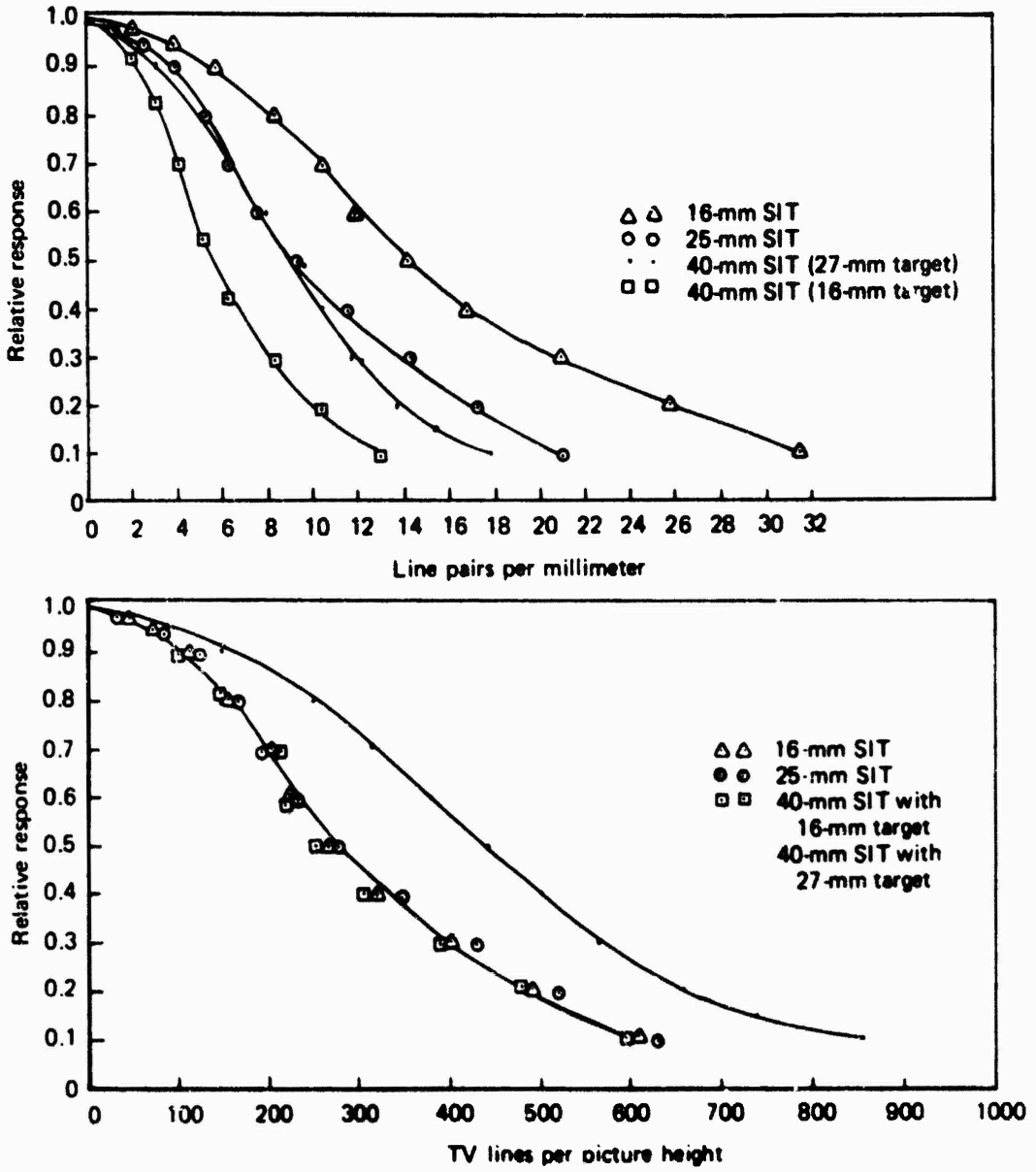

Fig. 6. Resolution of various SIT camera tubes.

The sensitivity of the SIT is not sufficiently high to be classified as a photon-noise-limited device, therefore, additional gain must be added in the form of an intensifier stage. We can choose between fiber optic coupling or relay lens coupling to transfer the image from the intensifier to the SIT. In either case, the SIT resolution will be the limiting resolution of the system.

For our testing program, we used an SIT with a 40-mm-diam photocathode coupled to a single-stage 40-mm-diam intensifier by fiber optics. Our measurements indicated a limiting resolution of 7.5 lp/mm, whereas a limiting resolution of 12.5 lp/mm was obtained without the intensifier. The resolution of the intensifier alone was measured to be greater than 50 lp/mm, and the resolution of the ISIT was calculated to be 11.7 lp/mm. This calculation assumes good coupling between the fiber optics, i.e., that the two surfaces are extremely flat, clean, and in intimate contact. In our case, neither surface was lapped nor polished, and this could explain the lower value measured for resolution.

If the Cloudcroft telescope is used at a focal length of 8 m, and the resolution is about 1 arc sec (including the atmosphere), then the diameter of each resolution element is 50 μm, which corresponds to a resolution of 20 lp/mm at the camera tube faceplate.

4. Sensitivity

Figure 7 shows the relative sensitivities and light transfer characteristics of SIT and ISIT camera tubes that are currently available. As we would expect, the photocathode diameter affects the camera tube sensitivity. As was stated earlier, none of the SIT devices are sufficiently sensitive, and an intensifer must be added to supply the required gain to enable true photon-noise-limited operation.

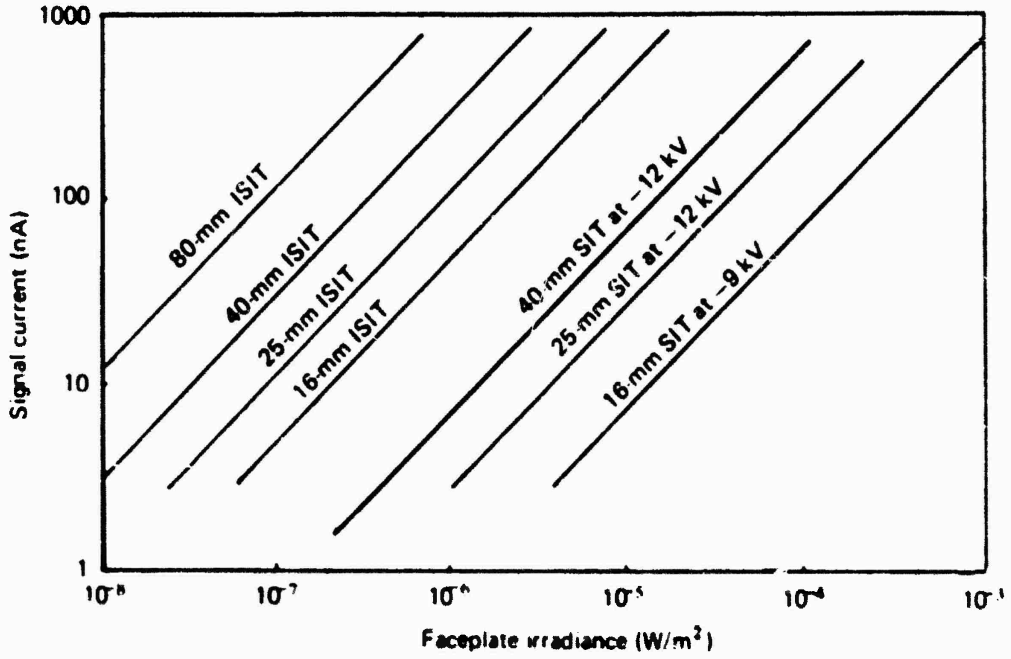

Fig. 7. Typical sensitivities of various SIT camera tubes.

For satellite observations, we expect a very poor object S/N, and the TV camera system S/N should therefore be limited by the statistical arrival of photons. We expect the general image size to vary from 0.1 mm diam to as large as 1 mm diam, and, by choosing the proper lenses in the telescope relay system, we can easily enlarge the image to fill the active raster on the ISIT.

5. Blemishes

It should be noted that the SIT target consists of an array of over 500,000 photodiodes. Not all diodes can be expected to be perfect, and manufacturers publish specifications for the number and size of spots contained within specified areas of the active image format. Different grades of SIT's are available with different spot specifications. Naturally, the camera tube with the least number of spots is by far the most expensive.

For satellite observations, it is our feeling that some spots in the format will not be objectionable.

6. Environmental Considerations

Environmentally, the ISIT is fairly rugged. The temperature opeating range is $-10°C$ to $+60°C$, and the temperature storage range is $-54°C$ to $+70°C$. Because of the altitude at Cloudcroft, some heating may be required for an ISIT camera during winter month operations. Operation at temperatures between $0°C$ and $+10°C$ may be desirable from dark current considerations because the dark current in silicon is reduced by half for every $10°C$ temperature drop.

7. Overload

In satellite observations, specular reflections are very likely to occur, so we may ask the question, how will the ISIT handle overloads? The answer is that no permanent damage will result, but severe loss of data may occur owing to spot blooming around the reflection. (The image Isocon is the best camera tube on the market to handle specular reflections, but it does not have sufficient sensitivity and is fairly complex, quite costly, and requires a bulky camera tube housing.)

Campana (1971) clearly outlined the problem of imaging bright point sources of light contained in an otherwise dimly illuminated object with low-light television camera tubes. Although we expect specular reflections from observed satellites, it is our opinion that the problem is not serious.

8. Data Processing

The low S/N of the satellite image and the turbulence of the atmosphere are expected to cause difficulty in obtaining high-quality imagery.

We feel that the ISIT TV camera could be used in a mode where several video frames could be stored on magnetic tape or film for later computer superposition and enhancement. At standard TV rates, 30 complete pictures could be stored in a 1-sec interval. If we use a nonstandard scan rate, the frame rate could be increased (accompanied by a proportional increase in video bandwidth) such that 60 frames could be stored in 1 sec or perhaps even less. Further research needs to be done in this area; however, the technique appears feasible for scanning up to 100 frames per sec by using special circuit design techniques in the camera.

9. Conclusions and Recommendations

The ISIT has been tested and found to be truly photon-noise-limited. The intensifier (as

reported by Cromwell in Section C of this chapter) should be a two-stage, magnetically focused intensifier (for low distortion and excellent uniformity), coupled to the SIT by means of a relay lens. Cromwell's data show this to be the best intensifier selection for the Cloudcroft facility. Our camera-tube program indicates that the best camera tube is the new 40-mm-diam photocathode, 27-mm-diam target SIT, such as the RCA C21145. We feel the combination of sensitivity and total number of pixels of this camera tube justifies the selection.

B. CHARGE–COUPLED DEVICES (CCD)

This report would not be complete without a section discussing the latest type of imaging detectors currently being developed in several research centers across the nation (and also abroad).

CCD's were originally developed by Bell Laboratories and were announced in May 1970. Briefly, CCD's store and transfer information in a manner not unlike the old "volunteer fire department bucket brigade." In operation, a potential "well" is created in a semiconductor (silicon, at present) by proper application of voltages. This charge is transferred along the silicon surface in shift register fashion by simple manipulation of the voltages that contain the potential well. CCD's are manufactured from either an N-type or P-type silicon substrate, an MOS-type silicon dioxide (SiO_2) insulation layer, and a metallized electrode on top of the SiO_2. Because it is the potential well that shifts, no P-N junctions are required. P-N junctions are used only for input and output functions in CCD's; therefore, the manufacturing process is very simple.

CCD's are particularly well suited for imaging applications because they are easily manufactured and have excellent spectral response, high quantum efficiency, and few defects. In the past, fabrication defects in solid-state image sensors have plagued the solid state industry. The fabrication of large-area, two-dimensional arrays has been virtually impossible owing to the complicated manufacturing process that is based on conventional planar technology. The much simpler fabrication techniques associated with CCD's will allow much closer element spacing (higher resolution) and higher yields (lower cost) devices, and open the door to true solid-state imaging. Within three or four years, we expect to see two-dimensional arrays of 400 by 500 elements with 2-μm to 3-μm element spacing (including the scanning and video amplifier electronics) to be available off the shelf. These first arrays will probably be costly, but the price should fall rapidly as more and more arrays are produced.

The CCD arrays operate in a very simple manner. Light is focused on the array and for a period of several milliseconds photons are absorbed by the silicon, which creates a charge pattern under the various electrodes. This pattern is an analog replica of the image. By shifting the potential wells in a shift register type of operation (as discussed previously), a train of variable amplitude pulses is routed to the video amplifier and constitutes the video signal. Line arrays and small two-dimensional arrays have been demonstrated in the laboratory and show great promise for the future. For instance, RCA has demonstrated a TV camera using a CCD array of 32 by 44 elements (1408 total), and Bell Laboratories recently demonstrated a 106 by 128 element array (13,568 total elements). The government is spending a large amount of money for developing CCD's into low-light television sensors, and we feel the future in television imaging devices lies in the solid-state area of research, especially since the development of CCD's.

We highly recommend a constant watch on the progress of CCD's because they appear to be a good answer to the satellite observation problem for the future. For the present, however, we recommend an intensified SIT camera tube with a 40-mm-diam photocathode as the image detector.

C. IMAGE INTENSIFIERS

The following is a summary of the laboratory evaluation of 11 image intensifiers tested by the image tube laboratory of the Optical Sciences Center. Full details of these tests are to be published in the near future as an Optical Sciences Center Technical Report, and the present summary gives the significant results of the study without a detailed discussion.

1. Image Intensifiers Tested

Table 4 lists the image intensifiers that have been tested. The types of photocathode and phosphor (as designated by the manufacturer) are shown for each tube. All the tubes have photocathode diameters of nominally 40 mm, with the exception of the EEV P829D tube, which has a photocathode diameter of 25 mm.

2. Resolving Power

Measurements of the resolving power of each intensifier are summarized in Figs. 8, 9, and 10, which show the limiting resolution as a function of field position. These data were obtained by visually inspecting with a microscope the images of a resolution test pattern produced by the intensifiers.

The dependence of resolution on operating time exhibited by the tube in Fig. 10 is unusually strong, and other tubes checked for this effect have shown either no or very minor effects.

Three general conclusions that may be drawn from these figures are (1) resolution is always substantially lower at the field edge than near the center; (2) the detailed dependence of resolution on field position varies considerably from one tube to the next and may be expected to vary even among samples of the same type of tube from a single manufacturer; and (3) for the same number of stages (and therefore approximately the same gain), the magnetically focused tubes have higher resolution and exhibit somewhat less falloff in resolution toward the field edge.

A mean relationship has been found between the limiting resolution of the intensifier output image (designated "phosphor resolution") and the limiting resolution that is recorded on a photograph of the intensifier ("photographic resolution"). The mean relationships for several different photographic emulsions are shown in Fig. 11. The photographs were taken of the intensifiers either by use of a relay lens or, with intensifiers having fiber-optic output faceplates, by directly contacting the photographic emulsion to the faceplate. (The relay lens used was a Nikon Repro-Nikkor 85-mm *f*/1 lens adjusted for 1:1 magnification, and the iris diaphragm was set at *f*/2.)

The lower resolution of the fiber-optically coupled photographs is caused, in part, by the inability to achieve the close contact required between the fiber-optic faceplate and the photographic glass plate. Measurements with a Fizeau interferometer of the flatness of the fiber-optic faceplates indicate that the faceplates are normally very smoothly convex or

Table 4

Image Intensifiers Investigated

a. Electrostatically focused

Manufacturer	ITT	Varo*	Varo	ITT	RCA	Varo
Model	F-4708	8605	8605DC	F-4724	8606	8606
Photocathode	S-20 ext. red	S-20R	S-20R	S-20 ext. red	S-20 ERMA	S-20R
Phosphor	P-20	P-20	P-20	P-20	P-20	P-20
No. of stages	1	1	1	3	3	3
Tube type	F-O I/O**	F-O I/O	F-O I/O	Coupled F-O single-stages	Coupled F-O single-stages	Coupled F-O single-stages

*Two tubes tested
**Fiber-optics input/output

b. Magnetically focused

Manufacturer	EEV	ITT	RCA	RCA
Model	P829D	F-4089	C33011	C70021AEP2
Photocathode	S-20	S-25	S-20	S-20
Phosphor	P-11	P-20	P-11	P-22B
No. of stages	5-dynode	1	2	3
Tube type	TSE*	F-O O**	Cascade	Cascade
Magnet used	EEV P4046 solenoid	ITT perm. magnet	Carnegie Comm. perm. magnet	EEV P4046 solenoid

*Transmission secondary emission
**Fiber-optic output

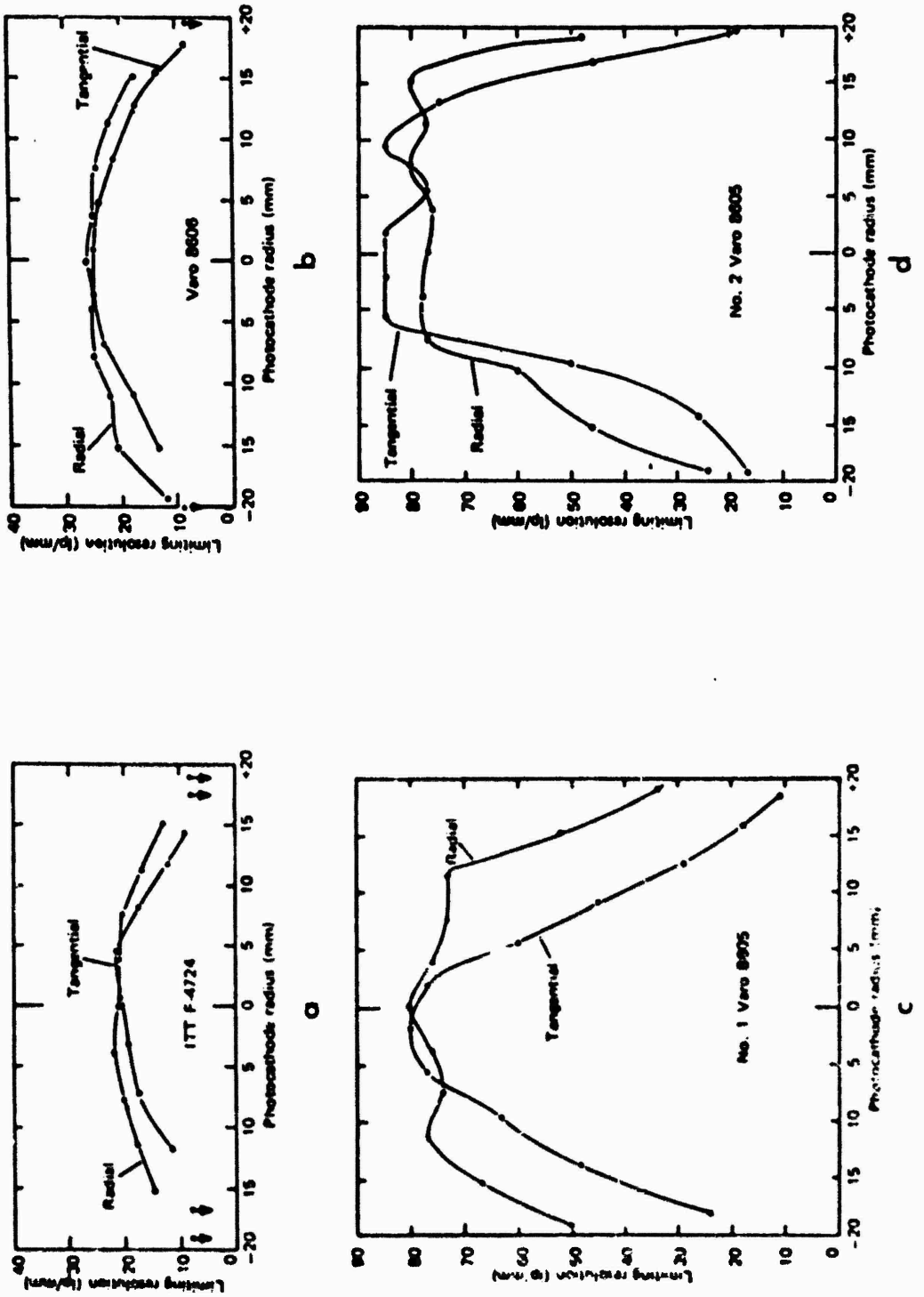
Tangential
Radial
ITT F-4724
Limiting resolution (lp/mm)
Photocathode radius (mm)
a
Tangential
Radial
Vare 8606
Limiting resolution (lp/mm)
Photocathode radius (mm)
b
Tangential
Radial
No. 1 Vare 8605
Limiting resolution (lp/mm)
Photocathode radius (mm)
c
Tangential
Radial
No. 2 Vare 8605
Limiting resolution (lp/mm)
Photocathode radius (mm)
d

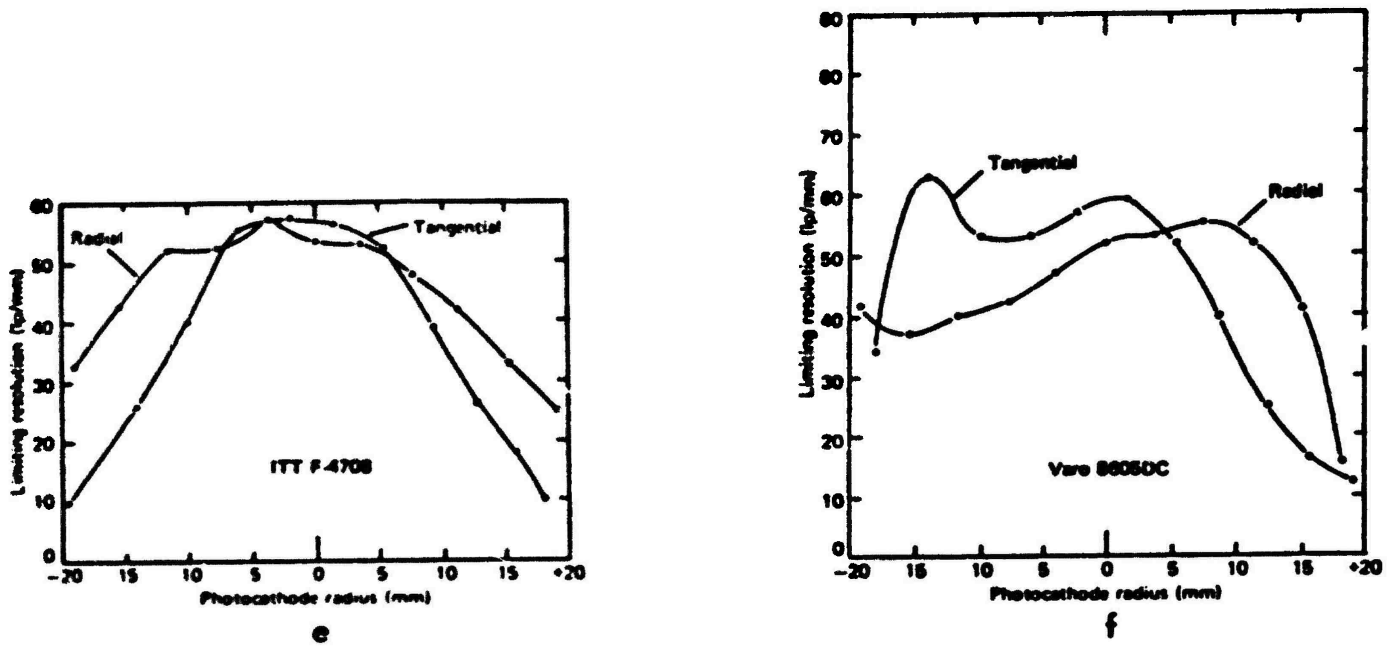

Fig. 8. Limiting resolution across the diameters of the photocathodes of six electrostatically focused image intensifiers. The specified spatial frequency is the frequency incident on the input photocathodes.

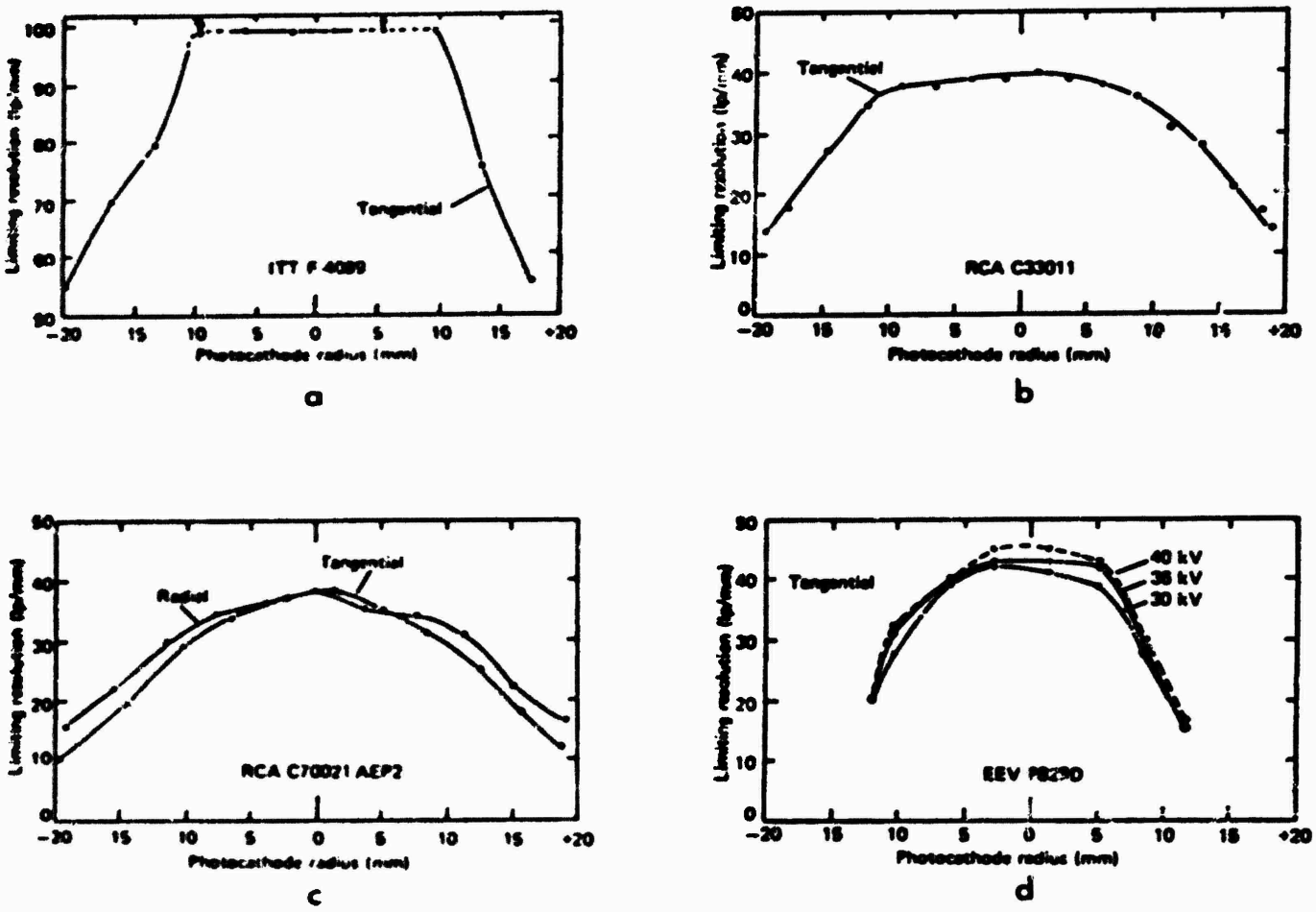

Fig. 9. Limiting resolution across the diameters of the photocathodes of four magnetically focused image intensifiers. Resolution of the tube in (a) exceeded the frequencies available on the resolution target at points represented by arrows.

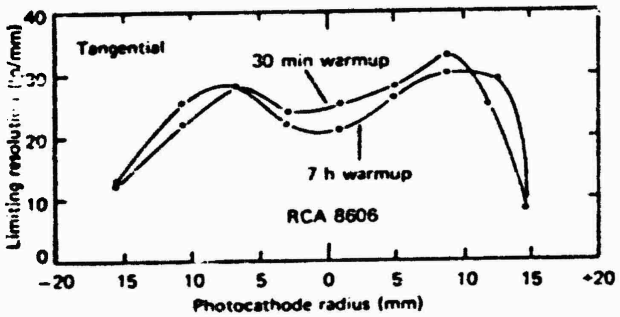

a Tangential resolution profile.

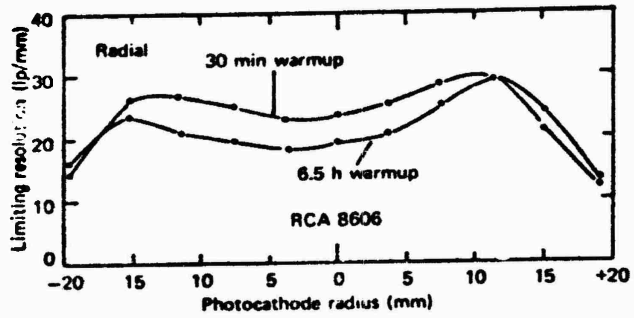

b Radial resolution profile.

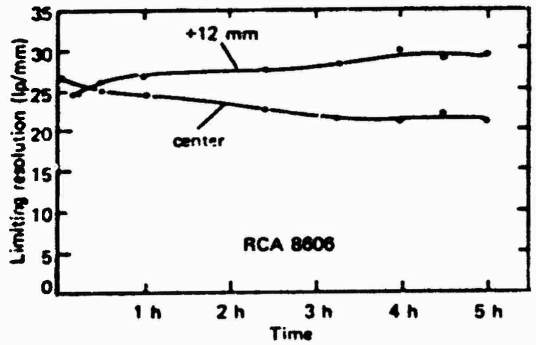

c Change in resolution at two field positions as a function of time.

Fig. 10. Unusually strong dependence of the limiting resolution on warmup time for a three-stage electrostatically focused image intensifier.

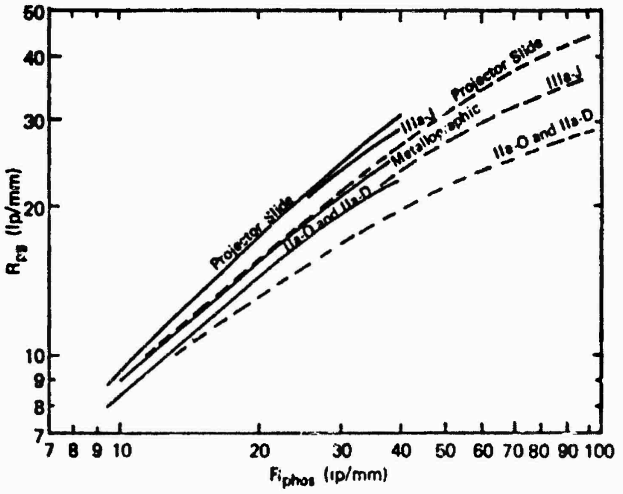

Fig. 11. R_{pg} vs R_{phos} (limiting photographic and phosphor resolutions, expressed as spatial frequency on output side) for nearly all tubes tested. Solid lines (mean curves) refer to relay lens photography, and dashed lines refer to fiber-optic contact photography.

concave, and the maximum deviation from flatness is less than 1 μm. Similar measurements of photographic plates, held in contact with a reference optical flat, indicate that the emulsions typically are in contact with the faceplate only at a few points along the emulsion and that there normally are several regions of the emulsion that are separated from the faceplate by about 3 μm and often by up to 6 μm.

A graphic illustration of the plate flatness problem is given in Fig. 12, which shows a plot of the emulsion surface of a standard 10.2 cm by 12.7 cm by 0.13 cm (4 in. by 5 in. by 0.050 in.) Eastman Kodak plate. Clearly, even a selected 53-mm-diam surface (the diameter of a 40-mm intensifier faceplate) will exhibit a certain amount of plate warpage that will not be removed when the surface is pressed into contact with a flat faceplate.

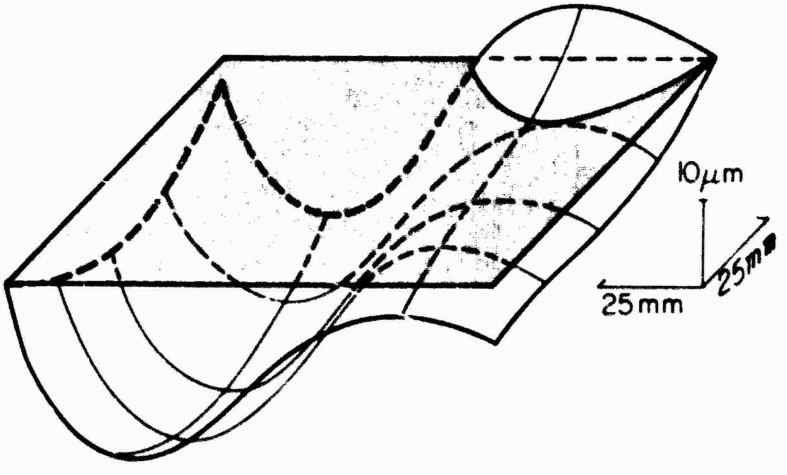

Fig. 12. Diagram of surface of 10.2 by 12.7 by 0.13 cm photographic glass plate. Vertical axis is shown at 2000 times the scale of the horizontal axis. Flat plane is shown to emphasize the shape of the plate surface.

When an intercomparison is made among photographs taken with the same emulsion but with different intensifiers, a photograph exhibiting a higher limiting resolution than another also has equal, or better, modulation at all lower spatial frequencies. Thus, for photographs taken on the same type of emulsion, the limiting resolution is indicative of the modulation transfer function at the spatial frequencies below the limiting value. This is true whether the photographs are obtained using relay lens coupling (at $f/2$) or fiber-optic coupling.

3. Geometrical Characteristics

Photographs illustrating typical geometrical characteristics of six intensifiers are shown in Fig. 13. Measurements obtained with a two-coordinate measuring engine of these and similar photographs are plotted in Figs. 14 through 17. *Magnification* in Figs. 14 and 16 is defined as the ratio of the measured radial distance of a test point in the output to the corresponding radial distance in the input. The magnification data points for each tube in Figs. 14 and 16 are the mean values obtained from measurements along four radii, each separated in position angle by 90°. *Incremental magnification* in Figs. 14 and 15 is defined as the output-to-input ratio of the radial separation of points that are separated by about 1 mm in the input image. Results for each of the four different position angles are denoted by a separate symbol. *S-distortion*, present in magnetically focused tubes only, is defined as the deviation that is experienced off axis by the image of a straight line that passes through the center of the field (see Fig. 13f). For all the magnetic tubes studied, mean values of *S*-distortion from the four position angles are given in Fig. 17. *Field rotation*, also present only in magnetically focused tubes, is defined as the angular rotation experienced by the image of a small line segment that passes through the center of the field (compare Figs. 13d and e). Values of field rotation are given in Table 5.

Table 5

Field Rotation in Magnetically Focused Tubes

Image tube	Field rotation (degrees)
EEV P829D	0
ITT F-4089	5
RCA C33011	7
RCA C70021AEP2	10

Figure 15, which is representative of the magnetic tubes, shows that there are substantial differences in image geometry at different position angles. This trend is considerably smaller but also noticeable in the electrostatic tubes. The approximate total spread at different position angles is as follows:

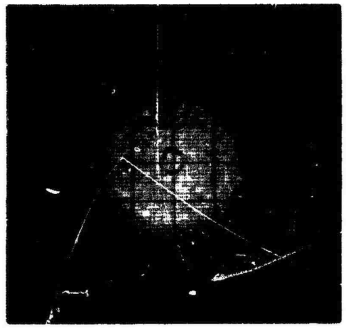

(a) ITT F-4708

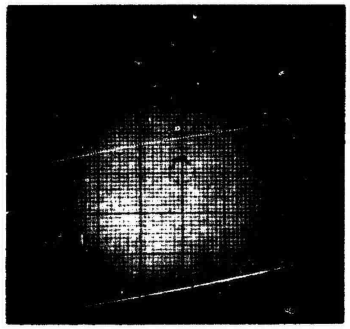

(b) Varo 8605DC

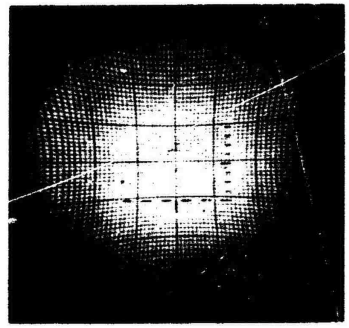

(c) RCA 8606

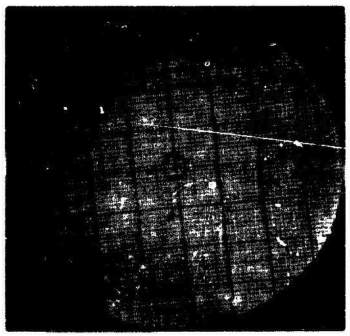

(d) ITT F-4089

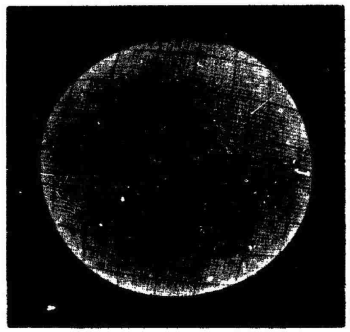

(e) RCA C70021AEP2

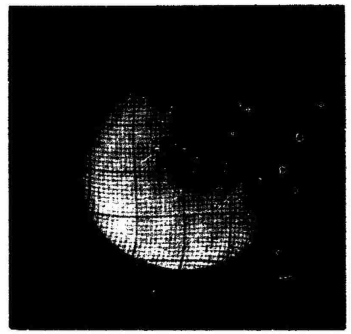

(f) EEV P829D

Fig. 13. Geometrical characteristics of six image intensifiers. The image rotation produced by the magnetic tubes is shown. The tonal range on the prints has been individually compensated for sensitivity profiles.

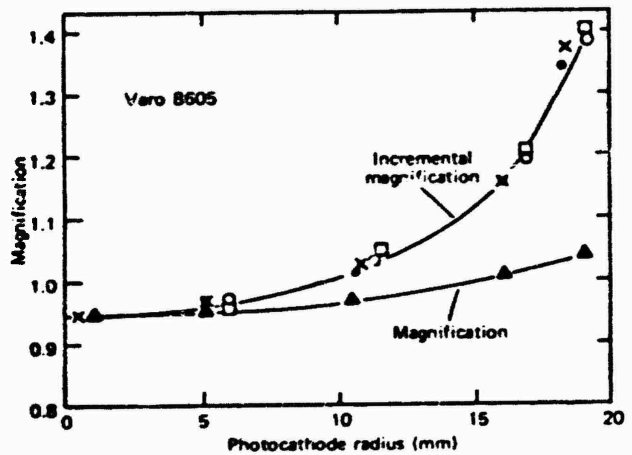

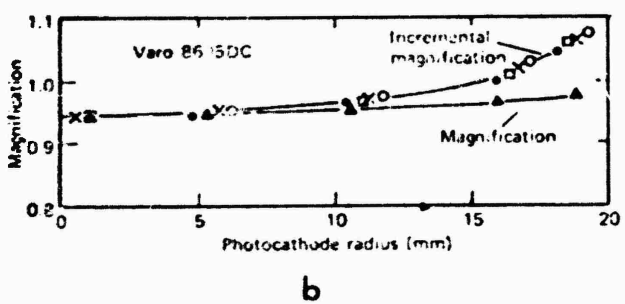

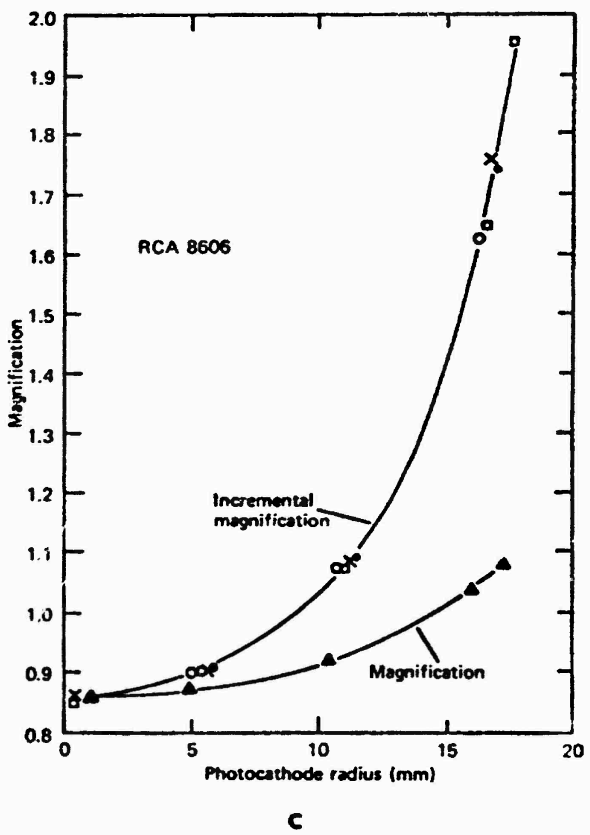

Fig. 14. Magnification and incremental magnification of three electrostatically focused image intensifiers. The four orthogonal position angles measured are identified by the following four symbols: □and X for position angle, 0° and 180°; ●and ○ for 90° and 270°. Points shown for magnification (▲) are the average of four position angles.

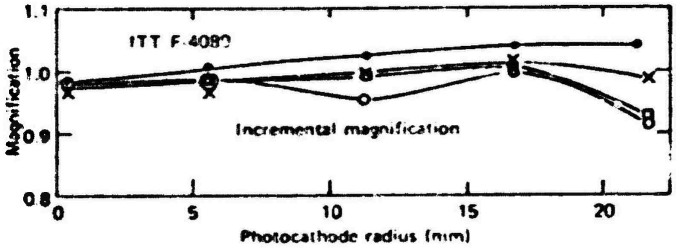

Fig. 15. Incremental magnification at four different position angles of a magnetically focused image intensifier. The symbol explanation is the same as for Fig. 14.

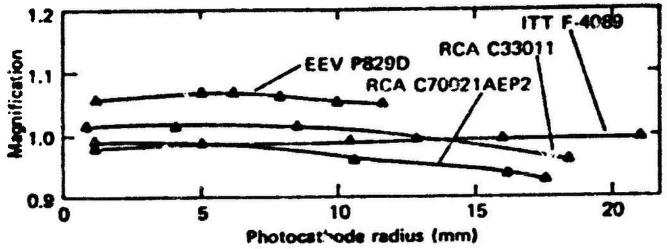

Fig. 16. Magnification of four magnetically focused image intensifiers. The mean values from four position angles are given.

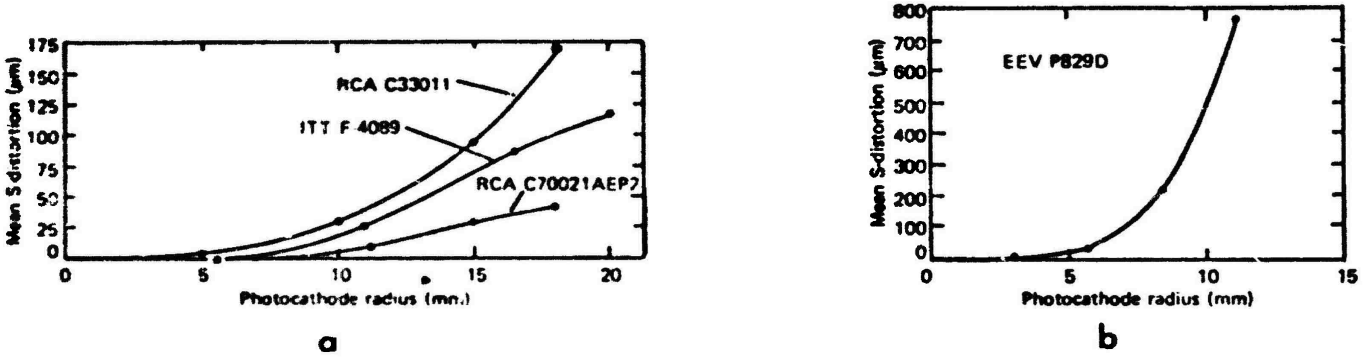

Fig. 17. Mean values of S-distortion of four magnetically focused image intensifiers. Note the change in the vertical scale between (a) and (b).

	Electrostatic tubes (%)	Magnetic tubes (%)
Incremental magnification	2.0	10
Magnification	0.1	2
S-distortion	--	100

When allowance is made for the number of stages, all the electrostatic tubes, with the exception of the distortion-corrected Varo 8605DC, have nearly identical pincushion distortion. It should be pointed out that the smaller distortion found with the Varo 8605DC tube, which utilizes a more steeply curved fiber-optic anode, is obtained at the expense of reduced light output toward the edge of the field (see Figs. 21 and 22).

The magnetic tubes tend to have superior geometry for approximately the same gain or number of stages. However, their unique *S*-distortion and field rotation can be troublesome in certain applications.

A general conclusion regarding nearly all the geometrical characteristics discussed above is that in applications where high positional accuracy is required, detailed calibration of the image tube geometry is essential. Clearly, there are instances where use of a simple analog correction function will be insufficient to account for the local variations in geometry (compare especially the following discussion on fiber-optic shear).

4. Shear in Fiber-Optic Faceplates

A problem that can adversely affect positional data from image intensifiers with fiber-optic faceplates is shear in the fiber optics. A rather extreme case is shown in Fig. 18. This particular faceplate contained shear lines throughout the field that produced image shifts of typically 40 μm. Nearly all the fiber-optic tubes were found to have about five or more regions, each typically 2 mm in length, that produce image shifts of 10 to 20 μm. It has been our experience that the fiber-optic plates made up of hexagonal arrays have less shear than those with square arrays.

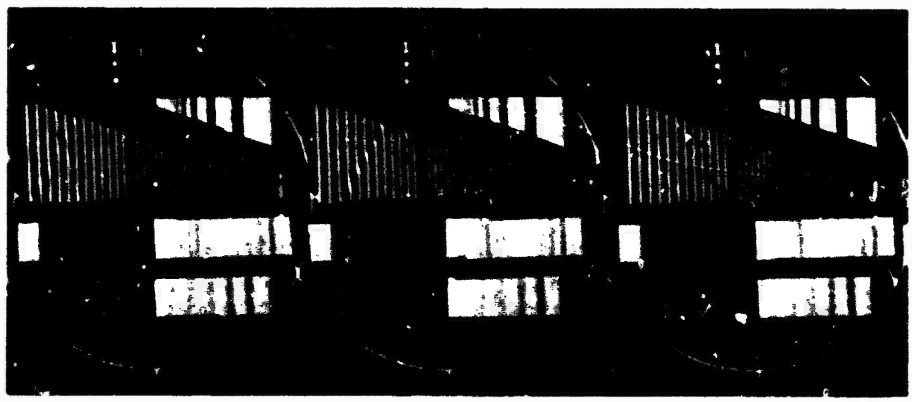

Fig. 18. Contact photograph with IIa-D emulsion showing a fiber-optic faceplate with several shear lines.

A thorough study of fiber-optic shear has been carried out on four unmounted fiber-optic plates that were designed to be used as image intensifier faceplates. They were loaned to the University of Arizona Steward Observatory by ITT in Fort Wayne, Indiana, and they were originally selected by ITT and the faceplate manufacturer from a set of 20 such faceplates for their freedom from shear and fiber-bundle pattern. The useful diameter of each faceplate is 4.45 cm, and the thickness is 0.90 cm. The faceplates were manufactured by Bendix, Mosaic Fabrications Division. Two of these particular plates, we feel, represent the very best fiber-optic plates currently available.

Results of studying contact photographs of a Ronchi ruling obtained with the fiber-optic faceplates are given in Table 6 and Fig. 19. Here, one shear is defined as one side of a hexagonal element of the faceplate, which is about 0.58 mm long. If image displacement occurs at all six sides of the hexagonal element, it is counted as six shears. We have found that an exponential function of the form

$$P = C\exp(-\alpha d)$$

fits the observed size distribution rather well for shears producing image displacements of 5 μm or greater (see Fig. 19). However, the real distribution is more peaked around 0 μm than an exponential function. For example, the percentage of shears in the size region 0 μm to 4 μm that is predicted from the best-fit exponential is 11.5% as compared to the real value of 94.1%.

It should be remembered when predicting the effects of shear in image intensifiers utilizing fiber-optic faceplates that the present faceplates represent the very best plates currently available, that the shear sizes will be approximately proportional to the thickness of the faceplate used, and that multiple-stage tubes (such as the electrostatic tubes tested here) commonly use several fiber-optic faceplates.

5. Photographic Speed Gain

Measurements of microdensitometer traces of photographs taken at the field center of each image tube have provided the value of the input exposure that is necessary for producing a photograph with a density of 0.6 above fog. These measurements are a test of the sensitivity of the entire image tube system, which consists of the intensifier, the phosphor output transfer component (relay lens or fiber-optic faceplate), and the photographic emulsion. The Baum test pattern was used as the input image for all the exposures (see Fig. 20a for spectral energy distribution), and the exposure times were kept near the same value (10 sec) in all cases to avoid reciprocity failure effects. The photographic densities were measured with a Joyce-Loebl microdensitometer.

Figure 20b gives the spectral response of a representative S-20 photocathode (Electronics Industries Association, 1964) and an S-20R, extended red, photocathode on a fiber-optic faceplate (Varo, Inc., 1972). The radiation from the electroluminescent panel matches both photocathode responses about equally well.

IIa-D emulsion was used to photograph the image intensifiers having P-20 output phosphors, and IIa-O emulsion was used for intensifiers having P-11 output phosphors. These two emulsions, with their respective spectral sensitivities, have been found to be optimum for recording the P-20 and P-11 phosphors, respectively. Both emulsions are characterized by high sensitivity, good resolving power, and moderate information storage capacity.

Table 6

Identifiable Shears in Four Selected Fiber-Optic Plates

Plate	Total No. on faceplate (area = 15.5 cm^2)	No. /cm^2
A	315	20.3
B	327	21.0
C	401	25.8
D	511	32.9

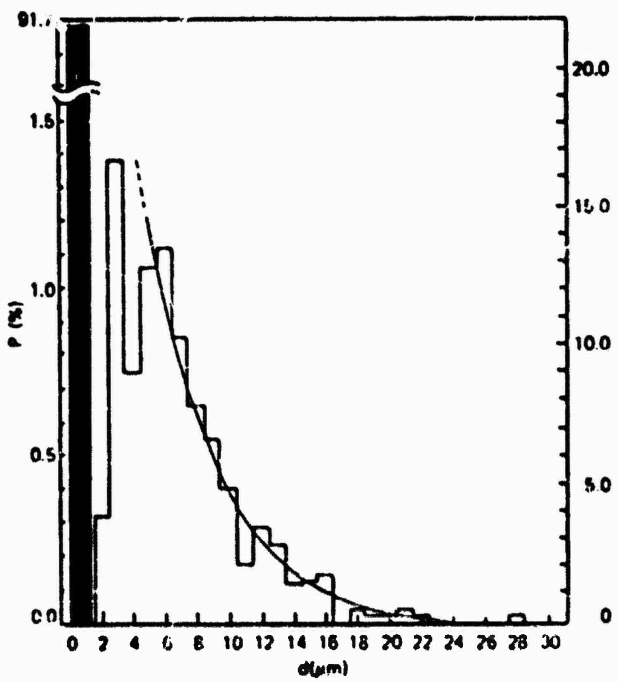

Fig. 19. Mean size distribution of fiber-optic shear in two selected fiber-optic faceplates 0.90 cm thick. The size of the displacement produced by the shear is d. The ordinate scale at left is the percentage of interfaces of the entire faceplate that produced the image displacement d. The black bar near 0 μm represents the percentage of interfaces with no detectable shear. The scale to the right is normalized so that the total number of identifiable shears (those with $d>0$) is 100%. The best-fit exponential curve is shown.

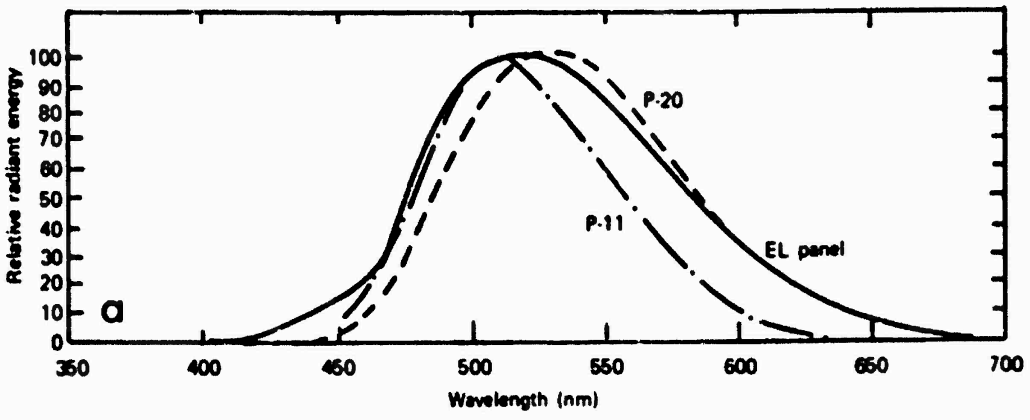

Spectral energy distributions of P-11 and P-20 phosphor screens. Also shown is the approximate spectral energy distribution of the image projected by the Baum projector with an electroluminescent (EL) panel as the source.

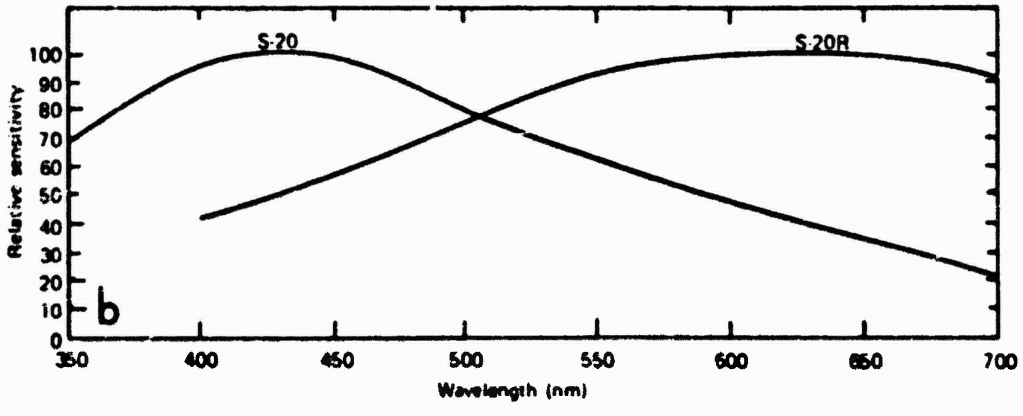

Spectral sensitivities of an Electronics Industries Association S-20 photocathode on lime glass and a representative Varo S-20R extended red photocathode on a fiber-optic faceplate.

Fig. 20. Spectral sensitivities and spectral energy distributions.

IIa-D emulsion also has a relatively good spectral sensitization match to the electroluminescent panel. Thus, for comparison with image intensifiers, we have taken photographs directly of the Baum target with an unaided IIa-D emulsion.

Results of the sensitivity measurements are given in Table 7. The table lists the voltage at which each tube was operated, the transfer method used (relay lens at $f/2$ or fiber-optic contact), and the exposure that produced a density above fog on the photograph of 0.6. Also given is the photographic speed gain, which is defined as the ratio of the two respective exposures producing a density of 0.6 above fog, one on an unaided IIa-D emulsion and one through an image tube. The exposure on the unaided IIa-D photograph was 5.1×10^{-2} erg/cm^2.

The last line of part (a) of Table 7 gives a "standardized" photographic speed gain for the electrostatic intensifiers, which provides a more uniform intercomparison of these intensifiers. The standardized value is the predicted photographic speed gain that would exist if (1) every intensifier were operated at 15 kV per stage and (2) all photographs were obtained by fiber-optic contact. Measurements have shown that the transfer efficiency of the relay lens (set at $f/2$) is 1.33% that of direct fiber-optic contact.

Table 8 gives the relative measured speeds of all the emulsions we have used with intensifiers. The results are given for both P-11 and P-20 phosphors. Because of its low sensitivity, Projector Slide emulsion would seldom be used in normal image tube photography. However, its relatively high resolving power, high contrast, high information storage capacity, and good reproducibility among emulsion batches make it extremely useful as a laboratory test emulsion.

Table 7. Photocathode Exposure Producing Density = 0.6 above Fog on IIa-O and IIa-D Emulsions

a. Electrostatically focused

Manufacturer	ITT	No. 1 Varo	No. 2 Varo	Varo	ITT	RCA	Varo
Model	F-4708	8605	8605	8605IX	F-4724	8606	8606
Phosphor	P-20	P-20	P-20	P-20	P-20	P-20	P-20
Voltage (kV)	14	15	12	15	30	45*	40**
Transfer	F-O contact	F-O contact	F-O contact	F-O contact	F-O contact	Relay lens $f/2$	Relay lens $f/2$
Exposure (erg/cm^2 X 10^5)	200	75	93	58	5.4	20	15
Photographic gain	25	67	55	87	940	250	330
Std. photographic gain	28	67	75	87	9100	19000	45000

b. Magnetically focused

Manufacturer Model	EEV P829D	EEV P829D	EEV P829D	ITT F-4089	RCA C33011	RCA C70021AEP2	RCA C70021AEP2
Phosphor	P-11	P-11	P-11	P-20	P-11	P-22B***	P-22B
Voltage (kV)	30	36	40	16	23	27	22
Transfer	Relay lens *f*/2	Relay lens *f*/2	Relay lens *f*/2	F-O contact	Relay lens *f*/2	Relay lens *f*/2	Relay lens *f*/2
Exposure ($erg/cm^2 \times 10^5$)	230	8.3	3.3	99	120	1.9	4.2
Photographic gain	22	610	1500	51	43	2600	1200

*Voltage division was assumed to be 15 kV per stage for calculation of standardized photographic speed gain.
**Voltage on the three stages was 12, 13, and 15 kV, respectively.
***Spectral emittance of P-22B phosphor is similar to that of P-11, therefore the image tube was photographed with IIa-O.

Table 8

Relative Speed of Photographic Emulsions To P-11 and P-20 Phosphors (Density = 0.6 Above Fog)

Emulsion	P-11	P-20
IIa-G	1.00	0.25
IIa-D	••	1.00
IIIa-J	0.7	0.41
Projector Slide (med)	0.2	0.002
Metallographic	0.3	0.15

It should be pointed out that photographic speed gain, used alone, is not a measure of the "information rate" gain of an image tube photograph. Speed gain as defined here is simply a practical way of comparing the speeds at which different intensifier systems produce a photographic density of 0.6, a value likely to be used in practice. The quality or information content of two image tube photographs exposed to this density can be judged only when the detective quantum efficiency of the two systems is known, as will be discussed later.

6. Uniformity of Response

The method used to assess uniformity of response is to uniformly irradiate the photocathode and then obtain high-contrast, fine-grained photographs of the output from which the uniformity can be measured. Uniform irradiance is provided by a distant point source, and interference filters with central wavelengths of 425 and 800 nm are used to define two spectral passbands. The emulsion used is Projector Slide.

Figure 21 shows records of the outputs from all the image intensifiers photographed in this manner. The transfer method (relay lens or fiber-optic contact) for each tube was previously given in Table 6. Five common nonuniformity phenomena are apparent in these photographs: (1) a radially symmetrical but nonflat "sensitivity profile" (response versus radius) especially apparent in the electrostatic tubes (a through g); (2) discrete, rather diffuse concentric rings in some of the electrostatic tubes (compare a and b); (3) enhanced or diminished response in localized, relatively large areas (c, e, g, and k); (4) a repetitive dark pattern, "fiber-optic bundle pattern," in some of the tubes using fiber-optic faceplates (a, f, and h); (5) an over-all "clumpiness" or small-scale deviation that occurs throughout the field of some tubes (see i), but that is often almost masked by fiber-bundle pattern (see b and h) in tubes having fiber-optic faceplates. In addition, a fixed "granularity" is often discernible on the photographs, but the reproductions in Fig. 21 do not clearly show this fine structure.

a. Sensitivity profile. Figure 22 shows the sensitivity profiles measured for four electrostatic tubes. The two most important causes of response falloff toward the field edge in the electrostatic tubes are, in order of importance: (1) geometrical distortion, the effect of which is shown by the curves labeled $1/M_A$ in Fig. 22 and (2) a decrease in transfer efficiency of the phosphor radiation as the field radius is increased. There are also wavelength dependences of the sensitivity profile due to the curved surface of the photocathode and the resultant variation in the angle of incidence of the input radiation.

The magnetic tubes tested generally show much flatter sensitivity profiles than do the electrostatic tubes (see Figs. 23a and b). Moreover, the measured profiles are generally within 10% agreement with the profiles predicted by geometrical considerations alone. (The deviation of the profiles in Fig. 23b from the $1/M_A$ curve is somewhat greater than 10% near the field edge owing to a relatively strong shading of the photocathode.)

b. Concentric rings in electrostatic tubes. When bright or dark rings are present, their location and structure are dependent on the angular distribution and the wavelength of the incident radiation. These rings have been found to be caused by the steep curvature of the input photocathode and appear to be produced by constructive and destructive interference phenomena in the thin film photocathode as well as by double pass effects. The response within a ring deviates from the over-all sensitivity profile generally by less than 10%.

c. Large-area variations in response. A relatively smooth gradient in the response from one edge of the field to another or localized, relatively large-area regions of enhanced or diminished sensitivity are fairly common with the intensifiers we tested. Localized deviations from the mean response are typically a few percent but occasionally are as much as 10% to 30%.

Nonuniformities are especially pronounced in the S-20 photocathodes when irradiated with 800-nm radiation. Compare, for example, the photographs shown in Figs. 21j and k

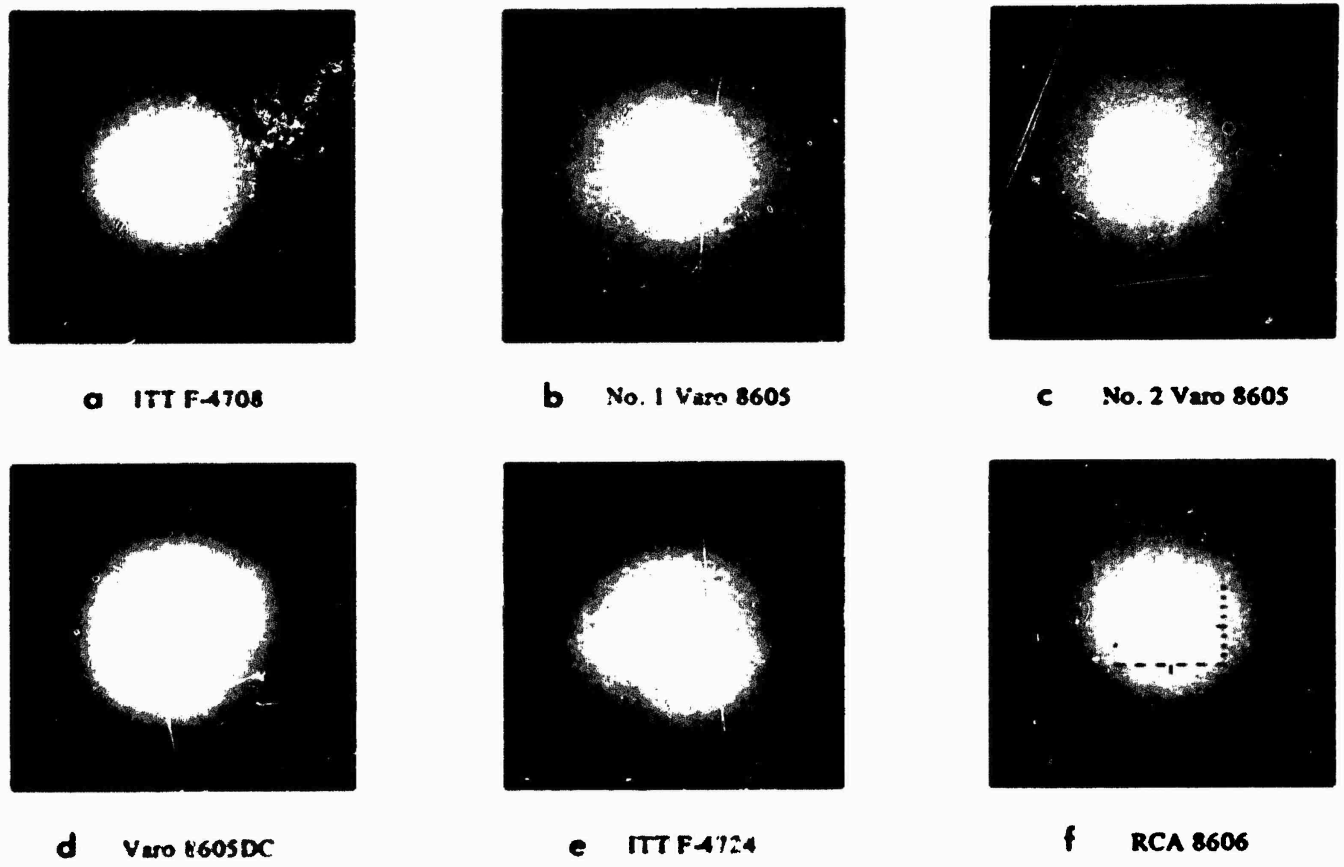

a ITT F-4708

b No. 1 Varo 8605

c No. 2 Varo 8605

d Varo 8605DC

e ITT F-4724

f RCA 8606

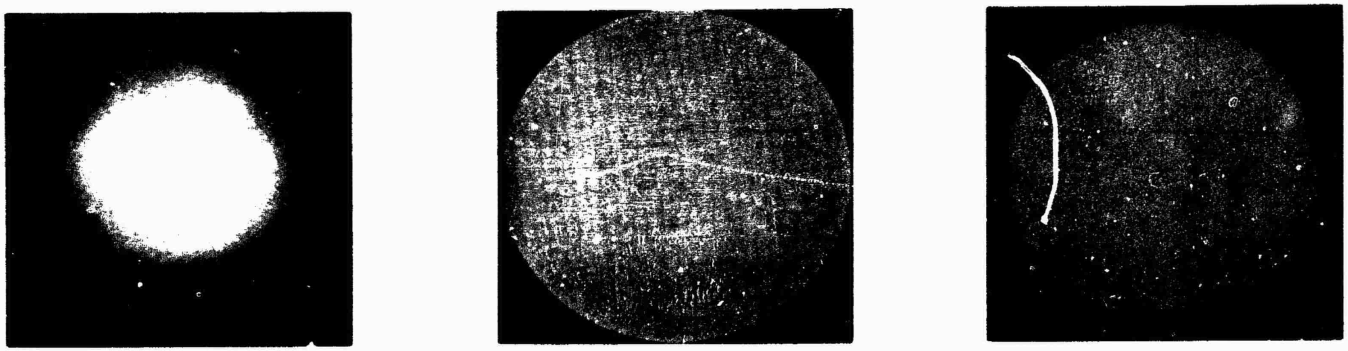

g Varo 8506 h ITT F-4089 i RCA C33011

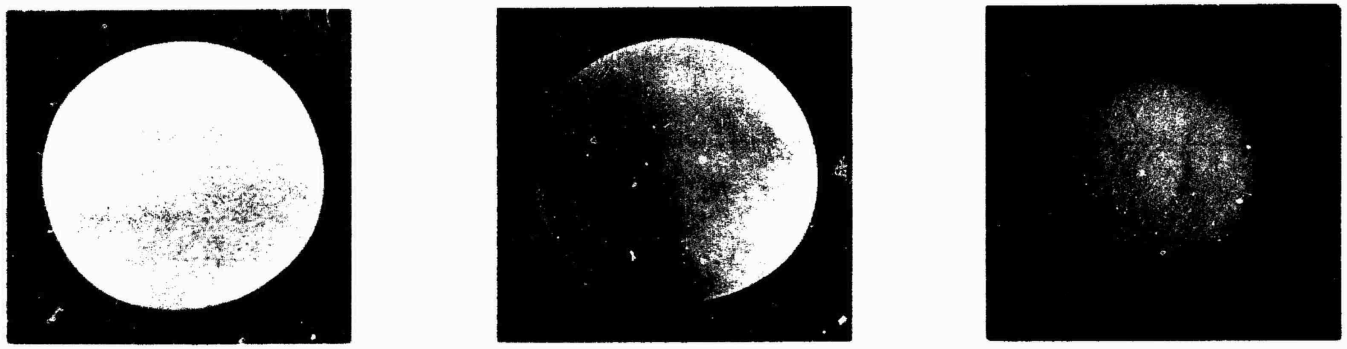

j RCA C70021AEP2 k RCA C70021AEP2 l EEV P829D

Fig. 21. Photographs of all intensifiers under conditions of uniform irradiation by a distant point source. The wavelength of radiation is 425 nm in all cases except for (k) where the wavelength is 800 nm. Projector Slide emulsion was used.

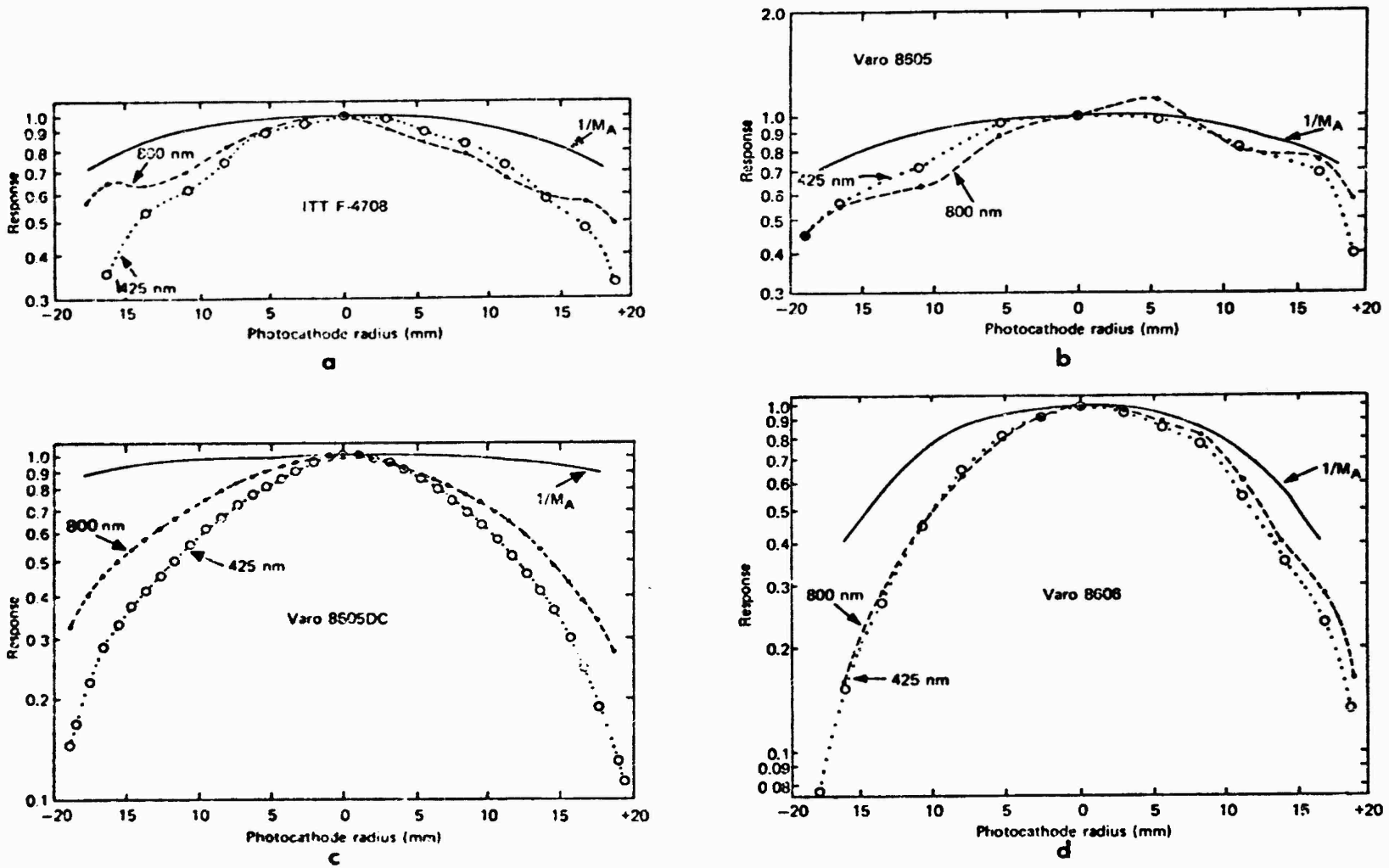

Fig. 22. Sensitivity profile at two wavelengths and the reciprocal of the elemental area magnification for four electrostatically focused tubes.

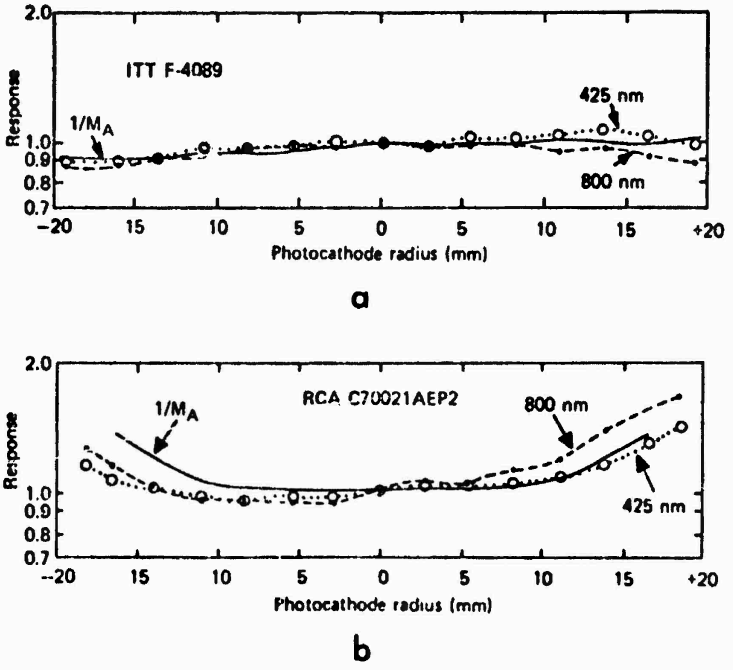

Fig. 23. Sensitivity profile at two wavelengths and the reciprocal of the elemental area magnification for two magnetically focused tubes.

obtained with 425-nm and 800-nm radiation, respectively, and also compare the sensitivity profiles shown in Fig. 23b.

d. Fiber-optic bundle pattern. The fiber-optic bundle pattern, or "chicken wire," seen in Fig. 21a is typical of several fiber-optic tubes we have seen although there is significant variation from tube to tube. In general, fiber-optic plates made up of hexagonal arrays (such as those in Figs. 21b, c, and g) are freer of bundle pattern than those with square arrays (Figs. 21a, d, e, f, and h). The tube whose response is shown in Fig. 21b is one of the best tubes we have tested with respect to freedom from fiber-optic bundle pattern.

Microdensitometer traces with a 10-μm by 250-μm slit of all the photographs in Fig. 21 are shown in Fig. 24. A trace is also shown of the unaided Projector Slide emulsion exposed to the same density as the image tube photographs. In these traces the bundle pattern in the fiber-optic tubes can be clearly identified as a cyclic modulation that produces a 5% to 10% deviation from the mean response in the worst cases.

e. Clumpiness and granularity of phosphor screens. Other fixed noise patterns that are occasionally discernible, especially if there is no fiber-bundle pattern to mask their detection, are clumpiness and granularity of the phosphor screens. An important result of this type of noise pattern, as well as of the fiber-bundle pattern, is reduced detection of threshold images such as faint images against a bright background. In principle, calibration procedures can be used to remove fixed noise pattern. In practice, however, such procedures are difficult to carry out, at least on photographic records.

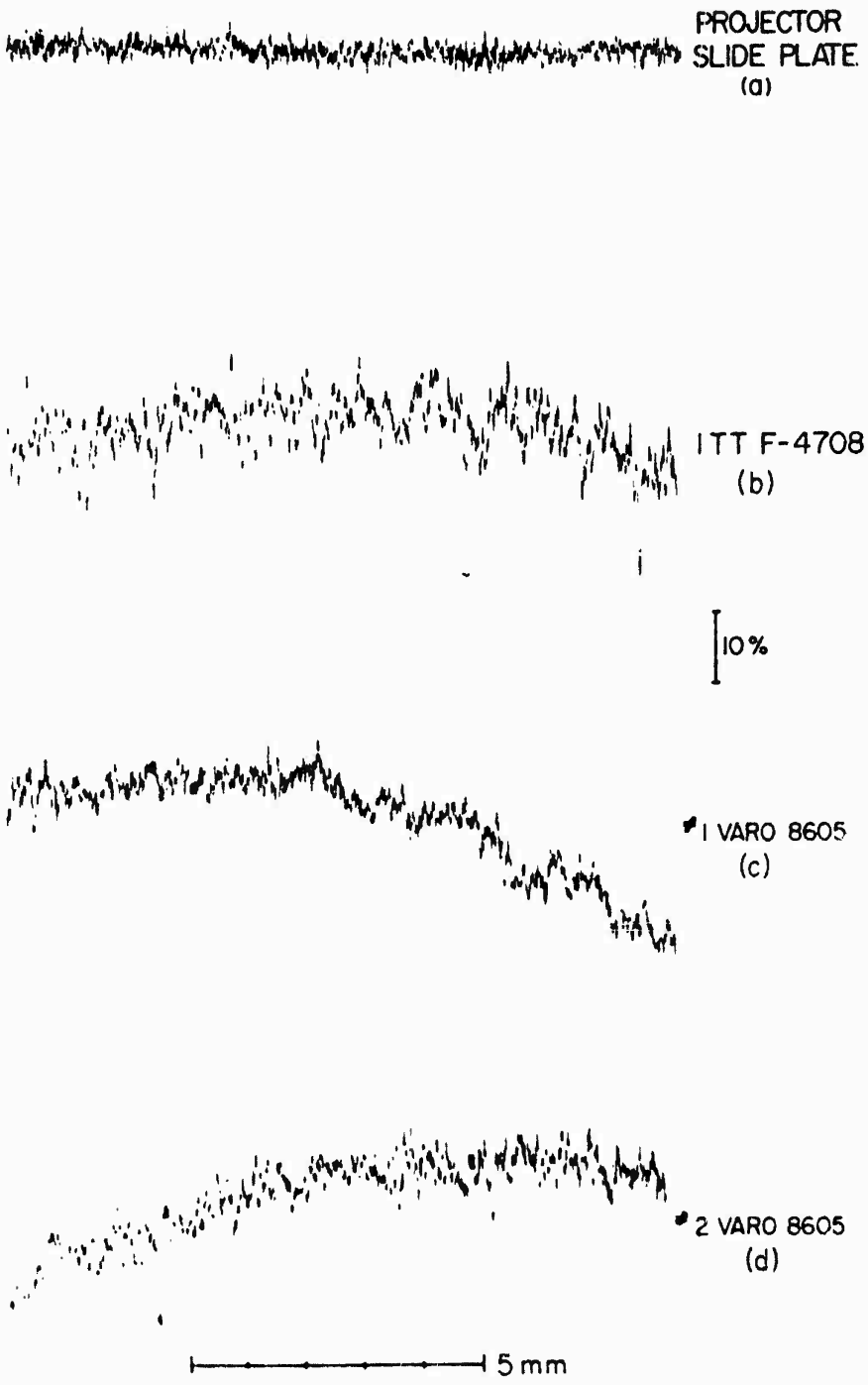

Fig. 24. Microdensitometer traces of image tube photographs shown in Fig. 21 made on a Joyce-Loebl microdensitometer with a 10-μm by 250-μm slit. Also given is a trace of an unaided Projector Slide emulsion exposed to the same density. The vertical bar indicates the amplitude of a 10% sensitivity variation. The horizontal bar indicates a 5-mm length on the image tube output screen.

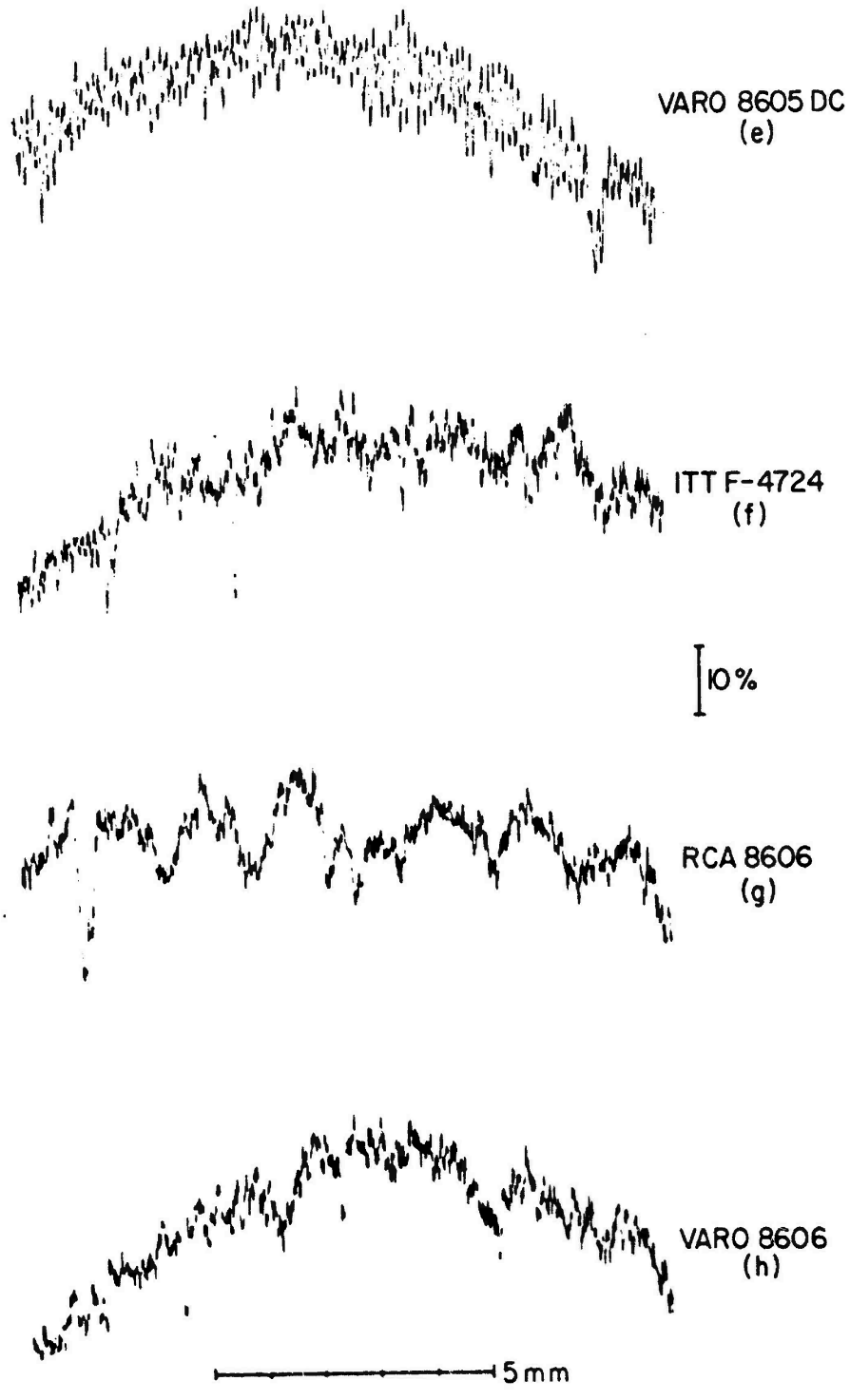

Fig. 24. Continued.

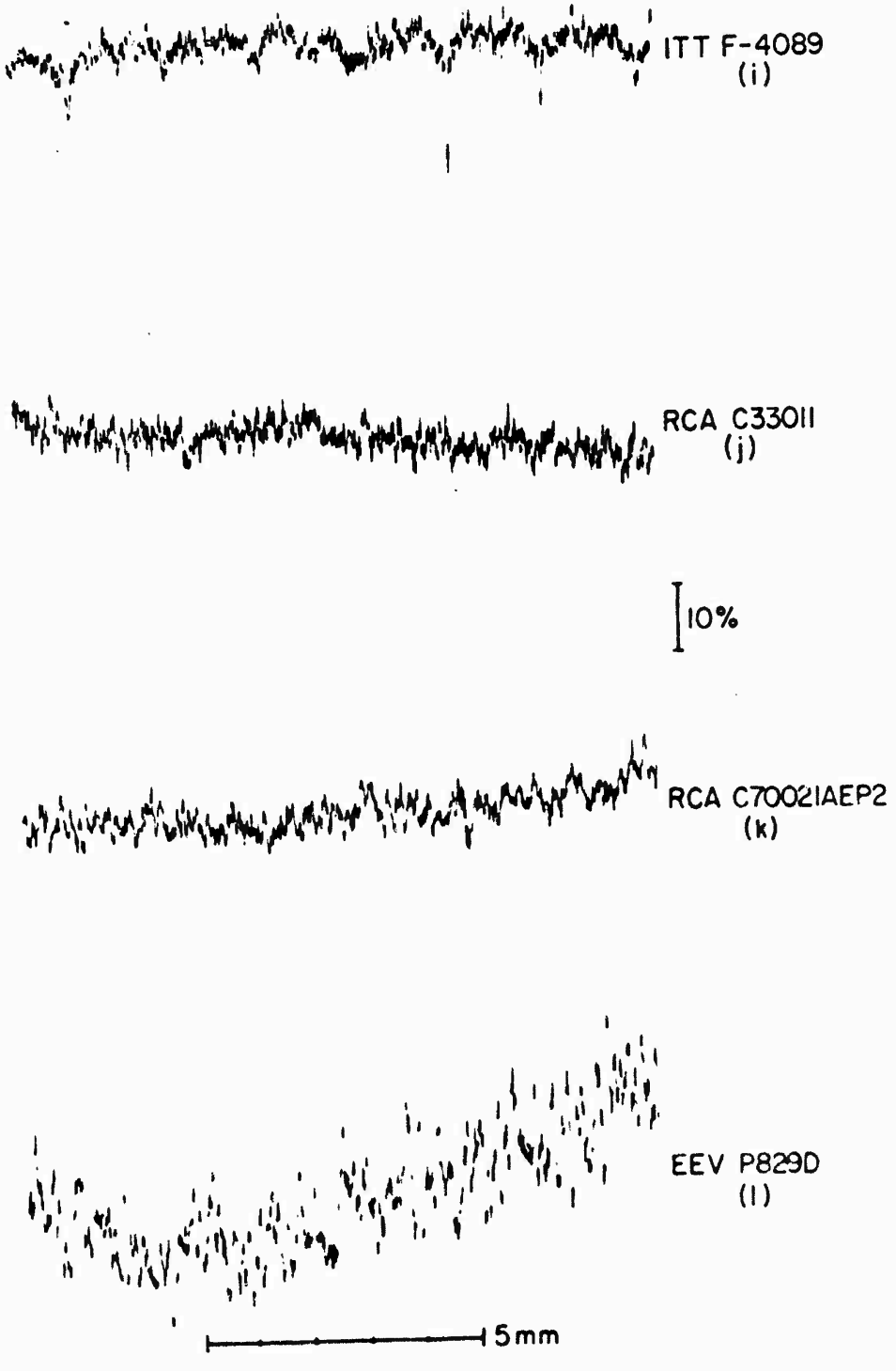

Fig. 24. Continued.

The manufacturers have been working to reduce this type of nonuniformity in image intensifier phosphors, and a comparison of Fig. 21j (which is of a recent three-stage intensifier) to Fig. 21i (which is of a much older two-stage intensifier) shows their efforts have been successful. A measure of the variation in sensitivity produced by clumpiness as well as the phosphor granularity may be obtained by studying the microdensitometer traces j and k of Fig. 24.

It is clear from studying the types of nonuniformities discussed in this section that, in applications where accurate radiometric measurements are to be made with an image intensifier, detailed calibration maps of the sensitivity, including its spectral dependence, must be obtained. The variations from uniform response are less important in the magnetically focused tubes although either electrostatically focused or magnetically focused tubes should lend themselves to calibration.

7. Light-Induced Background

Light-induced background is important in the over-all performance of image intensifiers. The additional noise produced by such background often significantly reduces the signal-to-noise ratio of weak images and, in applications where accurate radiometry is desired, corrections for the background must be included.

Figure 25 illustrates the general character of the light-induced background in a three-stage electrostatic intensifier. Figure 26 shows the results of measurements of the background of three types of intensifiers: (a) a single-stage electrostatic (No. 2 Varo 8605); (b) a three-stage electrostatic (Varo 8606); and (c) a single-stage magnetic (ITT F-4089). The measurements were taken along the diameter that is located about 1 mm from the irradiated border. Results are given for incident radiation of two different wavelengths. The background is expressed as an equivalent incident light that would produce the same output signal as the measured background signal. The hypothetical light is expressed as a percentage of the true incident radiation.

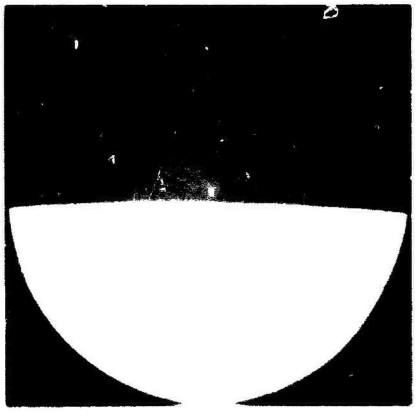

Fig. 25. Light-induced background for a three-stage electrostatically focused intensifier. Slightly less than half of the field is uniformly irradiated by a distant point source. The rest of the field is masked off, and the output signal from this portion is due to light-induced background.

a Single-stage electrostatically focused intensifier.

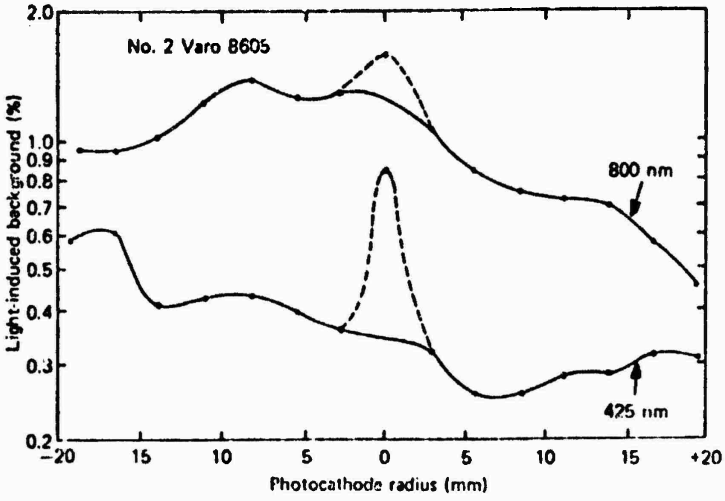

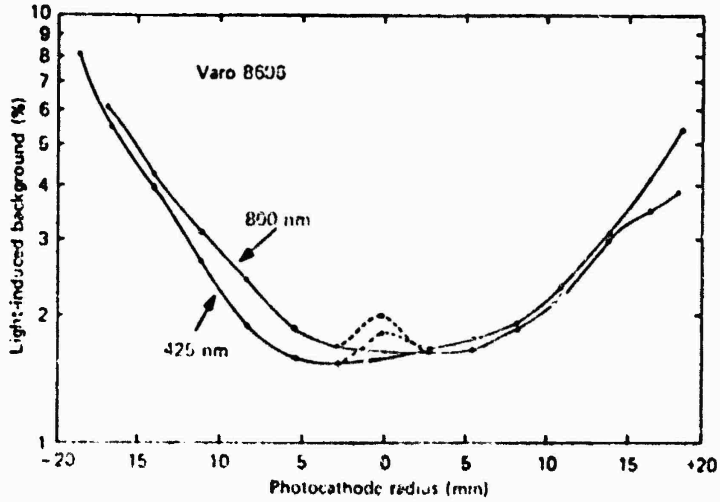

b Three-stage electrostatically focused intensifier.

c Single-stage magnetically focused intensifier.

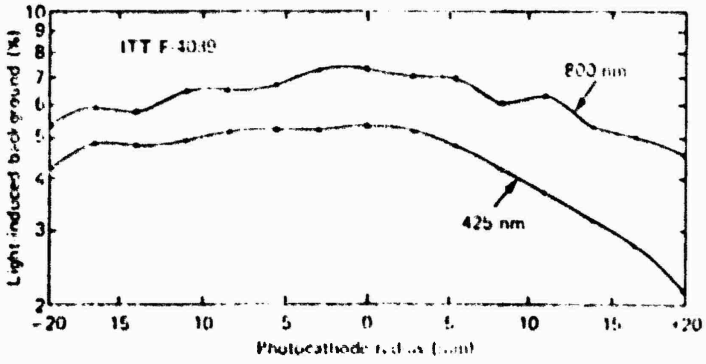

Fig. 26. Light-induced background at two wavelengths, half-field irradiation. The detailed structure of the central spikes in (a) and (b) (dashed lines) is only approximate.

Table 9 lists the light-induced backgrounds that occur near the field centers of the tubes when the tube photocathodes are uniformly irradiated over their entire area. The light-induced background is generally diffuse, and only in the case of the electrostatic tubes is there a sharp spike in the center. The values in the table refer to the diffuse background only and not to the local spike. The dependence of the background on field position is a general characteristic for all tubes, and the detailed structure is different from one class of tube to another, as illustrated in Fig. 26. This dependence makes it difficult to account properly for light-induced background in certain radiometric measurements.

Table 9. Light-Induced Background from Uniformly Irradiated Photocathode

a. Electrostatically focused

Manufacturer	ITT	No. 1 Varo	No. 2 Varo	Varo	ITT	RCA	Varo
Model	F-4708	8605	8605	8605DC	F-4724	8606	8606
Bkgd near center (%)							
425 nm	0.97	1.7	0.7	2.5	4.1	7*	3.0
800 nm	2.3	4.9	2.4	4.3	7.0	7*	3.2

b. Magnetically focused

Manufacturer	EEV	ITT	RCA	RCA
Model	P829D	F-4089	C33011	C70021AEP2
Bkgd near center (%)				
425 nm	**	13	22	37
800 nm	**	18	36	41

*Approximate value only.
**Data are incomplete. However, background is substantially higher than in other tubes tested.

Electrostatic tubes, for the same number of stages, have only about one-fifth as much light-induced background as the magnetic tubes. This is due largely to the focus anode in the electrostatic tubes, which acts as a shield against scattered light, electrons, and ions. Also, because the electrostatic tubes use fiber-optic input and output faceplates, the internal reflections that normally occur in standard glass faceplates are absent.

The principal causes of light-induced background have been identified by studying the background produced by a single small-area incident image. Figures 27a and b illustrate the types of spurious signals that occur in two different intensifiers when studied in this manner. Two dominant sources of light-induced background have been found to be optical feedback from the output phosphor and original input light that is transmitted by the photocathode and is subsequently scattered back to it. Other sources that have been identified are scattered ions and electrons and, in tubes utilizing standard glass faceplates, internally reflected light within the faceplates.

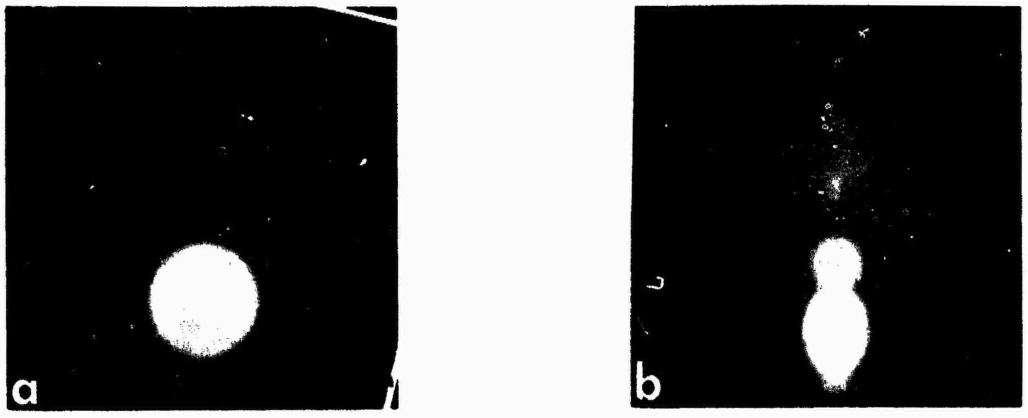

Fig. 27. Light-induced background from a small-area image for an RCA C33011, two-stage magnetically focused tube (a) and for a Varo 8606, three-stage electrostatically focused tube (b). An overexposed primary image is located toward the bottom of the field in each photo. In photo (a) the intensity of the background near field center is approximately 10^{-3} that of the primary image and in photo (b) it is approximately 10^{-4} that of the primary image.

8. Dark Emission

The dark emission from photodetectors is exceedingly important in setting the lower limit to the radiation levels that may be detected. In intensifiers, the principal cause of dark emission is thermal emission of electrons from the photocathode although other causes such as field emission within the tube may sometimes occur. In addition, most tubes with multi-alkalai photocathodes have a certain ion emission background believed to be caused by the ionization of heavy atoms by electron bombardment. Ion emission can be especially troublesome in photographs taken with high-gain intensifiers because of the particularly strong noise that is produced by the ion scintillations.

Records have been made of the dark emission of the intensifiers by taking long-exposure photographs of the phosphor outputs while the intensifiers were in total darkness. Measurements of the dark emission photographs are presented in Table 10. Given in the respective lines are (1) tube model, (2) photocathode type, (3) applied high voltage, (4) ambient room temperature (temperature of water-cooled solenoid cavity in the case of EEV P829D and RCA C70021AEP2), (5) photographic emulsion, (6) phosphor-to-emulsion transfer method, (7) exposure time, (8) density above fog produced by dark emission near the field center of the intensifer (measured with Joyce-Loebl microdensitometer), (9) the calculated value of the equivalent background input (EBI), and (10) the ion dark emission based on counts of the ion scintillations recorded on the photographs. The EBI is the value of incident radiant flux (with a spectral distribution of the electroluminescent panel shown in Fig. 21a) required by the photocathode of the intensifier to produce an increase in the phosphor screen radiance equal to the radiance produced by the dark emission.

The tubes that have especially low dark emission for their respective type of photocathode are the No. 2 Varo 8605, the Varo 8606, the EEV P829D, the RCA C33011, and the RCA C70021AEP2.

Table 10. Dark Emission Measurements

a. Electrostatically focused

Manufacturer Model	ITT F-4708	No. 2* Varo 8605	Varo 8605DC	ITT F-4724	RCA 8606	Varo 8606
Photocathode	S-20 ext. red	S-20R	S-20R	S-20 ext. red	S-20 ERMA	S-20R
Voltage (kV)	15	12	15	42	45	40**
Temp (°C)	20	19	18	22	22	19
Emulsion	IIa-D	IIa-O	IIa-O	IIa-D	IIa-O	IIa-D
Transfer	F-O contact	F-O contact	F-O contact	F-O contact	Relay lens *f*/1.4	Relay lens *f*/2
Exp. time	1 h	1 h	1 h	approx 15 sec	1½ h	1 h
Density above fog	1.43	0.07	1.04	1.95	0.51	0.52
EBI (W/cm^2)	1.2×10^{-13}	4.6×10^{-15}	1.3×10^{-13}	3.0×10^{-13}	1.9×10^{-13}	3.7×10^{-15}
ions/cm^2/sec	1	indiscernible	indiscernible	70	0.1	0.07

b. Magnetically focused

Manufacturer Model	EEV P829D	EEV P829D	EEV P829D	ITT F-4089	RCA C33011	RCA C70021A1 P2
Photocathode	S-20	S-20	S-20	S-25	S-20	S-20
Voltage (kV)	30	36	40	16	23	22
Temp (°C)	8	16	8	22	20	20
Emulsion	IIa-O	IIa-O	IIa-O	IIa-D	IIa-O	IIa-O
Transfer	Relay lens *f*/1	Relay lens *f*/1	Relay lens *f*/1	F-O contact	Relay lens *f*/1.2	Relay lens *f* 2
Exp. time	1 h	1 h	1 h	1 h	4 h	1 h
Density above fog	0.00	0.03	0.12	0.28	0.00	0.04
EBI (W/cm^2)	less than 2×10^{-13}	approx 6.9×10^{-17}	6.3×10^{-17}	1.3×10^{-13}	less than 4×10^{-16}	approx 1.4×10^{-16}
ions/cm^2/sec	undeter-minable	undeter-minable	undeter-minable	0.5	less than 10^{-5}	0.3

*No. 1 Varo 8605 was not measured.
**Voltage on the three stages was 12, 13, and 15 kV, respectively

The ion dark emission values measured from the photographs are generally uncertain by about 50% because the images of the ion scintillations were usually just barely distinguishable from emulsion granularity, quantum noise of the dark-emission electrons, or fixed noise patterns of the intensifier. The importance of ion emission in high-gain intensifiers is clearly demonstrated in a 1-h photograph taken with the RCA C70021AEP2 tube, shown in Fig. 28. It is apparent on the photograph that the ion background significantly increases the noise in the recorded image and that the accuracy of microphotometer traces would be seriously impaired as a result of the ions.

Fig. 28. RCA C70021AEP2 tube with 1-h exposure. The Baum image is the result of phosphor persistence in the first dynode. The ion dark emission is seen to strongly affect the noise of the photographic image. The presence of electron dark emission is barely discernible in the reproduction.

It should be pointed out that the significance of the ion background would be greatly reduced in an imaging detector where an electronic recording device such as a television camera is used to discriminate ion scintillations from electron scintillations. Such a system would have a clear advantage over one using a photographic emulsion for which discrimination is exceedingly difficult.

9. Detective Quantum Efficiency

We feel that detective quantum efficiency (DQE) is one of the most significant, fundamental performance characteristics of an image detector. It describes how well in practice, not in theory, the detector utilizes the information inherent in a photon image. (See Jones (1958, 1959), Marchant and Millikan (1965), and Zweig, Higgins, and MacAdam (1958) for detailed discussions of DQE.)

The DQE of an intensifier-plus-photographic-emulsion system is calculated by measuring the output signal-to-noise ratio, $(S/N)_{out}$, of the photograph with a microdensitometer and then comparing it to the input signal-to-noise ratio, $(S/N)_{in}$, which is determined by photon statistics of the input image. DQE is defined simply as the ratio

$$DQE = [(S/N)^2_{out}]/[(S/N)^2_{in}].$$

It is interesting to note that, if an image intensifier system added no spatial or temporal noise to the stream of photoelectrons emitted from its initial photocathode, and if each photoelectron were detected, then its DQE would be numerically equal to the quantum efficiency of the photocathode.

Perhaps the most useful way of describing the performance of a detector is to plot its DQE as a function of exposure to the incident radiation. This should be done for radiation of a specified spectral distribution (preferably monochromatic) and for images large in comparison to the resolution limit of the detector. An intercomparison of detectors can then be made by studying their DQE versus exposure curves. For most low-light-level applications (where an intensifier system is most likely to be required) the preferred detector is the one having the highest DQE value at the lowest exposure level. The output signal-to-noise ratio that is obtainable with a certain detector may be calculated from the defining equation of DQE, given above, and the DQE versus exposure curve. To compare detectors having different resolving powers, it is often necessary to select a different input optical system for each detector so that the scene being imaged is equally well resolved by each detector.

A full description of a DQE sensitometer developed during this study and the methods of measuring the DQE of image tube photographs have recently been presented by Smith (1972). For details the reader should refer to Smith's publication. However, it is useful to summarize a portion of Smith's work here.

Figures 29 and 30 (Smith, 1972) show the general dependence of DQE on exposure and photographic density, respectively. Data are shown for two image tubes in these figures. One tube, the EEV P829D, is the same one discussed throughout this paper. The other, an RCA C33011, is a different sample than the C33011 discussed in previous sections. Its only significant differences from the tube previously discussed are that the light gain is two times higher and the phosphor clumpiness is substantially reduced.

It is immediately apparent in Fig. 29 that the DQE of an image intensifier-plus-photographic-emulsion system is significantly higher than that of an unaided photograph. For example, a photograph using the RCA C33011 tube and IIa-O emulsion has about 20 times higher DQE than an unaided IIa-O. The DQE is not as high for the EEV P829D tube, but it is still significantly higher than that of an unaided emulsion. A principal reason for the low DQE of the EEV intensifier is its unusually wide range of scintillation sizes. (Basically, only the brightest scintillations are photographically recorded. Therefore, even though there may be a large number of total scintillations (of all sizes), the final output signal-to-noise ratio is determined principally by the relatively few very bright scintillations.)

Also immediately apparent in Fig. 29 is that the exposure at which an intensifier system achieves optimum DQE is much lower than that of an unaided photograph. The reduction in exposure is simply the inverse of the photographic speed gain given earlier.

It is interesting to note that, at least for the RCA C33011 intensifier, the shape of the DQE versus exposure relationship is quite similar to that of the unaided emulsion. Smith

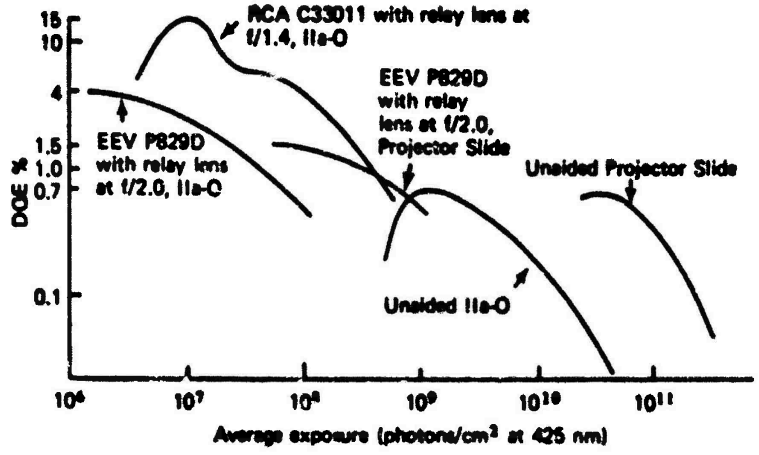

Fig. 29. DQE vs average exposure using the ΔD method. (See Smith (1972) for a discussion of the ΔD method.)

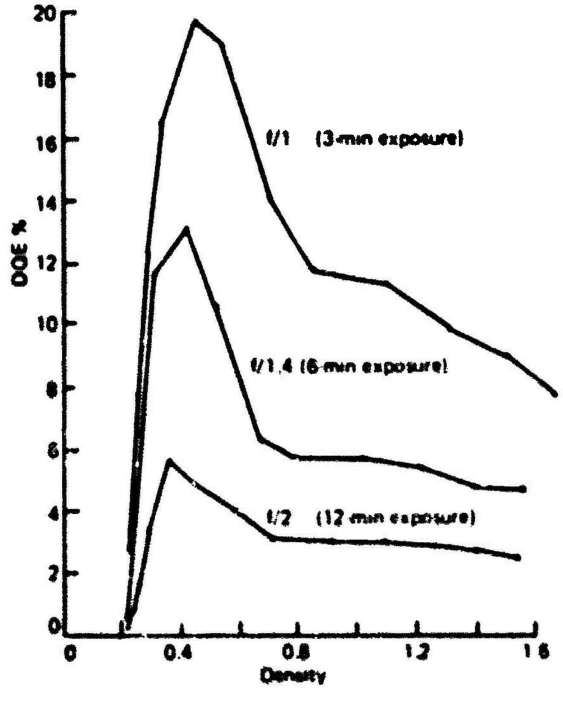

Fig. 30. DQE vs density using the gradient method. RCA C33011 tube with different relay lens openings; IIa-O emulsion; 425-nm radiation. (See Smith (1972) for a discussion of the gradient method.)

finds that for "multiple-photon event" detectors such as the RCA C33011 (where more than one photoelectron scintillation is required to make a detectable photographic density) the final record has a peaked DQE versus exposure curve, with the DQE equal to zero near zero exposure and with a maximum DQE occurring at a density above fog of approximately 0.2. This density for maximum DQE appears to be nearly invariant for all multiple photon event detectors, including the unaided emulsion itself.

As the photographic speed gain of an intensifier is increased beyond unity, the principal effect is to increase the DQE of the photographic emulsion. (At the same time, of course, the exposure at which optimum density occurs is reduced in inverse proportion to the gain.) This effect is clearly illustrated in Fig. 30, where the gain of the intensifier has been varied by changing the relay lens relative aperture. Smith's measurements of the photographic speed gains corresponding to the three curves in this figure were 60, 120, and 240 for $f/2.0$, $f/1.4$, and $f/1.0$, respectively.

As the photographic speed gain is increased even farther, a point is reached where each individual photoelectron scintillation produces a discrete clump of photographic grains. Such a detector system then becomes a "single-photon-event" detector such as the EEV P829D tube, and the behavior of the DQE versus exposure relationship is altered: Maximum DQE occurs at exposures very near zero. As with multiple-photon-event detectors, DQE falls off with increasing exposure although the slope is very mild at first. The absence of a sharp falloff of DQE with decreasing exposure at the very low exposure end (or at low densities) is explained by the fact that each photoelectron is clearly and independently recorded by the emulsion. This is quite different from the case of a lower gain tube or an unaided emulsion where two or more photoelectrons (or photons) are required within a certain time interval to render a photographic grain developable.

The eventual falloff of DQE with increasing exposure in all the curves of Fig. 29 may be understood as a "saturation" of the photographic emulsion. That is, after a certain amount of exposure, a significant fraction of the total available photographic grains are rendered developable and are no longer active in recording new information; therefore, the probability of detecting a new photoevent is substantially reduced.

Smith's data for the RCA C33011 in Fig. 30 indicate that in order for the peak DQE of an intensifier plus high speed emulsion (IIa-O) to be as high as possible (i.e., near the quantum efficiency of the photocathode), the photographic speed gain must be on the order of 300. The speed gain is approximately this value for the C33011 photographed with the relay lens at $f/1$. However, based on the subjective appearance of photographs taken of the RCA C70021AEP2, and not on any detailed DQE measurements, it appears that the speed gain of multistage cascade tubes must be approximately 10 times this high, or 3000, for the system to behave as a single-photon-event detector. These values, 300 and 3000, should apply approximately to all the types of tubes tested in the previous sections with the exception of the EEV, which is a transmission secondary emission design. The EEV tube has already been pointed out to be a single-photon-event detector at a photographic speed gain of about 600, but at this gain only the brightest scintillations are clearly recorded and many faint ones are not. The resultant degradation of DQE due to the wide scintillation size distribution of this transmission secondary emission tube has already been discussed.

There are a number of adverse characteristics in image intensifiers that can occur and that will reduce the DQE of the system. Particularly important among these are light-induced background, fixed noise structure (e.g., phosphor granularity and clumpiness, fiber-optic bundle pattern, etc.), and dark emission. Obviously, the less a particular intensifier exhibits one of these shortcomings then the less chance there is that that particular shortcoming will

degrade its DQE. Unfortunately, the practical tradeoffs among different types of intensifiers showing different amounts of these shortcomings are not presently well known. Clearly, the most satisfactory way of intercomparing various systems is to measure their DQE's in a manner similar to that done by Smith for the RCA C33011 and EEV P829D intensifiers. Such information, plus the information already given for these tubes in the previous sections, should allow an investigator to select the tube best suited to his particular requirement.

One fairly common mistake made by image tube users is to conclude that because an intensifier photograph does not have sufficient "quality" for the job at hand, a standard photographic emulsion must be used even though the standard emulsion will require a much higher exposure and has a much lower DQE. The lack of quality that is of concern to the investigator is usually due to either insufficient resolution or insufficient signal-to-noise ratio. Often times, either or both problems may be corrected by simply selecting an optical system (used to form the image on the detector) that enlarges the image. A linear enlargement of the image by a factor m increases the projected area of a given element in the original scene by m^2. The total number of photoevents from that element that can be stored by the detector without saturation is correspondingly increased by m^2. Hence, the signal-to-noise ratio is improved by a factor equal to the square root of m^2, or m. The spatial resolution in the scene, of course, will also be increased by m. Thus, an intensifier photograph may be obtained that has the required signal-to-noise ratio and resolution, and it will be obtained with the high efficiency (DQE) of the image intensifier system.

10. Relay Lens Tests

An evaluation of three relay lenses was carried out very early in our intensifier tests in order to select the optimum lens for transferring the light from the intensifiers to a photographic emulsion. The lenses were an 86-mm $f/1.2$ Elgeet Navitar, an 85-mm $f/1$ Nikon Repro-Nikkor, and an $f/1.9$ Perkin-Elmer cathode ray tube lens. All three lenses were tested under conditions of 1:1 magnification.

Figure 31 shows the results of measuring the light transfer efficiency as a function of field radius for the three lenses. The Nikon lens at full aperture ($f/1$) is clearly the most efficient relay lens, although there is significant vignetting of off-axis light at this aperture setting.

Figure 32 shows the limiting resolution of photographs of the RCA C33011 intensifier obtained with each lens. Various aperture settings were used except for the Perkin-Elmer lens, which has a single, fixed aperture. These and other resolution tests plus the light transfer efficiency measurements make it clear that the Perkin-Elmer lens is substantially poorer than the other two lenses for a given transfer efficiency.

A result that appears contradictory at first is that photographs taken with Metallographic emulsion (Fig. 32a) show the Nikon lens to have superior resolution to the Elgeet lens for the same transfer efficiency whereas photographs taken with IIa-O emulsion (Fig. 32b) show the two lenses to be similar. The reason for this is the difference in spectral sensitivity between the two emulsions and the difference in chromatic correction between the two lenses. The Elgeet lens is designed for use with blue radiation only, whereas the Nikon lens is designed for a much broader spectral range. Thus, the two lenses perform similarly when IIa-O emulsion, sensitive to blue radiation only, is used. However, when Metallographic emulsion is used, with its more extended green response, the poorer color-corrected Elgeet lens suffers in comparison to the Nikon lens. This is true even though the source being

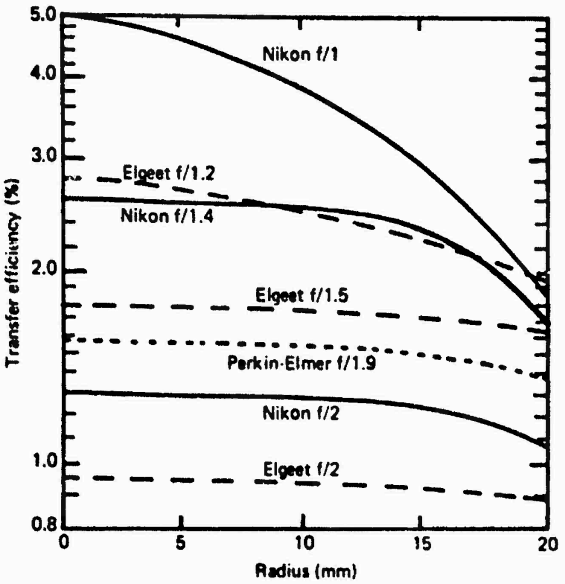

Fig. 31. The light transfer efficiency is plotted as a function of field radius for three relay lenses. The transfer efficiency is the percentage of light emitted from a phosphor screen that is transferred to the image plane by the lens.

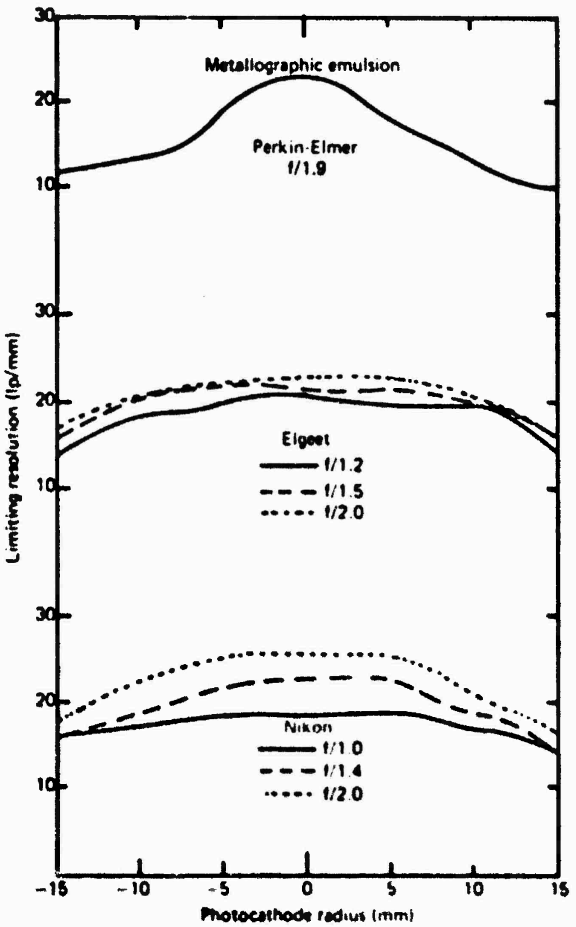

Fig. 32. Limiting resolution, in line pairs per millimeter, on photographs of the RCA C33011 image intensifier is shown as a function of photocathode radius. Metallographic emulsion was used for Fig. 32a, and IIa-O emulsion was used for Fig. 32b (next page). Interpolation of the measured curves shows that the Nikon lens provides the best resolution for a specified light transfer efficiency.

a

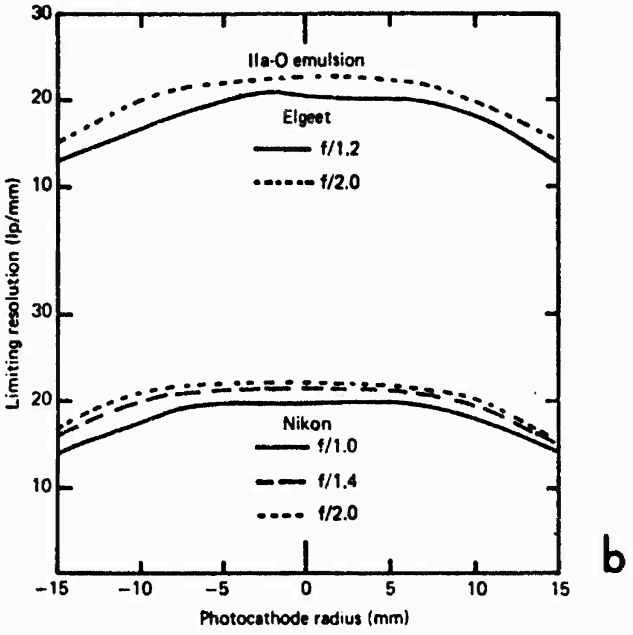

Fig. 32. Continued.

photographed in this case is a P-11 phosphor screen, which emits mostly blue radiation. When a green phosphor such as the P-20 type is being imaged, the Nikon lens is very much superior to the Elgeet.

When the Elgeet and Nikon lenses are used at their full apertures both lenses exhibit a large amount of spherical aberration. The result is a substantially reduced modulation transfer function even at spatial frequencies of a few line pairs per millimeter, and the photographic images appear very washed out. By the time the iris diaphragms are stopped down to $f/2$, the obvious effects of this aberration are eliminated.

We have concluded from the above and similar tests that the relay lens that gives the best over-all performance based on light transfer efficiency, vignetting characteristics, and resolution is the Nikon lens set at a relative aperture of $f/2$.

TASK II. WAVEFRONT–DETERMINATION–CORRECTION METHOD OF IMAGE RESTORATION

The objective of this task was to study the feasibility of using a modified Hartmann test as an aid in restoring atmospherically degraded images. With this method, the Hartmann test is used to determine the atmospherically produced wavefront perturbations at the exit pupil of the system, from which the transfer function of the system can then be determined. Once the transfer function is known, the degraded image is restored by standard inverse filtering techniques.

The assumptions upon which this method of image restoration are based are

(1) The imaging system is spatially invariant, i.e., the object is entirely contained within a single isoplanatic region.
(2) The object illumination is incoherent.
(3) The exit pupil of the system can be subdivided into small subapertures such that the primary aberrations present within each subaperture are simply wavefront tilt and piston error.
(4) The exposure time is short compared with the characteristic fluctuation time of the atmosphere, and no motion blur is present.

These assumptions appear to be reasonable for many situations in which images are to be obtained through the atmosphere, particularly those for which an earth-based instrument is used to image satellites.

A. GENERAL DISCUSSION OF TURBULENCE EFFECTS

The initial perturbation to a wavefield propagating through a turbulent atmosphere is a distortion of the cophasal surfaces, or wavefronts. As the wavefield continues to propagate, its modulus will also be changed by the effects of diffraction (even if the region is free of turbulence). In the general case where the wavefield travels a large distance through a turbulent atmosphere, the final distortion may be very severe owing to the combination of turbulence and diffraction effects.

For the case of a large earth-based telescope used to observe small objects at large distances, it is not unreasonable to assume that the turbulence occurs sufficiently close to the telescope so that

(1) The wavefront distortion is primarily phase distortion
(2) Light from all object points passes through the same region of turbulence. Hence the optical system is shift invariant
(3) Extended objects are illuminated incoherently, so the optical system is linear in irradiance.

Under these conditions it is possible to express an atmospherically blurred image as the convolution of the desired image with an atmospheric point spread function. If to the above three assumptions we add the requirement that this point spread function remain constant during the exposure time, it is theoretically possible (ignoring, for the moment, the presence of noise) to recover the desired image from the blurred image.

B. THEORY

We denote the object irradiance by $o(x,y)$, the image irradiance by $i(x,y)$, and the point-spread function of the imaging system (including the atmosphere) by $h(x,y)$. Thus, under the isoplanatic assumption, we may write the image irradiance as

$$i(x,y) = o(x,y)**h(x,y), \tag{1}$$

where the double asterisk denotes the two-dimensional convolution operation. Then, from the convolution theorem of the Fourier transform, the spatial frequency spectrum of the image is given by

$$I(\xi,\eta) = O(\xi,\eta)H(\xi,\eta) \tag{2}$$

where $I(\xi,\eta)$ is the Fourier transform, etc., and ξ and η are the spatial frequency variables corresponding to the x and y coordinates, respectively. The function $H(\xi,\eta)$ is the optical transfer function (OTF) of the entire imaging system and is affected both by atmospheric perturbations and telescope aberrations. It alters the magnitude and phase of the various Fourier components of the object, and thereby causes the image to be degraded. In the absence of atmospheric perturbations, $H(\xi,\eta)$ is simply the OTF of the telescope itself.

By making appropriate measurements, as outlined below, an estimate is obtained for the atmospherically degraded transfer function, and we denote this estimate by $\hat{H}(\xi,\eta)$. Then a restored image spectrum $\hat{I}(\xi,\eta)$ is calculated by

$$\hat{I}(\xi,\eta) = \frac{I(\xi,\eta)}{\hat{H}(\xi,\eta)} = \frac{O(\xi,\eta)H(\xi,\eta)}{\hat{H}(\xi,\eta)} \quad , \tag{3}$$

and the restored image itself is determined by an inverse Fourier transformation, i.e.,

$$\hat{i}(x,y) = F^{-1}[\hat{I}(\xi,\eta)] \; . \tag{4}$$

It should be clear that if our estimate $\hat{H}(\xi,\eta)$ is a good one, the restored image will bear a good resemblance to the object. On the other hand, if our estimate is a poor one, the restored image will also be poor.

We point out that the product $O(\xi,\eta)H(\xi,\eta)$ will become zero beyond certain so-called cutoff frequencies, ξ_c and η_c, and thus we cannot hope to extend the spectrum of the restored image beyond these frequencies nor can we restore the image spectrum at lower frequencies where the product $O(\xi,\eta)H(\xi,\eta)$ has a zero or near-zero value. However, we can expect to correct for some of the major atmospheric perturbations and telescope aberrations within the passband of the OTF.

C. DETERMINATION OF $\hat{H}(\xi,\eta)$

In the past, estimates of the system OTF have been made by recording the point spread function and then calculating the Fourier transform of the point spread function. However,

when the point spread function varies with time, as it will when atmospheric turbulence is a factor, the recording of the point spread function and the aberrated image must be made simultaneously. This obviously poses problems because often it is not possible to locate a point source in the vicinity of the object in a dynamic situation.

Attempts have also been made to determine the point spread function from the edge response of the system, but such attempts have met with little success for various reasons.

The method we have been working on does not require a knowledge of the point spread function, nor does it rely on the recording of the system edge response. It is determined by using the optical system shown schematically in Fig. 33. A portion of the light entering the telescope is caused to form an image in the usual fashion while the remainder of the light is used to determine the wavefront aberrations. The light is divided into these two portions by a beamsplitter, as shown in the figure, with the reflected portion forming the aberrated image.

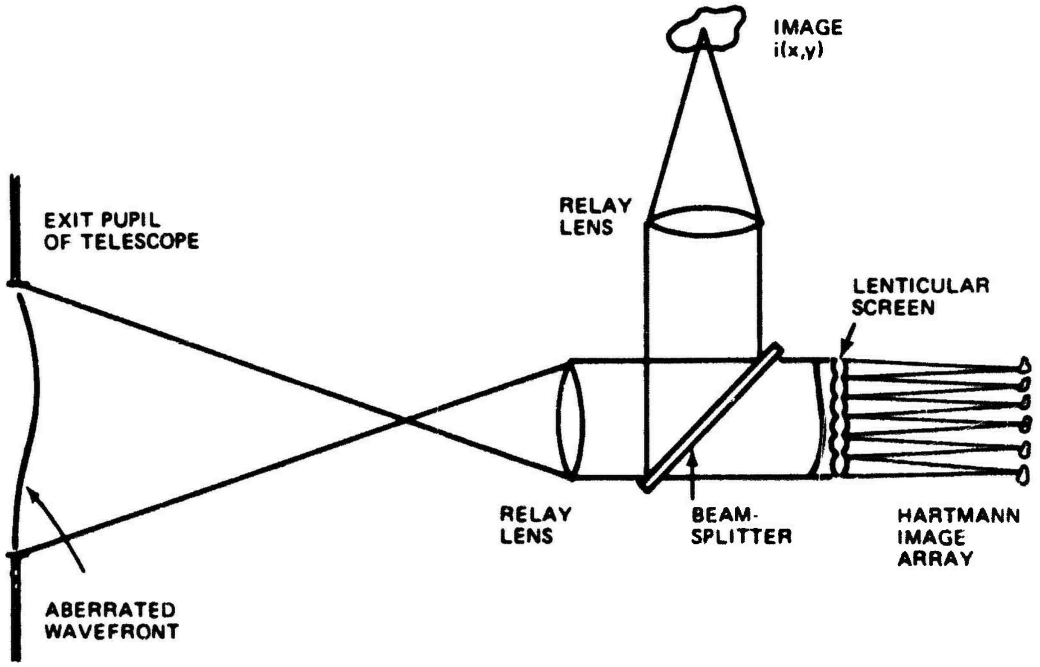

Fig. 33. Optical system used to estimate the OTF.

We now concentrate on the light transmitted by the beamsplitter. The relay lens casts an image of the telescope exit pupil onto a lenticular screen, i.e., a two-dimensional array of tiny lenslets. Each lenslet is sufficiently small to ensure that the primary aberration it encounters is a simple wavefront tilt, and each forms a poorly resolved image of the object in its back focal plane. Because the wavefront aberration across each lenslet is simply a tilt (a different tilt for each lenslet), all of the images formed by these lenslets look the same, and an array of identical, poorly resolved images is formed. However, the location of each image depends on the degree of wavefront tilt present across the lenslet that formed it. Thus, by measuring the location of the centroid of each image relative to its unaberrated location, information about the wavefront tilt at each lenslet can be obtained.

If we represent the wavefront aberration across the nmth lenslet of the array by $W_{nm}(x,y)$, our assumption about tilt only (plus a constant phase shift) leads to the expression

$$W_{nm}(x,y) = 2\pi(\xi_{nm}x + \eta_{nm}y) + \phi_{nm} \ . \tag{5}$$

The derivatives of this function with respect to x and y, respectively, are

$$\frac{\partial W_{nm}(x,y)}{\partial x} = 2\pi\xi_{nm}$$

$$\frac{\partial W_{nm}(x,y)}{\partial y} = 2\pi\eta_{nm} \ . \tag{6}$$

Now consider Fig. 34. The quantities Δx_{nm} and Δy_{nm} represent the shift in the coordinates of the nmth image with respect to their unperturbed values. It can be shown that for small wavefront tilts, these quantities are given by

$$\Delta x_{nm} = \lambda f \xi_{nm}$$

$$\Delta y_{nm} = \lambda f \eta_{nm} \tag{7}$$

where f is the focal length of each lenslet. Thus, from Eq. (6)

$$\frac{\partial W_{nm}(x,y)}{\partial x} = \frac{2\pi\Delta x_{nm}}{\lambda f}$$

$$\frac{\partial W_{nm}(x,y)}{\partial y} = \frac{2\pi\Delta y_{nm}}{\lambda f} \tag{8}$$

and we see that the derivatives of $W_{nm}(x,y)$ are directly proportional to the shift of the image centroid. The wavefront profile along any row or column of lenslets is then found, to within a constant, by integrating the expressions of Eq. (8). These integrations are performed by digital computer, and once the profiles are found for all rows and columns, a least squares fit is performed to obtain the best estimate of the actual wavefront.

Once the wavefront is determined over the entire exit pupil, a pupil function $p(x,y)$ is defined. Then, by digital computer, the Fourier transform of the pupil function $P(\xi,\eta)$ is calculated, and the squared magnitude of this function is obtained. Finally, the estimate of the system OTF is determined from

$$\hat{H}(\xi,\eta) = K\mathcal{F}^{-1}\left[|P((x/\lambda d),(y/\lambda d))|^2\right] \tag{9}$$

where d is a constant that causes $\hat{H}(\xi,\eta)$ to have the proper scale (d is related to the lateral magnification of the system).

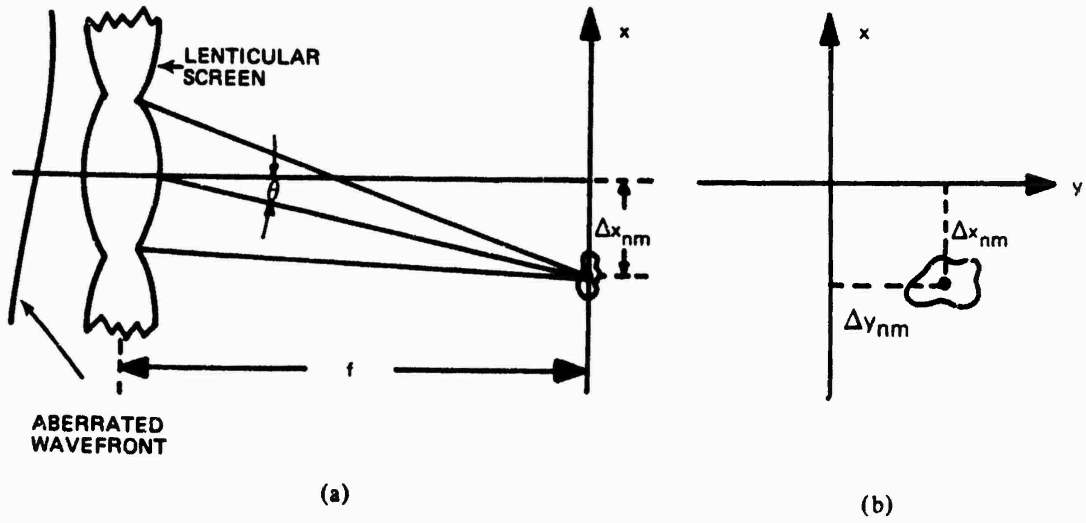

Fig. 34. Displacement of image at the *nm*th lenslet due to wavefront tilt.

D. DETERMINATION OF $\hat{i}(x,y)$

First, the degraded photographic image is scanned, corrected for photographic effects, and digitized. The resulting function is then Fourier transformed by means of a digital computer to obtain the image spectrum $I(\xi,\eta)$. Next $\hat{I}(\xi,\eta)$ is calculated from Eq. (3), but in doing so care must be taken not to divide by zero. Therefore, a threshold value is set for $\hat{H}(\xi,\eta)$ such that when $\hat{H}(\xi,\eta)$ drops below this value the numerator is left unchanged. Finally, the restored image $\hat{i}(x,y)$ is found from Eq. (4), again by digital computer. A computer printout can then be obtained for $\hat{i}(x,y)$, or its values can be used to intensity modulate a cathode ray tube (CRT) and a photograph made of the CRT display.

E. EXPERIMENTAL PROCEDURES

An optical system was designed for viewing incoherently illuminated transparencies at infinity, i.e., the object transparency was placed in the front focal plane of a lens, and the image then appeared in the back focal plane of a second lens as shown in Fig. 35. A glass plate, with sufficient thickness variations to perturb the wavefront, was placed close to the second lens, thus simulating a random, time-invariant distortion of the wavefront. A photographic image was recorded at the back focal plane of this lens, both with and without the presence of the glass plate. This was done in order to have both a blurred image and a reference with which to compare the restoration obtained.

After photographing the reference and blurred images, the objective lens was replaced with a lenticular screen composed of a rectangular array of 1-mm by 1-mm lenslets. The images formed by each lenslet were approximately 100 μm in diameter and separated by about 1 mm in both the x and y directions. The maximum displacements introduced by the wavefront distortion were on the order of 20 to 40 μm, and the images were therefore always well separated.

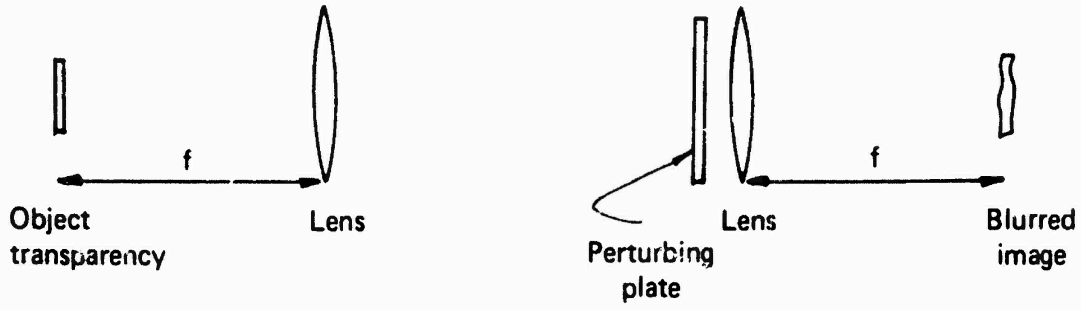

Fig. 35. Experimental setup for obtaining blurred images.

The wavefront perturbation was determined by exposing a piece of color film to two images from the lenticular screen, one with the wave aberration and one without the aberration. These two exposures were made with red and green light, respectively, so as to facilitate identification and measurement of the displaced image from the reference image for each lenslet.

An experiment was peformed in which a satellite photograph was imaged both with and without the simulated atmosphere. The rms wave aberration for this case was about 0.5λ, and this value was considered typical of the aberration for relatively poor seeing conditions with a large telescope, i.e., image resolution approximately one-tenth of the diffraction-limited value. The restoration obtained for this experiment was quite poor, as can be seen in Fig. 36c. In an attempt to determine why the restoration was unsatisfactory, an additional experiment was performed.

It was possible that the aberrated wavefront was not determined accurately enough from the Hartmann test data to calculate the correct transfer function. In order to find out how accurately the Hartmann test data must be measured in order to obtain a sufficiently good estimate of the aberrated wavefront, random perturbations in the Hartmann data were introduced artificially as explained below.

First, we assumed a perfect system, i.e., no atmospheric degradations and no telescope aberrations. Thus $H(\xi,\eta)$ was an aberration-free OTF. The array of images from which such an OTF would have been derived is a perfect array, i.e., no displacement of the centroid of any of the images ($\Delta x_{nm} = \Delta y_{nm} = 0$). Suppose, however, that in measuring the centroid locations for this perfect array, small errors $\epsilon_{x_{nm}}$ and $\epsilon_{y_{nm}}$ had been made. Thus, instead of measuring $\Delta x_{nm} = \Delta y_{nm} = 0$, $\Delta x_{nm} = \epsilon_{x_{nm}}$ and $\Delta y_{nm} = \epsilon_{y_{nm}}$ would have been obtained. The estimate $\hat{H}(\xi,\eta)$ of our OTF obtained from this erroneous data would then differ from the true $H(\xi,\eta)$ by an amount depending on the magnitudes of $\epsilon_{x_{nm}}$ and $\epsilon_{y_{nm}}$. To study the effects of such errors, the perfect centroid locations were perturbed in a random fashion, the perturbations being generated by a random number program and having a Gaussian distribution. The perturbations in x and y were chosen to be statistically independent, and the standard deviation, σ, of the x and y perturbation was taken to be the same.

The perturbed data were used to determine an associated wavefront, and the rms error of this wavefront was calculated for each value of the standard deviation σ. In addition, the estimate $\hat{H}(\xi,\eta)$ was determined, divided into the product $I(\xi,\eta)\hat{H}(\xi,\eta)$, and the spectrum $\hat{I}(\xi,\eta)$ was obtained. Finally $\hat{i}(x,y)$ was determined by Fourier transformation and compared with the original object. Table 11 lists the results of these experiments for several values of σ. For values of σ less than 4 μm, the quality of the restored images was quite good, but this image became badly degraded for values of σ between 4 and 8 μm, which corresponded to an rms wavefront error of about λ/10.

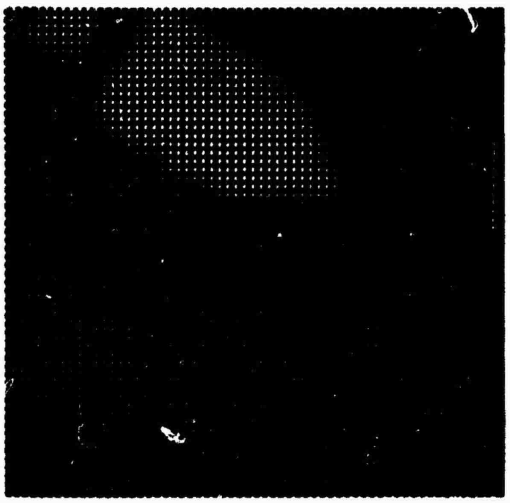

(a) Original object.

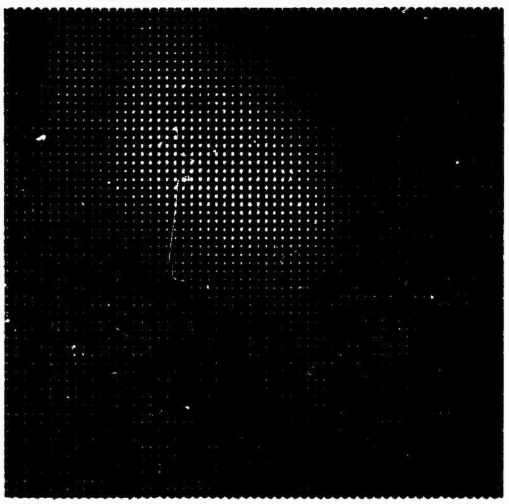

(b) Blurred image.

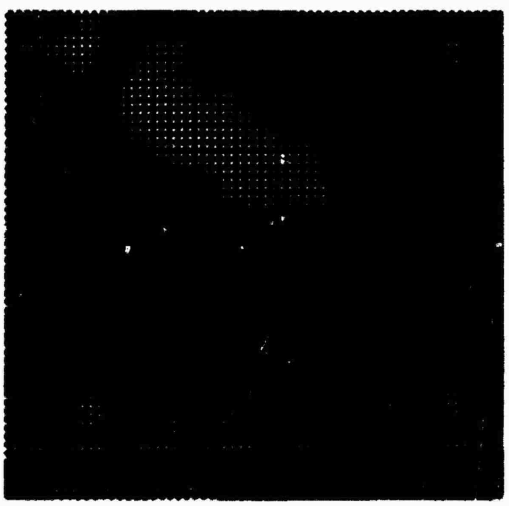

(c) Restored image.

Fig. 36. Satellite photograph imaged with and without simulated atmosphere.

Table 11. Rms Wavefront Error Introduced into Aberration-Free Wave by Perturbation of Image Centroid Data

Standard deviations of perturbations, σ (μm)	Rms wavefront error (waves)
0.001	Negligible
0.01	Negligible
0.1	Negligible
1.0	0.0181
2.0	0.0363
4.0	0.0726
8.0	0.1452
10.0	0.1815

In addition, similar perturbations were made to the data of the OTF that had already been aberrated by the atmosphere. In other words, this OTF was used to degrade the spectrum of an object, and then the data from which it had been calculated were perturbed and a new estimate was calculated. Finally, this new OTF was used to restore the degraded spectrum, and a restored image was obtained. The rms wavefront error was also calculated from the perturbed data. These results are listed in Table 12. Again the restoration began to fail for values of σ between 4 and 8 μm, or when an aberration having an rms wavefront error of about $\lambda/10$ was added to the already aberrated wave.

Table 12. Total rms Wavefront Error for Already Aberrated Wave

Standard Deviations of perturbations, σ (μm)	Rms wavefront error (waves)
0.001	0.4728
0.01	0.4728
0.1	0.4732
1.0	0.4771
2.0	0.4819
4.0	0.4936
8.0	0.5236
10.0	0.5417
100.0	1.9713

Because the measurement accuracy on the Hartmann data was better than 2 μm, it was concluded that errors in estimation of the wavefront aberration were not the reason for the inability to obtain satisfactory restorations. One other possibility for the failure of the restoration is that insufficient information was available in the blurred photograph. As mentioned previously, the presence of even a small rms error on the wavefront may cause the transfer function to have zero, or nearly zero, values in frequency bands substantially

below the cutoff frequency. In addition, the exact nature of the transfer function (shape, polarity, locations of zeros, etc.) cannot be determined simply by knowing the magnitude of the rms wavefront aberration. These features can be determined only by calculating the transfer function for each particular case. Also, the presence of zeros in the transfer function does not necessarily preclude a satisfactory restoration of a blurred image unless the original object contained important structure at the particular spatial frequencies where the transfer function is zero. Because this is not known unless the object is known, we conclude that there is no way in general to determine if the restoration will be satisfactory, even though the modified Hartmann test gives a good estimate of the perturbed wavefront.

Still another problem is caused by the addition of noise to the blurred image during the photographing and digitizing processes. All noise added after the blurring by the optical system is amplified considerably when restoration is attempted by inverse filtering. In the worst case, when the optical system transfer function is nearly zero over a range of spatial frequencies for which the object has important structure, and when the added photographic or microdensitometer noise is significant at this frequency, satisfactory restoration is prevented by insufficient signal-to-noise ratio. Because of this possibility, a third experiment was performed with a known object spectrum and reduced wave aberration.

For this experiment, the rms wave aberration was reduced to about 0.25λ, and the object was changed to an Air Force three-bar test target. Again, a satisfactory restoration could not be obtained. In this case it definitely appeared that low signal-to-noise ratio was the major problem. Even though the original object was a high-contrast bar target, the computed spectrum of the blurred image did not contain any components that were easily identified with the object.

F. CONCLUSIONS

It was concluded that, for aberrations of the magnitude used in the experiments described above, the effect of postdetection additive noise is so severe that satisfactory restoration by inverse filtering is probably not feasible. The ability to restore appears to be limited by postdetection signal-to-noise ratio, and if sufficient signal-to-noise ratio is obtained in the blurred image, restoration will probably not be necessary. In other words, restoration may be desired when the magnitude of the aberration exceeds a certain value, which may be defined as a lower bound for the aberration, but because of signal-to-noise ratio problems, it becomes unlikely when the aberration is greater than a certain upper bound. We feel that the separation of these two bounds is sufficiently small and that restoration by the methods investigated here may not be possible often enough to justify their use.

Figure 37 shows the expectation value of a statistical transfer function for random wavefront errors, as calculated by R. V. Shack. The complete transfer function for an optical system with random wavefront error may be determined by multiplying the diffraction-limited transfer function (cutoff frequency is 2 on the normalized scale shown) by the statistical transfer function shown in the figure. It is important to note that the statistical transfer function represents an ensemble average, and that a particular member of the ensemble will have fluctuations about this average. In fact, it has been shown (Diedericks, 1958) that the magnitude of transfer factor fluctuations about the average value is just

$$|\text{average value}|.$$

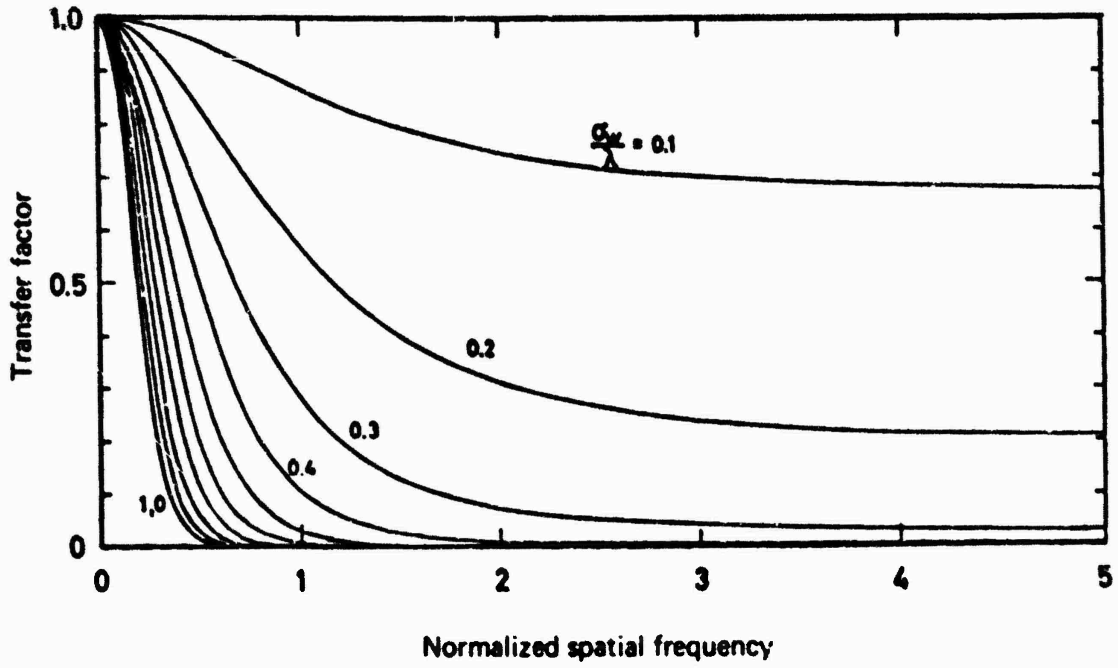

Fig. 37. Variation in equivalent transfer function with depth of wavefront disturbance. Autocorrelation function of wavefront disturbance is assumed constant.

Thus, to be reasonably certain that the wavefront distortion never causes the value of the transfer function to drop below about 10% of the diffraction-limited value, the rms wavefront aberration cannot exceed about 0.15λ. Because an aberration less than 0.1λ rms is generally considered to yield diffraction-limited performance, and an aberration greater than 0.15λ to 0.2λ rms may preclude restoration because of signal-to-noise ratio considerations, image restoration by inverse filtering appears to be worthwhile only for rms aberrations between 0.1λ and 0.15λ. As previously mentioned, typical rms wavefront aberrations for a large telescope observing through atmospheric turbulence may be greater than 0.15λ a great deal of the time, and satisfactory restorations will be possible only for very limited intervals.

Note that the wavefront aberration does not *directly* degrade the image; rather, it is the optical transfer function that may be said to cause the image blur. Therefore, if the data obtained from the modified Hartmann test were used to correct the wavefront *before* detection, an excellent image might be obtained without the need for postdetection processing. Such real-time correction of the wavefront may indeed be possible in the near future owing to the continuing advances in acoustic deflectors for electro-optic data displays. Also, nonlinear techniques in postdetection processing, nonlinear detection itself, etc., might overcome the limitations encountered in straightforward inverse filtering.

G. TELESCOPE CALIBRATION

A secondary portion of Task II was to calibrate the 122-cm primary mirror of the Cloudcroft telescope, i.e., to determine the wavefront error introduced by the primary mirror. The calibration was to have made use of the wavefront-determination-correction method of image restoration but with the modifications explained below.

The instrument designed and fabricated for this calibration contained one of the lenticular screens used for the image restoration work, and it also contained a pinhole reference source. The pinhole reference is first caused to illuminate the lenticular screen through a beamsplitter so that an array of reference images is formed and recorded. Because the light from the reference source never strikes the primary mirror, the position of the reference images is unaffected by any imperfections in the mirror. Next, with a bright star for illumination, an array of images is recorded on the same film as the reference images, but slightly offset so that none of the images fall on one another. A long exposure time is used for the second set of images so that the effects of atmospheric turbulence are averaged out.

Because the light from the star strikes the primary mirror, any imperfections in the mirror will show up as displacements of the Hartmann images over and above the original offset. These displacements are then measured, and the wavefront error introduced by the mirror is calculated in the same fashion as for the image restoration work. Our calculations indicated that in this way we could measure rms wavefront aberrations to approximately $\lambda/10$ to $\lambda/20$.

The instrument, which is shown in Fig. 38, was to have been delivered to Cloudcroft in April or May 1972, and the calibration was to have been performed at that time. However, because the telescope was inoperative or otherwise unavailable during those months, the instrument was not delivered until 10 July 1972, and bad weather prevented the calibration from being made at that time. The measurements were rescheduled for September and October, but again bad weather and telescope commitments prevented the calibration from being made.

The Cloudcroft personnel were instructed on the use of the instrument, and are qualified to make the necessary measurements if a calibration is desired in the future. The engineering drawings of this instrument have been delivered to the personnel at Cloudcroft.

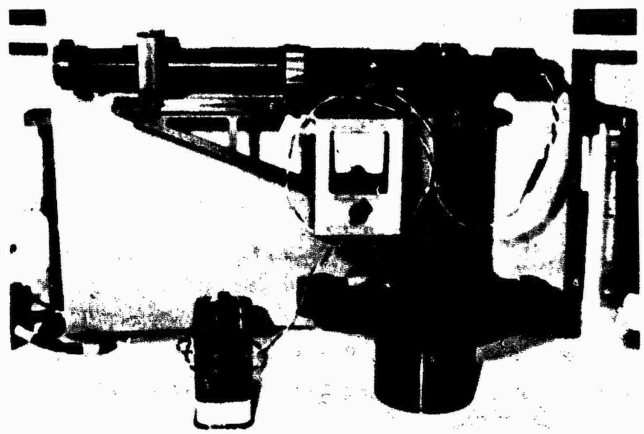

Fig. 38. Cloudcroft telescope.

TASK III. PHOTOGRAPHIC RECORDING OPTIMIZATION

The purpose of Task III was to develop a criterion for selecting a photographic film in order to optimize the information recording capability of the 122-cm (48-in.) telescope. Included in this investigation were such factors as aberrations of the telescope, exposure time, film speed and granularity, tracking error, seeing, and focal length. In the following sections, we develop a general formula for the information contained in the image based on the concept of channel capacity from information theory. The information is found to depend on the root mean square (rms) value of the image blur. The contribution to the rms blur of each of the degrading factors is determined, and an example is given demonstrating the use of the formula.

A. INFORMATION IN THE IMAGE

Throughout the development and application of this criterion, reference will be made to rms image blur of one form or another. The implication is that each of the blur mechanisms results in a two-dimensional gaussian probability density. While we realize the individual effects may not actually have rotational symmetry, ensemble averages will tend to this limit. The results we present will give a first-order guide to the importance of various factors and the extent to which they interact.

The information in the image will be calculated from a signal-to-noise ratio and will be based on the concept of channel capacity. If each spatial frequency is considered as a separate channel, an integration over all frequencies will give the total information. The channel capacity is given by

$$C = \ln(1 + (S/N)).$$

Now let us determine the appropriate values for S/N.

We assume the point spread function in the image is of gaussian form

$$p(r) = \exp(-\pi(r/\sigma)^2)$$

where r is the radial coordinate, and σ is a scaling factor.

The transfer function associated with this point spread function is also of gaussian form

$$t(\xi) = \exp(-\pi(\sigma\xi)^2)$$

in this expression, ξ is the radial spatial-frequency variable. This represents the relative signal spectral power in the image of a point object.

In order to get an idea of the noise spectral power, we will use the AIM curve. This is the aerial image modulation (as a function of spatial frequency) required to record three-bar charts, and it is a proportional measure of the noise power. The AIM curve includes processing, exposure, film transfer function granularity, and detection of image detail. While all these effects are not exactly the same for imaging three-bar targets and space objects, the AIM curve represents the capabilities of the film. The AIM curve will be represented as a gaussian of the form

$$\mathrm{AIM}(\xi) = A \exp(-\pi(r_f\xi)^2)$$

where A and r_f are parameters that characterize the film and processing conditions.

At any given spatial frequency ξ, the signal-to-noise ratio may be obtained from the appropriate ratio

$$S/N \cong \frac{\exp(-\pi(\sigma\xi)^2)}{A\exp(\pi(r_f\xi)^2)} = A^{-1}\exp[-\pi(r_f^2+\sigma^2)\xi^2].$$

Because each spatial frequency may be considered as a separate channel, the information I may be obtained by integration of the channel capacity over all spatial frequencies

$$I = \frac{2\pi}{\ln 2}\int_0^\infty \ln[1+(S(\xi)/N(\xi))]\,\xi d\xi.$$

This integral cannot be evaluated exactly, but it is approximately given by

$$I = \frac{1+(\ln A)^2}{r_f^2+\sigma^2} \quad (\text{bits/mm}^2).$$

Multiplication by the area of the image will give the total information in the image. The reciprocal of the "standard deviation" of the AIM curve r_f, is derivable from the high- and low-contrast resolution values, and σ is the rms image blur due to seeing, aberrations, tracking errors, etc.

B. ABERRATIONS

The manner in which the optical aberrations of the telescope design affect image quality will now be considered. The results are simplest for this case because the aberrations are fixed and no interactions with other system components need to be included.

The third-order aberrations are most simply expressed in terms of the effective focal length of the telescope, f the focal ratio at the image, N, the conic constant, K, the angle measured from the optical axis to the edge of the field, θ, and the axial distance from best focus, Δz. The transverse aberrations with the stop at the mirror, are as given in Table 13.

The conic constant for a parabolic mirror is equal to -1; thus, there is no spherical aberration. Because distortion is zero when the stop is in contact with the mirror, this leaves coma, astigmatism, and field curvature. Astigmatism and field curvature may be ignored if their magnitude is small in comparison to that of coma. This will be a valid condition when

$$\frac{f\theta^2}{4N} \ll \frac{f\theta}{16N^2} \quad \text{or} \quad 4N\theta \ll 1. \tag{10}$$

An $f/6.5$ mirror covering a 1-min semifield angle easily satisfies this requirement, and only coma will be considered.

The aberration in the image resulting from coma may be expressed in terms of the x and y coordinates of the ray with respect to the gaussian image position. When coma is the only aberration present, these equations are

Table 13. Transverse Aberrations for a Conic Mirror

Spherical aberration	$\frac{f(K+1)}{64N^3}$
Sagittal coma	$\frac{f\theta}{16N^2}$
Astigmatism	$\frac{f\theta^2}{4N}$
Field curvature	$-\frac{f\theta^2}{4N}$
Focus error	$-\frac{\Delta z}{2N}$

$$\Delta x = (\text{Coma})\,(\sin 2\phi)\rho^2 h \tag{11}$$

$$\Delta y = (\text{Coma})\,(2+\cos 2\phi)\rho^2 h \tag{12}$$

where h is the fractional field height, ρ is the fractional radial coordinate pupil, and ϕ is the azimuthal coordinate exit pupil.

The rms blur size due to coma, calculated from these intercept errors, is

$$r_c = \frac{f\theta}{16\sqrt{3}\,N^2} \qquad \text{(coma)} \; . \tag{13}$$

If the film is not located in the proper axial position, there is also a blur due to focus error. The radius of this geometric blur is $|\Delta z|/2N$ where Δz is the longitudinal focus error. The rms blur size due to defocus is

$$r_d = \frac{|\Delta z|}{4N} \qquad \text{(defocus)} \; . \tag{14}$$

C. TRACKING ERROR

The rms blur radius due to tracking error may be estimated from an angular error rate and the size of the resulting blur for a given exposure time. We will consider $\dot{\phi}$ to be the instantaneous error in the tracking rate (rad/sec). For an exposure time, t, this results in a linear blur of length $\dot{\phi}tf$ where f is the focal length of the telescope.

The resulting rms blur size for a uniform blur of this type is

$$r_t = \dot{\phi}tf/\sqrt{12} \qquad \text{(tracking)}. \tag{15}$$

D. SEEING

The nature of seeing is very complex and difficult to model. For our purposes, we propose a model of a heuristic nature.

We assume that there is an instantaneous best seeing, S_0, and a long time average, S_∞ which is approached exponentially as the time of observation increases (Fig. 39). Both S_0 and S_∞ are functions of the telescope aperture and atmospheric conditions.

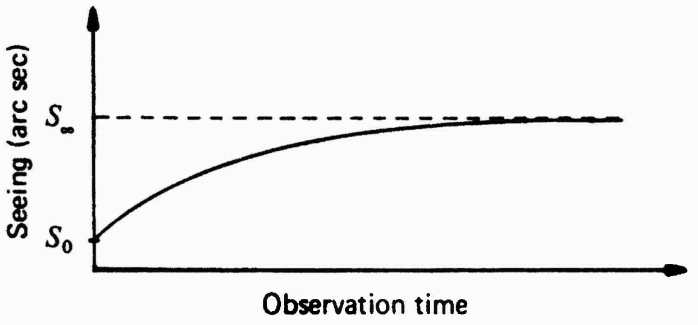

Fig. 39. Model for change of seeing with observation time.

The seeing is given by

$$S = S_\infty\left[1 - \left(\frac{S_\infty - S_0}{S_\infty}\right)\exp(-\alpha t)\right] \qquad \text{(arc sec)} \ . \tag{16}$$

In the case where S_∞ is much larger than S_0 and when we are dealing with relatively short exposure times, S^2 is accurately approximated by

$$S^2 = S_0{}^2 + 2(\alpha S_0 S_\infty)t. \tag{17}$$

The rms image blur due to seeing may be obtained from the value of seeing (in arc sec) by multiplying by 0.0384 mm. Therefore,

$$r_s = 0.0384\,(S_0{}^2 + 2(\alpha S_0 S_\infty)t)^{1/2} \qquad \text{(seeing)} \ . \tag{18}$$

E. EXPOSURE TIME

The exposure required under "daylight" conditions may be calculated from the ASA exposure index of the film used and the camera equation. The camera equation gives the exposure at the image plane as

$$E = \frac{\pi B t}{4N^2(1+m)^2} \tag{19}$$

where the ratio of the image size to object size is m (effectively zero for most telescopic uses), and B is the object brightness.

The ASA exposure index is approximately the reciprocal of the exposure (in meter-candle-seconds) required to give a density of 0.3 above base plus fog. If we employ this

criterion, the exposure is

$$E = 1/\text{ASA}. \tag{20}$$

Equating the two expressions, we find the required exposure time

$$t = \frac{4N^2}{(\text{ASA})\pi B} . \tag{21}$$

Because of the great number of variables involved, it would be very difficult to estimate B from the known parameters. We do have experimental data indicating that an exposure time of 1/125 sec is adequate for ASA 125 film at $f/16$, and substitution of these values into the equation for exposure time yields

$$B \cong 256. \tag{22}$$

This value will be used later as a typical object brightness.

F. FILM

There are many films that would be suitable for use in this application. Table 14 lists several Kodak films that are representative of the wide range of possible resolution and speed combinations.

Table 14. Parameters for Selected Kodak Films

Kodak film type	Speed		Resolving power		Granularity	Quality factor*	
	ASA	694	1000:1	1.6:1		Daylight	694.3
2479	400	6	90	32	38	1800	220
2481	80	10	80	32	38	720	250
2484	1000	X	70	--	40	2220	---
2485	8000	30	60	20	60	5360	330
2496	80	6	130	50	26	1160	320
2498	250	X	112	45	34	1780	---
LSB	125	X	125	--	--	1400	---

*The quality factor is used to estimate the relative information in the image recorded with each type of film. "X" data are not available or the spectral sensitivity is too low for use at 694 nm.

As a result of studying the modulation transfer function and granularity characteristics of these films, it has been determined that the rms blur size on the film for these films may be estimated by

$$r_f = 4/3R \tag{23}$$

where R is the measured high-contrast resolving power. Also listed in Table 14 is a quality factor. As determined below, we will find that the amount of information on the film is approximately proportional to the resolving power times the square root of the speed. This is given for both daylight and 694 nm if the data were available.

G. TOTAL MEAN-SQUARE BLUR

The total mean-square blur is obtained from the individual mean-square blur radii by assuming that they are independent random processes. This permits specifying the total as simply the sum of the squares of the rms values. Thus

$$r^2 = r_f^2 + r_s^2 + r_d^2 + r_c^2 + r_t^2 \, . \tag{24}$$

Because the telescope is often used with auxiliary relay optics, it is necessary to include this additional magnification. All the components of the total blur are affected by magnification except that component due to the film. The magnification is given by

$$M = N/6.5. \tag{25}$$

Because we are scaling the mean square radius, M^2 is used. With this factor included, the total mean square radius is

$$r^2 = r_f^2 + (N/6.5)^2(r_s^2 + r_d^2 + r_c^2 + r_t^2). \tag{26}$$

In Table 15 the formulas for the rms blur radii are summarized along with what may be considered typical values for each. The values are based on the criterion listed for a 1/125 sec exposure at $f/6.5$ focus and averaged over a total field of 2 min.

Table 15. Summary of Rms Blur Formula and Typical Values of Each

Type	Formula	Typical parameter	Blur value (μm)
Seeing	$r_s = (S_0^2 + 2\alpha S_0 S_{-1})^{1/2}$	0.5 sec	19.0
Tracking	$r_t = \phi f t/(12)^{1/2}$	10 sec/sec	3.1
Coma	$r_c = f\theta/16(3)^{1/2}N^2$	---	2.0
Focus	$r_d = \lvert\Delta z\rvert/4N$	0.1 mm	3.8
Film	$r_f = 4/3R$	LSB	10.7

H. OPTIMUM OPERATING CONDITIONS

The model that we have constructed may be used to predict optimum operating combinations of film, *f*-number, etc. based on the criterion of maximizing the information in the image. The average information is

$$I = \frac{4 \text{ bits/mm}^2}{r^2} \quad \text{(area)} \; . \tag{27}$$

The size of the image field is determined by the one minute semifield angle and the auxiliary magnification. The result is

$$\text{Area} = 17.5\,(N/6.5)^2 \text{ mm}^2 . \tag{28}$$

Therefore, the total information in the image is

$$I = \frac{70 \text{ bits}}{(6.5/N)^2 r_f^{\,2} + (r_s^{\,2} + r_d^{\,2} + r_c^{\,2} + r_t^{\,2})} \; . \tag{29}$$

Inspection of Table 15 indicates that under "typical" operating conditions, we may neglect all but r_s and r_f. This assumption will lead to useful estimates of the optimum operating conditions. In order to maximize I, we minimize the denominator (with respect to N)

$$\begin{aligned} \text{denominator} &= (6.5/N)^2 r_f^{\,2} + f^2 (S_0^{\,2} + 2\alpha S_0 S_{-} t) \\ &= (6.5)^2 r_f^{\,2} N^{-2} + f^2 S_0^{\,2} + 2 f^2 S_0 \alpha S_{-} t . \end{aligned} \tag{30}$$

The optimum value of N is

$$N^2 = (6.5/f)(r_f (\text{ASA})^{1/2})(\pi\beta/(S_0 \alpha S_{-}))^{1/2} \; . \tag{31}$$

Using this value of N we determine the required exposure time

$$t = \frac{4}{(\pi B)^{1/2}} \; \frac{6.5}{f} \; \frac{r_f}{(\text{ASA})^{1/2}} \; \frac{1}{(S_0 \alpha S_{-})^{1/2}} \; . \tag{32}$$

Substitution of these values back into the formula for the total information in the image yields

$$I = (1.5/f) \, \frac{R(\text{ASA})^{1/2} (\pi B)^{1/2}}{(S_0 \alpha S_{-})^{1/2}} \; , \tag{33}$$

where f is the prime focus focal length and the magnification is taken care of by the value of N. The factors are grouped in this formula according to their source. That is, all seeing factors combine to a single factor in the denominator, the film factors become the "quality

factor" listed in Table 14, and the prime focal length and object brightness also affect the total information.

Again, for "typical" values of object brightness and seeing, the information with LSB film is

$$I = 3 \times 10^6 \text{ bits.} \tag{34}$$

This may be increased by a factor of 3.8 by use of a better film, f-number combination. Examination of Table 14 shows how this may be accomplished.

I. FOCAL REDUCER FILTERS

Thus far we have not considered chromatic effects upon image quality because we were dealing with a mirror system that has no chromatic aberration and relay lenses for which we have no data.

The design data of the $f/3$ focal reducer are available, however, and therefore we can estimate the wavelength bands that may be used without serious loss of image quality due to a change in back focal distance. The lens was ray traced at nine separate wavelengths in the band from 500 to 900 nm, and the curve that was fit to the data is shown in Fig. 40.

The wavelength band that is permissible may be obtained by determining the range of wavelengths that results in a shift of the focal surface equal to a given tolerance. Because of the magnitude of other sources of image blur, we feel a blur tolerance of 2 μm is acceptable. This gives an allowable focal shift of ±0.024 mm (from the formula in Table 15).

If we then apply this allowable shift to the ray trace data, values for the bandwidth of the filters that can be used are obtained (see Table 16). In the vicinity of the minimum, where Wratten filters may be used, the passband is limited on the low end by the filter and on the high end by the film sensitivity.

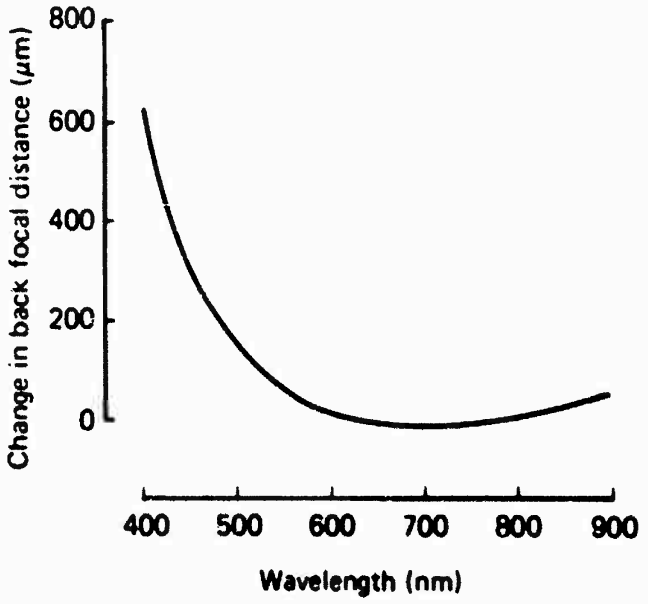

Fig. 40. Change in back focal distance with wavelength for f/3 focal reducer.

Table 16. Permissible Passband and Filters for Use with the *f*/3 Focal Reducer

Center wavelength λ (nm)	Width of passband $\Delta\lambda$ (nm)	Filter
400	9	Interference
450	16	Interference
500	28	Interference
550	51	Interference
600	103	Interference
650	205	Wratten 21* or interference
700	300	Wratten 22
750	300	Wratten 29
800	200	Wratten 89B or Wratten 70

*When this Wratten filter is used, the film should not have extended red sensitivity

TASK IV. F/3 FOCAL REDUCER

This special lens assembly was designed to be attached just inside the newtonian focus of the 122-cm *f*/6.5 parabolic mirror, where it converges the beam to a speed of *f*/3. Under perfect operating conditions, the aerial resolution over a 0.95-cm-diam flat field will be 500 lp/mm, diffraction-limited. It is restricted in resolution over larger fields owing to image curvature. It could be converted to either TV or motion picture output.

A. DESIGN

1. Technical Specifications

The lens assembly is optimized for monochromatic, pulsed-ruby laser light. It is achromatic around hydrogen-alpha red (656.3 nm), with D (589.3 nm) and A′ (768.2 nm) united in common focus. The secondary spectrum is less than one Rayleigh limit, so if the lens assembly is used with a broadband red filter, nearly diffraction-limited photographs may be taken with natural illumination. Visual focusing and testing should be performed with a red filter.

For diffraction-limited aerial resolution, the image must fall within ±0.012 mm (0.0005 in.) of the film. This corresponds to variations of the newtonian focal position of ±0.056 mm (0.002 in.).

2. Handling and Storage

The largest lenses in the focal reducer are made of flint glasses. The cells are either of brass or aluminum. Consequently, there is a considerable difference in their coefficients of expansion. All lenses are separated from their cell walls by three strips of 0.63 cm wide by 0.05 mm thick Teflon tape. Either the forward or back end of each lens seat has three strips of the same tape. At 68°F, the safely compressible total space between lens and cell wall is about 0.10 cm. Calculation shows that no significant distortion or risk of breakage will occur if the device is not exposed to temperatures below −4°F. While the lenses might survive even lower temperatures, we would feel insecure about their safety. Temperatures higher than 68°F present no breakage threat because the gap increases. We do not expect that collimation will be lost because the Teflon also expands.

CAUTION: The large lenses of the reducer are made of flint glass. This glass is notoriously sensitive to falling temperatures and to a lesser degree to rising temperatures. It would be inadvisable, for instance, to take the focal reducer from a heated room directly into the refrigerated dome. In particular, cold drafts should not be allowed to fall on a warm lens. For maximum safety, the focal reducer should be left stored in a closed box when not in use. This will protect it against rapid temperature changes.

3. Cleaning

The exposed lens surfaces should be covered with a dust-proof seal when not in use. The lenses are all hard-coated with magnesium fluoride and may be cleaned in the same manner as any other precision optical surface. (Note: The cosmetic quality of these lenses is 20-10, so particular care should be taken not to scratch them if maximum contrast is to be obtained.)

B. ASSEMBLY AND TESTING

1. Assembly

The focal reducer was assembled in our optical shop by Optician, Richard Sumner, with the assistance of Lens Designer, Richard Buchroeder, who designed the lens. Each element's ground edge was blackened to minimize scattering, each surface was washed with ethyl alcohol and wiped clean with lens tissue. While we do not have clean-room facilities, we made every effort to insure that dust was kept to a minimum. The assembled device is shown in Fig. 41.

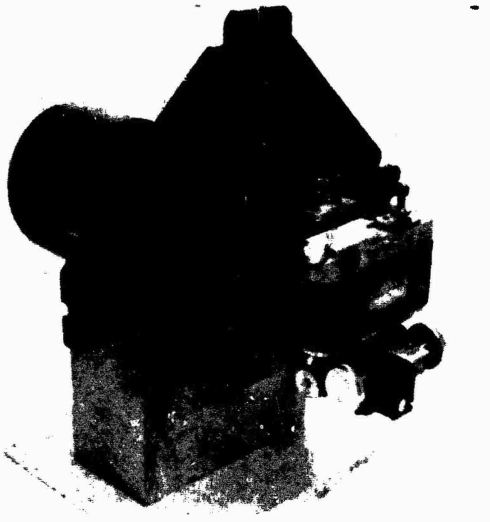

Fig. 41. Assembled focal reducer.

2. Laboratory Tests

Once assembled, the lens was tested against a precision concave spherical mirror in an autocollimation mode. The test consisted of aligning the reducer, mirror, and scatterplate interferometer to produce fringes when the correct rear conjugate was defined. The spacing of the rear element was adjusted to correct a small residual of spherical aberration. A polaroid camera with P/N film was used to photograph the fringes made with a helium-neon laser).

The tests showed that diffraction-limited performance has been achieved. The lens was found to be slightly off axis, but the wavefront was smooth and well-corrected clear to the edge.

The concentricity of the wavefront was found to be quite satisfactory.

A white-light Ronchi test (not photographed) with 100 and 200 lines/in. gratings enabled us to examine the optical correction over a wider range of wavelengths; it proved to be satisfactory. Because the lens is red-achromatized, it came as no surprise that a red filter is advisable for critical photography.

The laser was pointed down the axis of the lens and we looked for surface defects, forward and backward scattering, and reflections. There was no sign of an in-focus ghost. The cosmetic quality and antireflection coatings are excellent. Herron Optical Company should be praised for delivering lenses that actually surpass the stringent tolerances we specified. The quality is on par with that associated with precision laser optics.

3. Telescope Tests

The device was delivered to Cloudcroft on 16 February 1971, and tests were made on 30 March 1971. These tests included photography of stars and planets, as well as visual tests such as the Ronchi test. The results indicated that the focal reducer was performing as expected, and the degradations present were attributed to the atmosphere.

A second series of tests was attempted during the period 16-19 August 1971, but bad weather prevented any useful information from being obtained. Nevertheless, we conclude that when the focal reducer is properly installed and used, the resulting images will be atmospheric-turbulence limited rather than device limited.

C. OPERATION

1. Mechanical

The reducer acts as a coma-corrector for the parabolic mirror (if its coma were not corrected, it would give 21 Airy disks of tangential "parachute" glare). Consequently, centration and tilt adjustment are critical or proper quality will not be otained. For adjustment and testing, the camera should be removed and an observer should study a star image in the center of the field. The use of an ordinary eyepiece to study diffraction rings is not recommended because at $f/3$ it will introduce spherical aberration of its own. A Ronchi grating with about 100 lines/in. should be suitable, allowing both coarse and fine adjustments.

Tilts and translations are made until the axial star image is as perfect as possible. After this, stars near the edge of the field should be checked to be sure that no improper tilt compensations have been made. In principle, images over the entire field should appear equally perfect because the eye disregards the focal reducer's field curvature. Adjustment to diffraction limit will not be easy because the Airy disk has a diameter of only 0.2 arc sec. Average seeing conditions give a stellar blur of about 2.0 arc sec.

With visual testing complete, the camera can be attached. The reflex attachment is suitable for rough focusing with an eyepiece. However, if we wish to resolve diffraction-limited detail, a high-powered microscope (with a numerical aperture of 0.17; a standard numerical aperture of 0.25 is recommended) will be required. The camera will have to be "squared-on" by experiment. We regret that the number of adjustments available is less than we would like. Owing to the extremely critical range of focus, it may be necessary to adjust focus frequently, possibly between every exposure.

2. Optical

The lenses were spaced and tested prior to shipment. If the screws along the tube wall become loose, they should be retightened snugly. The set screws at either end of the tube

are used for optical adjustment. It is intended that they be locked with glyptol once performance on the telescope has been optimized. It is recommended that these screws not be adjusted except on the advice of one familiar with the nature of the optical correction. It is possible, if one is skillful, to correct minor spherical aberration of the primary mirror by alterations in the focal reducer's spacings. By the same method, the spherical aberration caused by plane-parallel filters can be compensated. In general, more harm than good will come if the lenses are indiscriminantly adjusted.

3. Filter

For daylight discrimination, a filter to isolate the ruby laser light is required. Unfortunately, the inexpensive commercial filter we purchased is unusable unless it is laid on, or very near, the film. Even then, it might cause ghost images and scattered light. For optimum performance, a new specially designed filter is needed.

In order to eliminate any optical degradation, this filter should have the form of a concentric optical window made of red filter glass (optical quality) with a multilayer intereference stack on one side, and a magnesium fluoride antireflection coating on the other. It can be attached with a close-fitting slip-on cell to the front of the focal reducer. The making of such a filter is a major task. Unfortunately one cannot be purchased because it is of a specialized nature.

D. CONCLUDING REMARKS

The ordinary *f*/2, *f*/2.8, or *f*/4 photographic lens gives a resolution that is rarely better than 100 lines/mm, and then it is usually accompanied with considerable flare. We have built a lens that will resolve to 500 lines/mm with no geometrical flare. Our lens is diffraction limited in almost the purest sense.

While it is not uncommon to achieve diffraction performance in an *f*/3 (numerical aperture = 0.1667) microscope objective, it is a formidable challenge to do so in such a large assembly as the focal reducer. Each lens surface was polished to a surface accuracy of better than five millionth's of an inch; the glass is of such high quality that not the slightest strain or striae can be seen between crossed polaroids. Each lens is centered to a fraction of 1 arc min.

The degree of precision that we have achieved is appreciated when one considers that the first lens accepts a light bundle 7.62 cm in diameter; the assembly then compresses this to a spot only 3.81 μm in diameter. Not only is this accomplished on axis, but it corrects defects of a parabolic mirror that are 20 times too severe so that a moderate flat field of view with diffraction-limited resolution is obtained.

ACKNOWLEDGMENTS

The authors gratefully thank R. A. Buchroeder, P. B. Keenan, J. D. Nichols, B. C. Platt, J. D. Rancourt, R. V. Shack, and F. R. Whitehead for the work they performed under this contract.

REFERENCES

Campana, S. B., 1971, "Bright lights and L^3 TV–A poor mix," pp. 22-27 in *Electro-Optical Systems Design,* Naval Air Development Center, Warminster, Pennsylvania.

Coltman, J. W. and A. E. Anderson, 1959, "Noise limitations to resolving power in electronic imaging," Westinghouse Scientific paper 6-41000-0-P2; also Proc. IRE 48:858-865, 1960.

Diedericks, E., 1958-1959, "Statistische Oberflaechenfehler, Einfluss auf den Uebertragungsfaktor und Toleranyen," Schneider and Company, Hausmitteilunger 11(3/4).

Electronic Industries Association, 1964, "Relative spectral response data for photosensitive devices, S-curves," Publication No. 50.

Jones, R. C., 1958, "On the quantum efficiency of photographic negatives," Phot. Sci. Eng. 2(2):57-65.

Jones, R. C., 1959, "Quantum efficiency of detectors for visible and infrared radiation," pp. 87-183 in *Advances in Electronics and Electron Physics,* Vol. 11, L. Marton, Ed., New York, Academic Press.

Marchant, J. C., and A. G. Millikan, 1965, "Photographic detection of faint stellar objects," J. Opt. Soc. Am. 55(8):907-911.

Rosell, R. A., et al., 1968, "Noise limitations to the detection of isolated square images on a TV monitor," preliminary report, Westinghouse Aerospace Division, Baltimore, Maryland.

Smith, G. H., 1972, "Evaluation of image intensifier tubes using detective quantum efficiency," Optical Sciences Center Tech. Rept. 76, 46 pp.

Varo, Inc., 1972, "Image-intensifier and image-converter tubes," Electron Devices Division, Garland, Texas, 16 pp.

Zweig, H. J., G. C. Higgins, and D. L. MacAdam, 1958, "On the information-detecting capacity of photographic emulsions," J. Opt. Soc. Am. 48(12):926-933.

UNCLASSIFIED
Security Classification

DOCUMENT CONTROL DATA - R & D

(Security classification of title, body of abstract and indexing annotation must be entered when the overall report is classified)

1. ORIGINATING ACTIVITY *(Corporate author)*
Optical Sciences Center
University of Arizona
Tucson, Arizona 85721

2a. REPORT SECURITY CLASSIFICATION
UNCLASSIFIED

2b. GROUP

3. REPORT TITLE
Electro-Optical Aerospace Surveillance Studies

4. DESCRIPTIVE NOTES *(Type of report and inclusive dates)*
Final report, December 1969 through December 1972

5. AUTHOR(S) *(First name, middle initial, last name)*
L. Ralph Baker
Richard H. Cromwell
Jack D. Gaskill

6. REPORT DATE	7a. TOTAL NO. OF PAGES	7b. NO. OF REFS
September 1973	75	11

8a. CONTRACT OR GRANT NO.	9a. ORIGINATOR'S REPORT NUMBER(S)
F33615-70-C-1203	
b. PROJECT NO.	
c.	9b. OTHER REPORT NO(S) *(Any other numbers that may be assigned this report)*
d.	AFAL-TR-73-188

10. DISTRIBUTION STATEMENT
Distribution limited to U.S. Government agencies only; test and evaluation, 21 June 1973. Other requests for this document must be referred to AFAL (RSO-4) W-PAFB, OH 45433.

11. SUPPLEMENTARY NOTES	12. SPONSORING MILITARY ACTIVITY
	Air Force Avionics Laboratory Air Force Systems Command Wright-Patterson Air Force Base, Ohio

13. ABSTRACT

The purpose of this contract was to study methods for improving images of space objects obtained with earth-based telescopes. The results of the four contractual tasks are presented. With regard to Task I, recommendations are given for the best intensifier/SIT combinations and relay optics for the Cloudcroft satellite imaging program. As discussed in the section on Task II, it has been concluded that the wavefront-determination-correction method of image restoration is probably not feasible if only linear, postdetection inverse-filtering techniques are used. A discussion of the telescope calibration instrumentation is also included. With regard to Task III, information is listed that allows the optimum film/*f*-number combination to be determined for use with the *f*/3 focal reducer. The design and operation of the *f*/3 focal reducer are discussed in the section on Task IV.

DD FORM 1 NOV 68 1473

UNCLASSIFIED
Security Classification

14. KEY WORDS	LINK A		LINK B		LINK C	
	ROLE	WT	ROLE	WT	ROLE	WT
Electro-optical imaging devices						
SIT camera tube						
Charge-coupled devices						
Image intensifiers						
Image restoration						
Telescope calibration						
Photographic recording optimization						
Focal reducer						